Title
Corrosion Issues in the Disposal of High Level Nuclear Waste

Author
Lu, Pin

Publication Date
2016

Peer reviewed|Thesis/dissertation

Corrosion Issues in the Disposal of High Level Nuclear Waste

By

Pin Lu

A dissertation submitted in partial satisfaction of the
requirements for the degree of
Doctor of Philosophy
in
Engineering — Materials Science and Engineering
in the
Graduate Division
of the
University of California, Berkeley

Committee in charge:

Professor Digby D. Macdonald
Professor Thomas M. Devine
Professor Paulo J. M. Monteiro

Summer, 2016

Abstract

Corrosion Issues in the Disposal of High Level Nuclear Waste

by

Pin Lu

Doctor of Philosophy in Engineering — Materials Science and Engineering

University of California, Berkeley

Professor Digby D. Macdonald, Chair

Corrosion in geological disposal facilities of high level nuclear waste is of great importance to maintain the integrity of the waste container and thus ensure the public safety. Specifically, a nuclear waste "Supercontainer" has been designed by Belgium with carbon steel as being the main metallic barrier material. The corrosion environment in the Supercontainer has been determined to be anoxic for the vast majority of the service period, and the forms of corrosion are expected to be mainly general passive corrosion and pitting corrosion due to passivity breakdown. In order to realize the prediction of accumulated corrosion damage over the exceedingly long service horizon of the Supercontainer (>100,000 years), employment of mechanistically based or analytic models are necessary. Accordingly, the passivity and passivity breakdown of carbon steel were investigated in this dissertation work experimentally using electrochemical techniques and analyzed within the framework of the Point Defect Model (PDM), an analytical model describing the mechanism of passivity.

A mixed potential model has been developed to deconvolve the negative total current density that is observed at potentials more negative than the open circuit potential, E_{corr}, under anoxic conditions into its partial anodic and cathodic components as a function of potential across the passive range. Deconvolution was successfully achieved by optimizing a Mixed Potential Model (MPM) comprising the PDM to describe the partial anodic process and the Butler-Volmer equation to describe the partial cathodic process of hydrogen evolution. In this manner, the corrosion rate can be determined across the entire passive range, including the range of potential ($E < E_{corr}$) within which the net observed current density is negative.

The commonly observed irreversibility of the passive state on carbon steel in alkaline solutions was examined in simulated concrete pore solution under anoxic conditions replicated by applying relatively negative film formation potentials, at which the cathodic process dominates the passive system. The fundamental source of this irreversibility was investigated by describing the kinetics of the passive system by the MPM. Electrochemical impedance spectroscopy, Mott-Schottky analysis and model optimization were performed at each potential when the potential was first stepped in the anodic direction and then in the cathodic direction. The experiment and optimization results demonstrate that the irreversibility of the passive state is closely associated with the discrepancy in the defect structure of the passive film upon opposite stepping directions of the film formation potential, and is essentially caused by the slower film formation and slower film dissolution during the cathodic potential stepping than those during the anodic potential stepping.

The theory of the kinetics of nucleation of metastable pits in terms of the PDM has been applied the first time to describing the evolution of the nucleation rate of metastable pits on a variety of metallic substrates. The PDM successfully accounts for the experimental data that have been reported in the literature on stainless steel, carbon steel, iron, aluminum, and Alloy-22, and which are judged to be reliable and reproducible. Important fundamental parameters related to metastable pitting such as total number density of pitting nucleation sites, dissolution time of the cap over the pit, energy related to absorption of the aggressive ions into oxygen vacancies in the surface of the barrier layer, vacancy condensation rate, and the time at which the nucleation rate of metastable pits is maximum were obtained from the optimization of the PDM on the experimental data, as reported in the present paper. The values obtained for those parameters are in good agreement with values and observations reported elsewhere.

Finally, passivity breakdown on carbon steel was studied in various solutions with different pH values, chloride concentrations, and temperatures. The data are interpreted in terms of the PDM, too. An increase in temperature from 25 °C to 85 °C results in a decrease in localized corrosion resistance according to a linear relationship between the critical pitting potential and log (chloride activity) for all chloride concentrations. The linear dependence of the critical pitting potential on the square root of potential scan rate, as predicted by the PDM, yields an estimate of the critical areal concentration of condensed cation vacancies at the metal/film interface that leads to the passivity breakdown.

Table of Contents

List of Figures

List of Tables

List of Symbols

Roman Symbols

a	constant defined in Eq. (7-12)	s
a_i	constant for *i*th point defect reaction defined in Table 2-3	V^{-1}
a_{X^-}	activity of aggressive anion X^-	mol L^{-1}
A	parameter defined in Eq. (7-14)	cm^{-2}
b	constant defined in Eq. (7-13)	-
b_{anod}	Tafel slope of cathodic reaction upon the anodic potential stepping	V dec^{-1}
b_{cath}	Tafel slope of cathodic reaction upon the cathodic potential stepping	V dec^{-1}
b_c	Tafel slope of cathodic reaction	V dec^{-1}
$\widehat{b_c}$	Tafel slope of cathodic reaction on completely film-free surface	V dec^{-1}
b_i	constant for *i*th point defect reaction defined in Table 2-3	cm^{-1}
B	function defined in Eq. (7-9)	cm^{-4}
c_i	constant for *i*th point defect reaction defined in Table 2-3	-
C_H	concentration of hydrogen ions at the bl/s interface	mol L^{-1}
C_H^0	standard state concentration of hydrogen ions at the bl/s interface	mol L^{-1}
C_{dl}	capacitance of the double layer	F cm^{-2}
C_g	geometric capacitance of the barrier layer of the passive film	F cm^{-2}
C_{ol}	capacitance of the outer-layer of the passive film	F cm^{-2}
C_{sc}	space charge capacitance	F cm^{-2}
D	diffusivity of cation vacancies	cm^2 s^{-1}
$\overline{D}$	mean diffusivity of cation vacancies	cm^2 s^{-1}
D_i	diffusivity of metal interstitials	cm^2 s^{-1}
ΔG_A^0	standard Gibbs energy change for the chloride/oxygen vacancy absorption reaction	J mol^{-1}
ΔG_S^0	standard Gibbs energy change for the Schottky pair reaction	J mol^{-1}
e	electronic charge	C
F	Faraday's constant	C mol^{-1}
i_0	exchange current density	A cm^{-2}
$\widehat{i_o}$	current density of a "film-free" redox reaction	A cm^{-2}

i_{anod}	anodic partial current density in the steady state	A cm^{-2}
i_{cath}	cathodic partial current density in the steady state	A cm^{-2}
i_{ss}	passive current density in the steady state	A cm^{-2}
i_{totoal}	total current density of the system in the steady state	A cm^{-2}
I_{ss}	passive current in the steady state	A
J_{ca}	flux of cation vacancies across the barrier layer at the breakdown site	cm^{-2} s^{-1}
J_m	the annihilation flux of the cation vacancies at the breakdown site	cm^{-2} s^{-1}
k	Boltzmann's constant	J K^{-1}
k_c	rate constant for cathodic reaction	mol cm^{-2} s^{-1}
k_i	rate constant of ith point defect reaction, $k_i = k_i^0 \mathrm{e}^{a_i V} \mathrm{e}^{b_i L} \mathrm{e}^{c_i \mathrm{pH}}$	Table 2-3
k_i^0	standard rate constant of ith point defect reaction	Table 2-3
K	$K = \gamma\varepsilon$	cm^{-1}
L	thickness of the barrier layer	cm
L_{ss}	steady-state thickness of the barrier layer	cm
n	reaction order of the dissolution of the barrier layer	-
N_0	total number of available breakdown site	cm^{-2}
N_A	Avogadro's number	-
N_d	donor density	cm^{-3}
$N(t)$	integral number of metastable pits as a function of observation time, Eq. (7-11)	cm^{-2}
$N(D)$	number of breakdown sites that have diffusivities larger than D	cm^{-2}
$n(t)$	nucleation rate of metastable pits as a function of observation time, Eq. (7-15)	cm^{-2} t^{-1}
R	ideal gas constant	J mol^{-1} K^{-1}
R_c	resistance associated with the cathodic reaction	Ω cm^2
R_{ol}	resistance of the outer-layer of the passive film	Ω cm^2
R_s	resistance of the solution	Ω cm^2
t_{max}	time at which the nucleation rate maximizes	s
t_{ind}	induction time of metastable pitting	s
T	temperature	K or °C
v	potential sweep rate of potentiodynamic scan in determining V_b	V/s

V_{app}	applied potential	V
V_b	passivity breakdown potential	V
V_{fb}	flat-band potential	V
$V_M^{\chi'}$	cation vacancy	-
$V_O^{\cdot\cdot}$	oxygen vacancy	-
w	energy term defined in Eq. (7-4)	J mol^{-1}
W	Warburg impedance element	-
Y_{cath}	conductance of the cathodic reaction	S
Z'	real part of impedance	Ω cm^2
Z''	imaginary part of impedance	Ω cm^2
Z_{cath}	impedance of the cathodic reaction	Ω cm^2
$Z_{e,h}$	diffusional impedance of electrons and/or electronic holes through barrier layer	Ω cm^2
Z_F	faradaic impedance within the barrier layer	Ω cm^2
Z_{ol}	impedance of the outer-layer	Ω cm^2
Z_{total}	total impedance of an interfacial system	Ω cm^2
Z_W	Warburg impedance	Ω cm^2

Greek Symbols

α	polarizability of the barrier layer/solution interface	-
α_c	transfer coefficient for cathodic reaction	-
α_i	transfer coefficient for *i*th point defect reaction	-
β	dependence of the potential drop across barrier layer/solution interface on pH	V
$\hat{\beta}$	tunneling constant of a passive film	cm^{-1}
γ	$\gamma = F/RT$	V^{-1}
ε	electric field strength within the barrier layer	V cm^{-1}
ε_0	vacuum permittivity	F cm^{-1}
$\boldsymbol{\eta}$	cathodic overpotential	V
λ	parameter defined in Eq. (7-3)	cm^2 s^{-1}

ξ	critical concentration of vacancies	cm^{-2}
σ	Warburg coefficient	$\Omega\ s^{-1/2}$
σ_D	standard deviation for cation vacancy diffusivity	$cm^2\ s^{-1}$
τ	the dissolution time of the cap over the vacancy condensate	s
$\phi^0_{f/s}$	potential drop at the film/solution interface for V_{app} = 0 and pH = 0	V
χ	oxidation state of host cation within the barrier layer	-
Ω	molar volume of oxide per cation in the barrier layer	$cm^3\ mol^{-1}$

Abbreviations

bl/ol	barrier layer/outer-layer interface
bl/s	barrier layer/solution interface
CS	Carbon Steel
EIS	Electrochemical Impedance Spectroscopy
HER	Hydrogen Evolution Reaction
HFM	High Field Model
HLNW	High Level Nuclear Waste
IAEA	International Atomic Energy Agency
K-K	Kramer-Kronig
MPM	Mixed Potential Model
M-S	Mott-Schottky
m/bl	metal/barrier layer interface
ONDRAF/NIRAS	Belgian Agency for Radioactive Waste and Enriched Fissile Materials
PDM	Point Defect Model
PEM	Place Exchange Model
SCE	Saturated Calomel Electrode
SCPS	Simulated Concrete Pore Solution
SHE	Standard Hydrogen Electrode
SS	Stainless Steel
VHLW	Vitrified High-Level Waste
XPS	X-ray Photoelectron Spectroscopy

Acknowledgements

First and foremost, enormous gratitude is due to Professor Digby D. Macdonald who has been my advisor for five years and has provided me relentless support and encouragement, in both academic research and life.

I would like to extend my thanks to my dissertation committee members who offered me invaluable guidance and advice in completing this work: Professor Thomas M. Devine and Professor Paulo J. M. Monteiro.

I would also like to thank Dr. Samin Sharifi-Asl, Dr. Feixiong Mao, Dr. Yifan Jiang, and all other colleagues of mine, past and present, for their collaboration and useful discussions.

Finally, special thanks to my parents for their constant support over all these years; to my daughter, Irene, for brightening each day of my life with your smile and laughter; and to my wife, Yingjie — my eternal gratitude for your unwavering love and patience.

Chapter 1 Overview

Worldwide, industrial development and economic growth requires the ever-increasing production of energy. Nuclear energy has been recognized as a continuous, affordable, reliable base-load power, without carbon dioxide emissions. Currently (as of June 2016), there are about 440 commercial nuclear power reactors operable in 31 countries, with over 380,000 MW of total capacity, which provide over 11% of the world's electricity [1]. In 2015, 13 countries relied on nuclear energy to supply at least one-quarter of their total electricity. However, besides producing electricity for the benefit of society, nuclear power leaves dangerous radioactive residues for which a safe, long-term solution has to be found to protect the many generations to come.

The generally accepted strategy for dealing with long-lived High Level Nuclear Waste (HLNW) is deep underground burial in stable geological formations, after a period of interim storage to allow for the decay of both the temperature and the most active, short-lived isotopes (transmutation of long term radioactive elements is the other main approach). In geological disposal, or in long term interim storage, isolation of the waste is achieved by applying the multi-barrier concept, which involves the use of several natural and/or engineered barriers to retard and/or to prevent the transport of radio-nuclides into the biosphere. The metallic container constitutes one of the most important engineered barriers, with the main threat to metal or alloy integrity being corrosion. Clearly, the reliability and the viability of integrity predictions are of paramount importance in assuring the public that safe storage and disposal can be achieved. The prediction of accumulated corrosion damage with regard to engineered barrier integrity must be discussed, compared, and explored within the corrosion community, which has the responsibility of meeting the challenge of predicting corrosion damage over millennia or hundreds of millennia on a sound scientific and technical basis.

It has become evident that purely empirical methods cannot meet the challenge of assuring the public of the safe disposal of HLNW within the engineered barrier concept, due to the rapid-growing uncertainty over extended extrapolation in empirical protocols [2]. Deterministic modeling, which posits that the future may be predicted from the past upon the basis of the natural laws, has to be incorporated complementarily with empiricism for effective prediction. The development of mechanistically based models to account for the corrosion process becomes an absolute necessity in deterministic modeling. Several challenges stand out to devise a valid deterministic model: decide what variables to be included in the model in order to accurately and completely represent the corrosion system; establish the corrosion evolution path (i.e., what path the system will follow to proceed from the current status to the further status); and specify the kinetic parameters of the corroding system (i.e., how fast the system will proceed along the evolution path). Specifying the corrosion evolution path hundreds of thousands of years into the future is often the greatest challenge and it is under intensive study in the community of nuclear and corrosion scientists.

Specifically, in Belgium, a design of Supercontainer has been proposed for the geological disposal of HLNW, in which carbon steel is the material for the main metallic barrier (“overpack”). The possible forms of corrosion damage incurred to carbon steel has been decided to be slow general corrosion due to passive state and/or pitting corrosion due to passivity breakdown that is expected to occur if Supercontainer is breached for some reason and aggressive substance invades the carbon steel barrier. Therefore, it is of critical importance to investigate and understand the

passivity and passivity breakdown of carbon steel inside the Supercontainer environment, which has been focused in this work. The present thesis work also aims to contribute to the deterministic modeling of the corrosion of the overpack by obtaining the kinetic parameters of the passive corrosion of carbon steel inside the Supercontainer. This was done by employing an analytical (mechanistically based) model, namely the Point Defect Model, to account for the passivity of carbon steel, as expanded in the later chapters.

Some specific efforts in this dissertation are that we:

1. Conducted a series of comprehensive electrochemical analysis on carbon steel in the simulated concrete pore solution, including electrochemical impedance spectroscopy, potentiodynamic polarization, and Mott-Schottky analysis, etc., to investigate the passive state of carbon steel.
2. Studied the kinetics of the passivity on carbon steel under potentiostatic anoxic conditions and extracted kinetic parameter values by optimizing the Point Defect Model (PDM) on experimental impedance data; a mixed potential model was developed to account for the very cathodic anoxic condition in the Supercontainer and the corrosion rate of carbon steel was calculated.
3. Developed and tested the theory of the kinetics of metastable pit nucleation in terms of the PDM to gain deeper understanding of metastable pitting on metal surfaces. Via optimization of the PDM on experimental metastable pit nucleation rate data, important fundamental parameters governing the kinetics of nucleation were extracted successfully. Moreover, these parameters were able to yield an accurate prediction of the critical pitting potential of various metals and alloys.
4. Performed an intensive experimental investigation into the passivity breakdown of carbon steel in various solutions with different pH values, chloride concentrations, and temperatures, which generates a comprehensive data base of critical pitting potential of carbon steel. Numerical analysis of the pitting potential data within the framework of the PDM produced values of fundamental parameters that contribute to elucidating the passivity breakdown of carbon steel.

The materials in this dissertation are divided into 9 chapters. Chapter 1 (this chapter) describes the current nuclear power status, points out the corrosion problems in the geological nuclear waste repository, and introduces the thesis work and organization of this dissertation. Chapter 2 is intended to provide some pertinent background information on the HLNW Supercontainer and corrosion of the carbon steel overpack. Theories of the PDM for film growth and dissolution under steady state, as well as a review of metastable pit nucleation, are also introduced in Chapter 2. Chapter 3 describes the experimental details of this thesis work, including materials, apparatus setup, and experiment procedures. The experimental results related to passivity of carbon steel are then presented and discussed in depth in Chapter 4. Chapter 5 details the development of the mixed potential model that combines the PDM and the Butler-Volmer equation to account for the kinetics of passivity on carbon steel, and Chapter 6 reports the results of the optimization of the mixed potential model on experimental impedance data. The analysis on optimization results is also included in Chapter 6. Chapter 7 focuses on testing the theory of

the kinetics of metastable pit nucleation and Chapter 8 explores the pitting corrosion of carbon steel in alkaline chloride-containing environment under various conditions. Chapter 9 summarizes this dissertation, and discusses some possible future work.

References

[1] Nuclear Power in the World Today, in.
[2] D. Féron, D.D. Macdonald, Proc. MRS Proceedings, 2006.

Chapter 2 Background

2.1 The High Level Nuclear Waste Supercontainer

HLNW are the highly radioactive materials produced as a byproduct of the reactions that occur inside nuclear reactors. HLNW contain highly radioactive fission products and thus they must be handled and stored with care. Since the only way radioactive waste finally becomes harmless is through decay, which for HLNW can take hundreds of thousands of years, the wastes must be stored and finally disposed of in a way that provides adequate protection of the public for a very long time. Indeed, according to International Atomic Energy Agency (IAEA), the fundamental safety objective of all radioactive waste management activities is "to protect people and the environment from harmful effects of ionizing radiation" [1].

Among many proposed resolutions to meet the objective defined by IAEA, geological disposal, that is, disposal in a repository constructed in a stable geological formation, is the solution currently recommended at the international level to protect human and the environment from the risks associated with high-level radioactive waste. This solution is based on a strategy of concentration and confinement of the radionuclides and other contaminants present in the wastes and their packaging, instead of a strategy of dilution and dispersion. It employs a system of engineered and natural barriers between the wastes and the surface environment in order to prevent these radionuclides and the other contaminants ever reaching it in such concentrations that they could present an unacceptable risk, for man and the environment.

The Belgian radioactive waste management organization (ONDRAF/NIRAS) is committed to developing a concept and design of a geological disposal facility, and to developing the evidence and arguments required to prove that such a facility can be constructed in a safe, technically feasible and economically achievable manner, without neglecting the societal aspects. The current plans of ONDRAF/NIRAS for the disposal of HLNW, mainly including vitrified high-level waste (VHLW) and spent fuel, in Belgium calls for encapsulating the processed or un-reprocessed waste in Supercontainers permanently (for 100,000 to 1,000,000 years), which is currently being studied as the reference design for the packaging of HLNW [2-7].

The Supercontainer is essentially a multi-barrier system that includes a prefabricated, massive cylindrical concrete block made of ordinary Portland cement, named the "buffer", into which a watertight cylindrical carbon steel container, the so-called "overpack", holding HLNW canisters, are inserted. After the insertion, the cavity between the carbon steel overpack and the concrete buffer is filled with a cementitious material, the "filler". The entire concrete block will then be fitted into an outer, cylindrical stainless steel container, termed the "envelope". The general conceptual design of the Supercontainer for VHLW is presented in Figure 2-1 and the dimensions are shown in Table 2-1 [8].

The Supercontainer design was developed based on the contained environment concept, the basic idea of which is to encapsulate the overpack in a tailor-made buffer that isolates the immediate overpack environment from the clay repository. This design would establish and maintain a chemically benign environment around the overpack, with respect to corrosion, that is favorable in maintaining the overpack's integrity at least during the thermal phase. The thermal

phase is assumed to last for at least hundreds of years for vitrified HLNW after emplacement of the wastes in the underground repository.

After construction of the Supercontainer, it will be transported into pre-built underground galleries and disposed in a deep clay layer (i.e. the host rock formation). All the remaining voids in the disposal gallery (e.g. voids between the Supercontainer and the gallery) will be backfilled with a cement-based material.

2.1.1 Carbon Steel Overpack

The overpack will surround the VHLW canisters or spent fuel assemblies and provide the main barrier to radionuclide release during the thermal phase. Based on recommendations of the ONDRAF/NIRAS corrosion panel, the overpack will be manufactured from carbon steel. A low-alloy steel (Cr-Mo-type) was originally recommended for the overpack by the Belgian expert review panel. However, low-alloy steels are not necessarily adequately resistant to sulphide attack and are more difficult to weld, and carbon steel is now preferred on the basis of its more predictable behavior. The choice of carbon steel as an overpack material for VHLW and spent fuel is consistent with the preference in the strategic choices of ONDRAF/NIRAS for using materials for which broad experience and knowledge already exists, i.e. it being widely used in many engineering applications. The behavior of carbon steel in a concrete environment, in particular, is well understood and favorable to meeting the requirement for overpack longevity.

2.1.2 Concrete Buffer

The Portland cement has been chosen primarily based on the strategic preferences made by ONDRAF/NIRAS for using well-understood materials. Concrete is indeed widely used to stabilize various types of underground excavations in many countries, and as a material for shielding of ionizing radiation sources. Its mechanical and shielding properties are thus well characterized. The concrete buffer functions as a radiological shield so that dose rates at the outer surface of the Supercontainer are low (maximum dose of 25 μSv per hour at a distance of 1 meter from the surface) [5] and the containers can thus be handled by the workforce without using additional shielding, which will be a significant benefit during the operational phase when transportation and underground installation of the Supercontainer take place. Furthermore, it will also provide a highly-alkaline environment, in which the external surface of the overpack will be passivated and is expected only to be prone to slow uniform corrosion, provided that the outer envelope remains intact.

Concrete buffer will be pre-cast and allowed to cure so that moisture is prevented from evaporating from it. Therefore, the buffer will have a significant pore water content when the supercontainer is initially assembled. After overpack insertion, an annular gap will remain between buffer and overpack; the filler will be used to fill this gap. The principal functions of the filler are to fill the void space at the overpack surface, thereby ensuring a “good” contact between the overpack, filler and buffer to contribute to minimizing overpack corrosion and allowing heat transfer from the overpack.

2.1.3 Stainless Steel Envelope

The incorporation of the stainless steel envelope into the Supercontainer has been just confirmed not long before. The envelope will probably be made from 6 mm-thick low carbon stainless steel sheeting with a welded bottom and lid [5]. The method of attaching the lid has not been finalized. The primary function of the envelope is to provide mechanical strength and thereby facilitate fabrication of the buffer and handling of the Supercontainer. The envelope may, if sealed, also prevent water ingress from the clay environment for a time, and may facilitate monitoring during the operational period by allowing instrumentation to be attached to the external surface of the Supercontainer. However, no reliance is placed on the envelope for ensuring long-term radiological safety. An important design issue concerns whether the envelope should be sealed or will be constructed with openings such as vents, which is still under investigation.

Table 2-1: Dimensions of the Supercontainer and disposal gallery for vitrified HLNW and its various components [8].

Components	Dimension (m)
Canister	
canister length without lid	1.335
canister length with lid	1.338
nominal height of glass inside canister	1.100
canister outer diameter	0.430
thickness of canister wall	0.005
Overpack	
overpack length	2.725
overpack thickness	0.030
overpack outer diameter	0.520
Cementitious filler	
thickness 2nd phase portlandite filler	0.050
Buffer	
buffer length	4.070
buffer inner diameter	0.620
buffer outer diameter	2.020
Supercontainer	
length supercontainer	4.082
Supercontainer outer diameter	2.032
stainless steel outer envelope thickness	0.006
Disposal gallery	
gallery length	1000
spacing between 2 disposal galleries	50
gallery inner diameter	3.000
gallery outer diameter	3.600

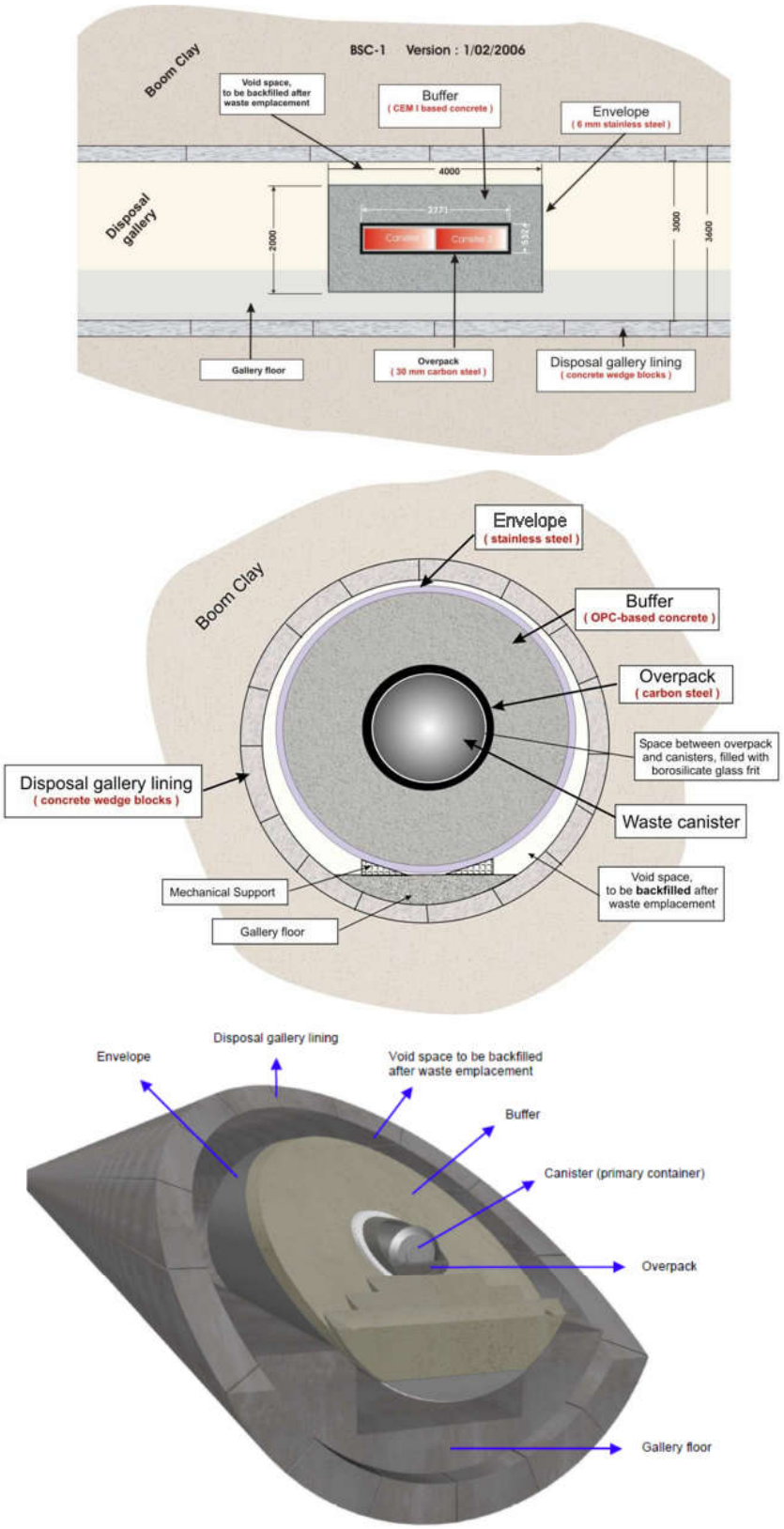

Figure 2-1: Illustration of the cross-section (top) and longitudinal-section (middle) of the high level nuclear waste Supercontainer and 3D representation of a Supercontainer emplaced in a disposal gallery (bottom) [from ONDRAF].

2.2 Corrosion of Carbon Steel in the HLNW Supercontainer

As described above, Supercontainers are essentially the unit formed by the cylinder carbon steel overpack and a massive concrete block ("buffer"). The overpack is regarded as the primary protective layer of the multi-barrier Supercontainer. Since the annular space between the overpack and the stainless steel envelope is envisioned to be filled with a cementitious buffer having a composition similar to that of Portland cement, it has been assumed that the principal threat to container integrity is corrosion of the carbon steel overpack in contact with Portland cement concrete. Due to water in the concrete, the corrosion medium of the overpack is thus concrete pore solution, which is defined as being equivalent to saturated $Ca(OH)_2$ with its pH being adjusted to 13.5 at 25°C by the addition of NaOH [6]. This high pH environment surrounding the overpack is expected to endow passivity to carbon steel and thus the corrosion of the overpack is primarily related to passivity and passivity breakdown.

One of the important features of this multi-barrier system of Supercontainer is that the annular space between overpack and envelope is isolated from the clay environment by the stainless steel envelope, in which case the inventory of oxygen and water is fixed. The oxygen gas trapped inside the annular space will be gradually consumed by corrosion occurring simultaneously at the outer surface of carbon steel overpack and inner surface of stainless steel envelope. The decreasing oxygen partial pressure will drive the corrosion potential of the carbon steel overpack and the stainless steel envelope in the negative direction, and at a certain point the potential will be sufficiently negative to render hydrogen evolution the predominant cathodic reaction. The process of hydrogen evolution at the steel surfaces primarily takes the form of water reduction, rather than proton reduction, because of the very low concentration of the latter ($10^{-13.5}$ M), and continuously produces hydrogen gas in the annulus containing the concrete buffer. Assuming the air tightness of the stainless steel envelope is sufficient that the hydrogen gas cannot escape, the annulus will become pressurized, which further lowers the corrosion potential. Accordingly, the research presented in this report was focused on studying the corrosion behavior of carbon steel under anoxic conditions characterized by very negative corrosion potentials.

At such negative potentials, the cathodic reaction dominates the corrosion system and thus the information regarding to the partial anodic process, which is required to study the passivity electrochemically, such as the anodic corrosion current density and the impedance associated with the anodic reactions, cannot be obtained directly, a subject that will be addressed in Chapter 5 and 6. Additionally, the passive carbon steel also exhibits apparent corrosion irreversibility when the film formation potential shifts in opposite anodic and cathodic directions; specifically, a strong resistance to cathodic potential reduction of the passive state is evident if a pre-exiting passive film has been developed during earlier anodic polarization. This type of irreversibility is typically observed in the cyclic voltammogram obtained on iron and steels [9-17], in which the potentials of the oxidation and reduction peaks for one redox reaction are always found non-coincident to each other. Numerous studies using various types of non-electrochemical characterization techniques such as XANES [18, 19], ellipsometry [20], XPS [21], SIMS [22, 23] et al. also reported the persistence of the passive film on iron in alkaline solutions upon cathodic reduction, manifested by the resilient residual iron oxide that cannot be completely removed by cathodic polarization. Nevertheless, few studies have been done to investigate this behavior in detail and, hence, did not define the essential mechanism that causes the irreversible polarization. As will be shown in the

next section, passivity is a kinetic phenomenon controlled by generation and annihilation of point defects at the metal/barrier layer (m/bl) and the barrier layer/outer-layer (bl/ol) interface, as proposed in the PDM, and thus, the irreversibility of passivity is likely to be associated with certain kinetic processes that do not respond equivalently when the potential is shifted in opposite directions. From this perspective, this work also aims to gain deeper understanding of the fundamental source of the kinetic irreversibility of the passive film on carbon steel under anoxic conditions by performing short term experiments and employing the mixed potential model to describe the overall corrosion process and hence to analyze the experimental data.

2.3 Analytic Models for Passivity and the Point Defect Model

As discussed in Chapter 1, analytic or mechanistically based models are necessary to establish an effective prediction of corrosion damage over exceptionally long periods. Ever since the discovery of passivity by Faraday, numerous models have been postulated to account for this phenomenon.

Table 2-2 compares a few prominent models that have been widely recognized within the field of passivity research. Verwey's high field model [24] (HFM) is applicable to cation conductors, in which cation motion in the oxide passive film is the rate-controlling step, while Cabrera-Mott's model [25], also for cation conductors, regards cation injection from metal into film as the rate-controlling step. In both of these models, the film grows at the film/solution interface, and hence it is not obvious how the models can account for the commonly observed bilayer structure. Both of these models predict transient changes of current density and film thickness with time, but neither predicts the existence of steady states in these properties at finite times. Vetter and Gorn [26] developed a model for the passive film on iron that recognized the existence of potential drops across the interfaces. However, this model makes predictions only with respect to the transient current behavior. The place exchange model [27] (PEM) postulates cooperative cation/anion exchange and injection of oxygen ion into the film as the rate-determining steps. The model predicts transient current density and film thickness behavior, but it does not account for the steady state.

Table 2-2: The comparison of the prominent analytical models for describing passive film.

Models	Differential Rate Laws	Predictions	Observations
PDM	$\frac{dL}{dt} = a \cdot e^{-bL} - c$	• Depassivation when $dL/dt < 0$. • Steady state film thickness and current density when $0 < c < a$.	• Observed • Observed
HFM	$\frac{dL}{dt} = a' \cdot e^{b'/L}$	• No depassivation. • Barrier layer grows monotonically to infinite thickness. • Current goes to zero as $L \to \infty$ • Infinite growth rate at $L = 0$	• Incorrect • Not observed • Not observed • Non-physical
PEM	$\frac{dL}{dt} = a'' \cdot e^{-b''L}$	• No depassivation. • Barrier layer grows monotonically to infinite thickness. • Current goes to zero as $L \to \infty$	• Incorrect • Not observed • Not observed

The point defect model (PDM) has been developed by Macdonald et al. to describe the passivity behavior of metals and alloys at an atomic scale [28, 29], and a large amount of empirical and simulative evidence has attested that this model is able to account successfully for essentially all observations on the properties and structure of passive films. So far, the PDM has no known conflicts with experiment and has resulted in the prediction of several phenomena that were previously unknown or not fully recognized in the field.

2.3.1 The PDM for the Steady State of Passivity

The PDM envisions that the passive film comprises a bi-layer structure consisting of a highly point-defective oxide barrier layer that grows into the metal at the metal/barrier layer (m/bl) interface and a precipitated outer layer that forms via the hydrolysis of metal cations that are transmitted through the barrier layer and are ejected at the barrier layer/solution (bl/s) interface and/or by the dissolution of the barrier layer itself at the same location. In the case of carbon steel in contact with highly alkaline concrete pore solution, the outer-layer of the passive film is porous and not point-defective, primarily comprising hydroxide and/or oxy-hydroxide [$Fe(OH)_2$/$Fe(OH)_3$/FeOOH] that is generated by precipitation of iron cations ejected from the barrier layer with OH^- in solution.

The PDM then postulates that the growth of the barrier layer of the passive film is governed by the generation and annihilation of point defects at the m/bl and bl/s interfaces and that these reactions essentially establish the point defect concentrations in the barrier layer. The point defects that are considered in the model are cation and oxygen vacancies and metal interstitials; oxygen interstitials are not considered, because they are too large to move through most oxide lattices except possibly at very high temperatures.

Seven elemental defect reactions occurring at the m/bl and bl/s interfaces are proposed in the PDM, as shown in Figure 2-2. Because the growth direction of the barrier layer is into the metal substrate, the origin point of the *x* axis (x = 0) is located at bl/s interface, which may or may not coincide with the original metal/solution (m/s) interface. From these defect generation and annihilation reactions, combined with constraints of the relevant natural laws (e.g. mass and charge conservation, equivalence of mass-charge as in Faraday's law), equations describing the kinetics of the growth and dissolution of the passive film along with mass and charge transfer through the film can be derived. Corresponding coefficients and rate constants for each interfacial reaction are listed in Table 2-3; in these expressions, α is the polarizability of the bl/s interface; β is the dependence of the potential drop across the bl/s interface upon pH, and α_i and k_i^0 are respectively the transfer coefficient and the standard rate constant for the *j*th reaction in Figure 2-2, $\gamma = F/RT$, $K = \gamma\varepsilon$, and ε is the electric field strength within the barrier layer, F is Faraday's constant. The apparent rate constant k_i is then defined as:

$$k_i = k_i^0 e^{a_i V} e^{b_i L} e^{c_i pH} \tag{2-1}$$

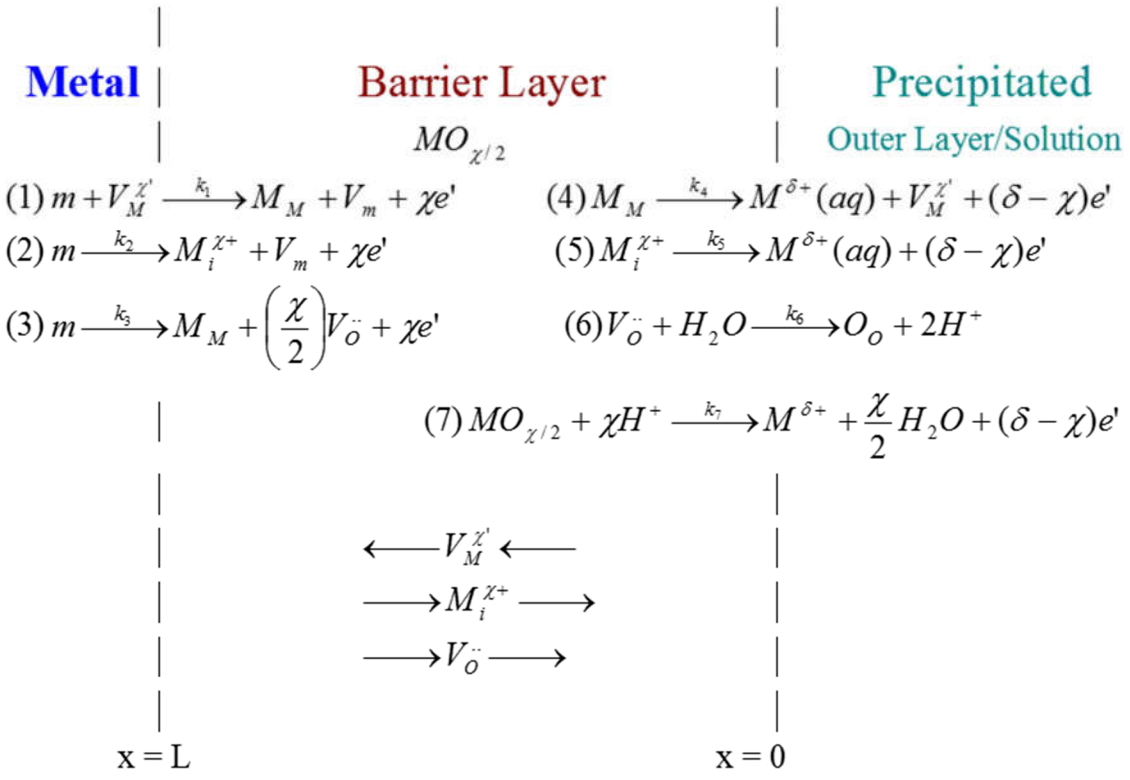

Figure 2-2: Summary of the defect generation and annihilation reactions envisioned to occur at the interfaces of the barrier oxide layer on a metal, according to PDM. $V_M^{\chi'} \equiv$ cation vacancy, $M_i^{\chi^+} \equiv$ cation interstitial, $V_O^{\cdot\cdot} \equiv$ oxygen (anion) vacancy, $M^{\delta^+}(aq) \equiv$ cation in outer layer/solution interface, $M_M \equiv$ cation in cation site on the cation sublattice, $O_O \equiv$oxide ion in anion site on the anion sublattice, $MO_{\chi/2} \equiv$ stoichiometric barrier layer oxide, $V_m \equiv$vacancy in metal substrate.

Table 2-3: Coefficients for the rate constants for the reactions that generate and annihilate point defects at the m/bl interface (Reactions 1 – 3) and at the bl/ol interface (Reactions 4 – 6), Figure 2-2, and for dissolution of the film (Reaction 7). $k_i = k_i^0 e^{a_i V} e^{b_i L} e^{c_i \mathrm{pH}}$.

Reactions	a_i **(V^{-1})**	b_i **(cm^{-1})**	c_i	**Units of k_i^o**
(1) $m + V_M^{\chi'} \xrightarrow{k_1} M_M + v_m + \chi e'$	$\alpha_1(1\text{-}\alpha)\ \chi\gamma$	$-\alpha_1\chi K$	$-\alpha_1\beta\chi\gamma$	s^{-1}
(2) $m \xrightarrow{k_2} M_i^{\chi+} + v_m + \chi e'$	$\alpha_2(1\text{-}\alpha)\ \chi\gamma$	$-\alpha_2\chi K$	$-\alpha_2\beta\chi\gamma$	$\frac{\mathrm{mol}}{\mathrm{cm^2\ s}}$
(3) $m \xrightarrow{k_3} M_M + \frac{\chi}{2} V_{\ddot{O}} + \chi e'$	$\alpha_3(1\text{-}\alpha)\ \chi\gamma$	$-\alpha_3\chi K$	$-\alpha_3\beta\chi\gamma$	$\frac{\mathrm{mol}}{\mathrm{cm^2\ s}}$
(4) $M_M \xrightarrow{k_4} M^{\Gamma+} + (\delta - \chi)e'$	$\alpha_4\alpha\delta\gamma$		$\alpha_4\beta\delta\gamma$	$\frac{\mathrm{mol}}{\mathrm{cm^2\ s}}$
(5) $M_i^{\chi+} \xrightarrow{k_5} M^{\Gamma+} + (\Gamma - \chi)e'$	$\alpha_4\alpha\delta\gamma$		$\alpha_5\beta\delta\gamma$	$\frac{\mathrm{cm}}{\mathrm{s}}$
(6) $V_{\ddot{O}} + H_2O \xrightarrow{k_6} O_O + 2H^+$	$2\alpha_4\alpha\gamma$		$\alpha_6\beta\delta\gamma$	$\frac{\mathrm{cm}}{\mathrm{s}}$
(7) $MO_{\chi/2} + \chi H^+ \xrightarrow{k_7}$ $M^{\Gamma+} + \frac{\chi}{2} H_2O + (\Gamma - \chi)e'$	$\alpha_7\alpha\ (\delta\text{-}\chi)\gamma$		$\alpha_7(\delta\text{-}\chi)\beta\gamma$	$\frac{\mathrm{mol}}{\mathrm{cm^2\ s}}$

The total electron current density, i_{total}, which is sensed in an external circuit, is given by:

$$i_{total} = F[\chi k_1 C_v^L + \chi k_2 + \chi k_3 + (\delta - \chi)k_4 + (\delta - \chi)k_5 C_i^0 + (\delta - \chi)k_7] \quad (2\text{-}2)$$

where C_v^L is the concentration of cation vacancies at metal/barrier layer (m/bl) interface and C_i^0 is the concentration of cation interstitials at barrier layer /outer layer (bl/ol) interface. Note that Eq. (2-1) does not depend upon the concentration of oxygen vacancies or upon the rate constant for Reaction (6), Figure 2-2. Thus, no relaxations in the impedance response involve oxygen vacancies, but this is essentially an artifact of considering Reaction (3), Figure 2-2 to be irreversible. If this reaction was considered to be reversible, then a relaxation involving oxygen vacancies would be present. Furthermore, the concentration of H^+ is considered to be constant and is included in the definition of k_7, as indicated in Eq. (2-5).

Using the method of partial charges, the rate constants for the reactions are found to be of the form:

$$k_i = k_i^0 \exp[a_i(V - R_{ol} i_{total}) - b_i L], \quad i = 1,2,3 \quad (2\text{-}3)$$

$$k_i = k_i^0 \exp[a_i(V - R_{ol} i_{total})], \quad i = 4,5 \quad (2\text{-}4)$$

$$k_7 = k_7^0 \exp[a_7(V - R_{ol} i_{total})] \left(\frac{C_H}{C_H^0}\right)^n \quad (2\text{-}5)$$

where n is the kinetic order of barrier layer dissolution with respect to H^+. In deriving these expressions, it is assumed that a resistive outer layer exists on the surface of the barrier layer and that the passive current flows through the barrier layer to a remote cathode, which is the normal experimental configuration. Because of this, the potential that exists at the barrier layer/outer layer interface must be corrected from that applied at the reference electrode located at the outer layer/solution interface by the potential drop across the outer layer, where R_{ol} ($\Omega \cdot cm^2$) is the specific resistance of the outer layer.

It has been clarified [28-30] that Reactions (3) and (7) are lattice non-conservative and they create and destroy the minimal units of the barrier layer ($MO_{\chi/2}$), respectively. Thus, the rate of growth of the barrier layer into the metal at the m/bl interface, (dL^+/dt), and the rate of dissolution rate of the barrier layer, (dL^-/dt), at the bl/ol interface can be written as:

$$dL^+/dt = \Omega k_3 \quad (2\text{-}6)$$

and

$$\mathrm{d}L^{-}/\mathrm{d}t = \Omega k_7 (C_H/C_H^0)^n \tag{2-7}$$

where Ω is molar volume of the barrier layer per cation. When the rates of these two processes are equal, the steady state is reached, and the steady-state barrier layer thickness, L_{ss}, can be expressed as:

$$L_{ss} = \left(\frac{a_7 - a_3}{b_3}\right) V + \left(\frac{c_7 - c_3}{b_3}\right) \mathrm{pH} + \frac{1}{b_3} \ln\left[\frac{k_7^0}{k_3^0} (C_H/C_H^0)^n\right] \tag{2-8}$$

Substitution for the coefficients from Table 2-3 finally yields:

$$L_{ss} = \frac{1}{\varepsilon}\left[1 - \alpha - \frac{\alpha\alpha_7}{\alpha_3}\left(\frac{\delta}{\chi} - 1\right)\right] V - \frac{\beta}{\varepsilon}\left[\frac{\alpha_7}{\alpha_3}\left(\frac{\delta}{\chi} - 1\right) + 1\right] \mathrm{pH} - \frac{1}{\alpha_3 \chi \varepsilon \gamma} \ln\left[\frac{k_7^0}{k_3^0}\left(\frac{C_H}{C_H^0}\right)^n\right] \tag{2-9}$$

For the case where no change occurs in the oxidation state of the cation upon ejection from the barrier layer via Reactions (4) and (5) or upon dissolution of the film, $\chi = \delta$, and Eq. (2-9) reduces to simpler form as:

$$L_{ss} = \frac{1}{\varepsilon}(1 - \alpha) V - \frac{1}{\varepsilon}\left(\frac{2.303n}{\alpha_3 \chi \gamma} - \beta\right) \mathrm{pH} - \frac{1}{\alpha_3 \chi \varepsilon \gamma} \ln\left[\frac{k_7^0}{k_3^0}\right] \tag{2-10}$$

Eq. (2-10) shows that the steady state thickness of barrier layer increases linearly with increasing applied potential with an anodizing constant of $(1 - \alpha)/\varepsilon$ at fixed pH. The anodizing constant is predicted to be, typically, 1.2 – 2.5 nm/V, which is in excellent agreement with experiment results reported previously [31].

From Eqs. (2-1) to (2-10) and by accepting the definitions of the rate constants given in Table 2-3, we obtain the total passive current density in the steady state in the final form:

$$i_{ss} = \delta F[k_2^0 e^{a_2 V} e^{b_2 L_{ss}} e^{c_2 \mathrm{pH}} + k_4^0 e^{a_4 V} e^{c_4 \mathrm{pH}} + k_7^0 e^{a_7 V} e^{c_7 \mathrm{pH}} \cdot (C_H/C_H^0)^n] \tag{2-11}$$

2.3.2 The PDM for the Passivity Breakdown

The passive state is not absolutely protective and passivity breakdown occurs for various reasons, giving rise to enhanced general corrosion rate or to localized corrosion. Localized passivity breakdown is especially of great concern, because it results in the nucleation and propagation of pits and the subsequent nucleation and growth of cracks provided that there is sufficient tensile stress in the system to initiate crack nucleation at the stress raiser represented by the pit. Of particular concern is localized passivity breakdown, which results in the nucleation and growth of pits and subsequently the nucleation and growth of cracks if the requisite tensile stress is present in the system to cause crack nucleation at the stress raiser represented by the pit.

Passivity breakdown is expected to occur to the carbon steel overpack if the exterior stainless steel envelope is breached and aggressive species, such as chloride, sulfide, etc., diffuse to the overpack surface. As shown in Table 2-2, the PDM is the only analytical model that can account for the experimental observations of passivity breakdown. With respect to passivity breakdown, it is clearly evident that any deterministic model for describing pit nucleation rate must simultaneously describe the properties of the passive film existing on a metal surface and clearly specify the criteria for passivity breakdown itself.

A review of the literature reveals the following generalizations of the experimental data for passivity breakdown of metals and alloys in a wide variety of environments [32-39]:

(i) Localized corrosion is initiated by passivity breakdown and occurs on a wide variety of passive metals and alloys in a wide variety of environments.

(ii) Certain species (e.g., Cl^- and Br^-) induce passivity breakdown by interacting with the defective barrier oxide layer of the passive film. These aggressive species apparently do not penetrate through the barrier layer, but may be incorporated into the precipitated outer layer, which has led to reports that the halide ions are incorporated into or have penetrated through the barrier layer of the passive film [39].

(iii) Passivity breakdown occurs at a wide variety of sites on metal and alloy surfaces.

(iv) Passivity breakdown is a dynamic, deterministic process, being predetermined and (in principle) predictable on the basis of known physical laws [40].

(v) The transition of a meta-stable pit to a stable pit is a rare event.

(vi) Two fundamentally different repassivation phenomena may be identified: (a) "Prompt" repassivation and (b) "delayed" repassivation (sometimes referred to as "stifling"). Prompt repassivation determines the "survival probability" of metastable pits in their transition to stable pits and delayed repassivation determines the rate at which stable pits die.

(vii) A single passivity breakdown site is characterized by a critical voltage (V_b) and induction time (t_{ind}). V_b is found to be near-normally distributed while t_{ind} displays a left acute distribution. The parameters V_b (and $\overline{V_b}$) and t_{ind} exhibit highly characteristic dependencies on the activities of the breakdown-inducing aggressive species ($[X^-]$) and on the applied voltage (t_{ind} only) for a wide variety of systems, suggesting commonality in mechanism.

(viii) V_b (and$\overline{V_b}$) is found to depend on the identity of the aggressive ion within a homologous series. Thus, in the case of iron, nickel, and their alloys with chromium (e.g. the stainless steels) the propensities of the halide ions for inducing passivity breakdown lie as $F^- < Cl^- > B^- < I^-$, whereas, in the case of titanium, bromide ion is the most aggressive. These trends are readily explained by the absorption of the halide into oxygen vacancies in the surface of the barrier layer, with the extent of absorption being determined by the competitive needs to dehydrate the ion and expand the vacancy [40].

(ix) The mean breakdown voltage, $\overline{V_b}$, is found to decrease linearly with log([X^-]) with a slope that exceeds 2.303*RT/F*, which is attributed to the value of the polarizability of the bl/s interface (α) lying between 0 and 1, for essentially all systems (metal/solution) that have been investigated. Likewise, the induction time, again for essentially all systems that have been carefully investigated, displays a common form of the dependencies of log(t_{ind}) on potential and [X^-]. These relationships, again, strongly suggest commonality in breakdown mechanism.

(x) Certain oxyanions (e.g. nitrate, borate, and nitrite) inhibit passivity breakdown, with the effect being accounted for by competitive absorption of the inhibitor with the aggressive anion into surface oxygen vacancies in the barrier layer [41].

(xi) In many systems (e.g. Al, Ga, Zr, stainless steel), blister formation is observed to be the precursor to passivity breakdown.

(xii) Certain alloying elements (e.g., Mo and W in Fe-Cr alloys) cause a positive shift in V_b (and $\overline{V_b}$) and in a lengthening of the induction time [42]. The effect is greater for a larger difference in the oxidation states between the solute and host.

(xiii) Incident electromagnetic radiation, with a photon energy that is greater than the band-gap of the barrier layer oxide, also results in a positive shift in V_b (and$\overline{V_b}$), and in a lengthening of the induction time [43-45]. The defect (electronic and crystallographic) structures of the barrier layer are modified by irradiation.

The PDM, as it relates to passivity breakdown, postulates that certain aggressive anions, e.g., F^-, Cl^-, Br^-, and I^- absorb into oxygen vacancies in the surface of the barrier layer, resulting in the generation of cation vacancies ($V_M^{\chi'}$) and hence to an enhanced flux of the same species across the barrier layer toward the m/bl interface, as depicted in Figure 2-3 [38]. The model postulates that, if the cation vacancies arriving at the m/bl interface cannot be annihilated at a sufficiently high rate via the reaction $m + V_M^{\chi'} \rightarrow M_M + v_m + \chi e^-$, the excess vacancies will condense locally on the cation sub-lattice or on the substrate metal lattice at the m/bl interface and hence cause local separation of the barrier layer from the substrate metal. Once separation has occurred, the barrier layer at that locale can no longer grow into the metal via the Reaction (3), $m \rightarrow M_M + \frac{\chi}{2} V_O^{\bullet\bullet} + \chi e^-$, which generates new film [represented here as $M_M + \frac{\chi}{2} V_O^{\bullet\bullet} \equiv M\left(V_O^{\bullet\bullet}\right)_{\varphi/2}$ on the premise that an oxygen vacancy can be treated as an oxygen anion (equivalent sites on the anion sub-lattice)]. However, the barrier layer continues to grow into the metal at the periphery of the cation vacancy condensate (Figure 2-3), where the m/bl interface is still intact,

and also continues to dissolve at the bl/s interface via Reaction (7), $MO_{\chi/2} + \chi H^+ \rightarrow M^{\delta+} + \frac{\chi}{2} H_2O + (\delta - \chi)e^-$. This results in local thinning of the "cap" over the cation vacancy condensate with the cap eventually rupturing, due to the growth stresses in the film and in the near-surface substrate. The predicted thinning has been detected using micro-ellipsometry [46]. In the view of the PDM, the "weak points" on the surface, where passivity breakdown is predicted to occur, correspond to regions of high cation vacancy flux and likely high cation vacancy diffusivity. These regions are identified as being regions of high local discontinuity in the barrier layer, such as the points of intersection of the barrier layer with precipitates, inclusions (e.g., MnS), and other "second phase" particles, grain boundaries between nano-crystallites of the barrier layer [47], and metal dislocations that project through the barrier layer.

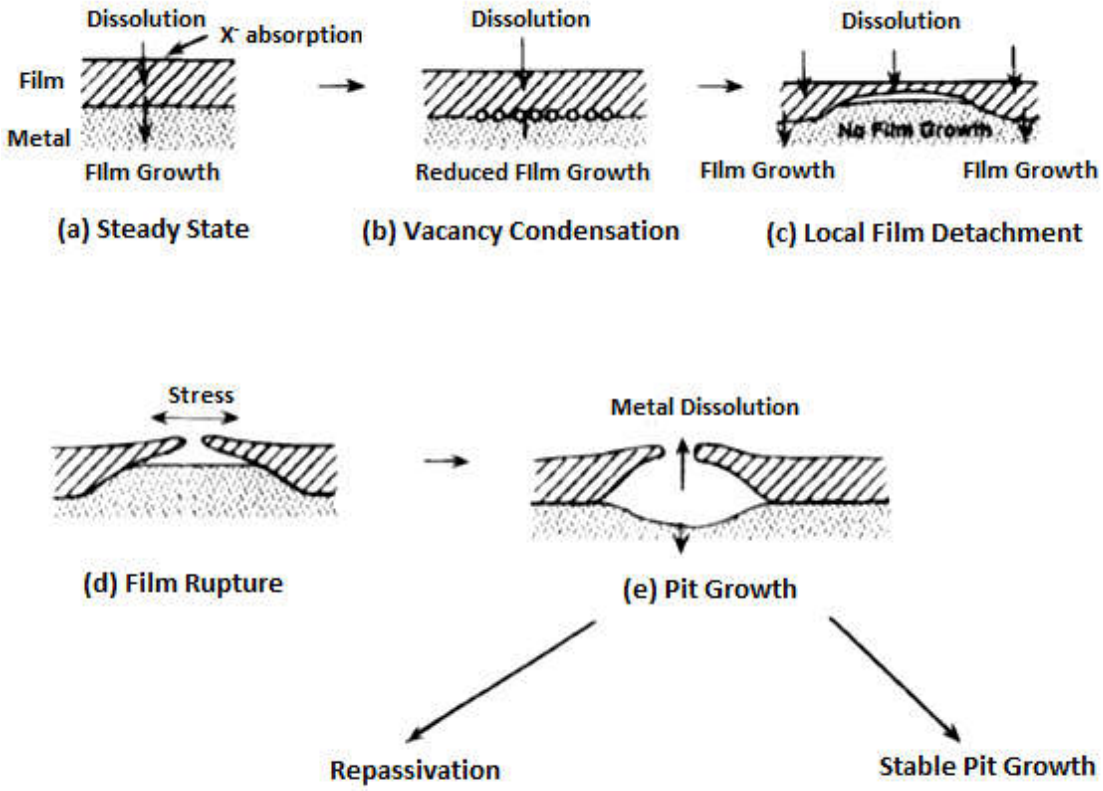

Figure 2-3: Cartoon displaying the sequence of events in passivity breakdown, according to the Point Defect Model. Note that the initial event is the absorption of an aggressive anion into an oxygen vacancy at the film/solution interface (a), resulting in an enhanced flux of cation vacancies across the film and eventually in condensation of cation vacancies at the metal/film interface (b). The film stops growing into the metal beneath the cation vacancy condensate while it continues to dissolve at the film/solution interface (c), eventually resulting in rupture (d) and repassivation or the formation of a stable pit (e). Adapted from Ref. [39].

Additional support for the mechanism of passivity breakdown proposed by the PDM also stems from the almost general observation of the formation of blisters (cation vacancy condensate) as precursors to passivity breakdown on a variety of metals and alloys, the passivity breakdown on liquid versus solid gallium, and the potential sweep rate dependence of the apparent breakdown voltage [48-50]. The latter evidence is particularly convincing, because the test involves no adjustable parameters and yields a quantity (the concentration of condensed vacancies) that can be compared with the same quantity calculated from fundamental principles (crystal structure of the barrier layer).

The postulated mechanisms for the generation of cation vacancies at the barrier layer/solution interface via the absorption of an aggressive anion into a surface oxygen vacancy are summarized in Figure 2-4 [39]. The initial event is the absorption of a chloride ion into a surface oxygen vacancy as depicted in the figure. This process involves two more fundamental processes; dehydration of $X^{-}\cdot nH_2O$ and expansion of the surface oxygen vacancy to the size necessary to accept the aggressive anion. Considering the halide homologous series, ranked according to ion size, $F^- < Cl^- < Br^- < I^-$, the standard Gibbs energy of absorption of a halide into an oxygen vacancy, i.e.

$$Cl^-.nH_2O + V_O^{\cdot\cdot} = Cl_O^{\cdot} + nH_2O \tag{2-I}$$

can be split into two more fundamental processes

$$Cl^-.nH_2O = Cl^- + nH_2O \tag{2-II}$$

$$Cl^- + V_O^{\cdot\cdot} = Cl_O^{\cdot} \tag{2-III}$$

Thus, the change in the standard Gibbs energy for the absorption of X^- into a surface oxygen vacancy can be written as:

$$\Delta G_A^0 = \Delta G_{dehyd}^0 + \Delta G_{exp}^0 \tag{2-12}$$

where ΔG_{dehyd}^0 and ΔG_{exp}^0 are the changes in the standard Gibbs energies for anion dehydration [Reaction (2-II)] and surface oxygen vacancy expansion [Reaction (2-III)], respectively. Thermodynamic data and analysis shows that ΔG_{dehyd}^0 becomes less positive along the homologous halide series, corresponding to weaker hydration as the aggressive anion radius increases. On the other hand, if the anion radius is less than the radius of a surface oxygen vacancy (F^- and Cl^- in their absorption into surface oxygen vacancies in the passive films on iron, nickel, and stainless steels), no vacancy expansion is required to insert the anion and ΔG_{exp}^0 is independent

of anion size. For larger anions (Br^- and I^-), however, significant work is incurred in expanding the surface oxygen vacancy resulting in a positive change in the standard Gibbs energy for absorption ΔG^0_{exp} that becomes increasingly larger with anion size. The analysis predicts that the resulting breakdown potential [See later; Eq. (7-2)] should pass through a minimum at an anion radius corresponding to that for chloride, in agreement with experiment for passivity breakdown on iron, nickel, and stainless steels.

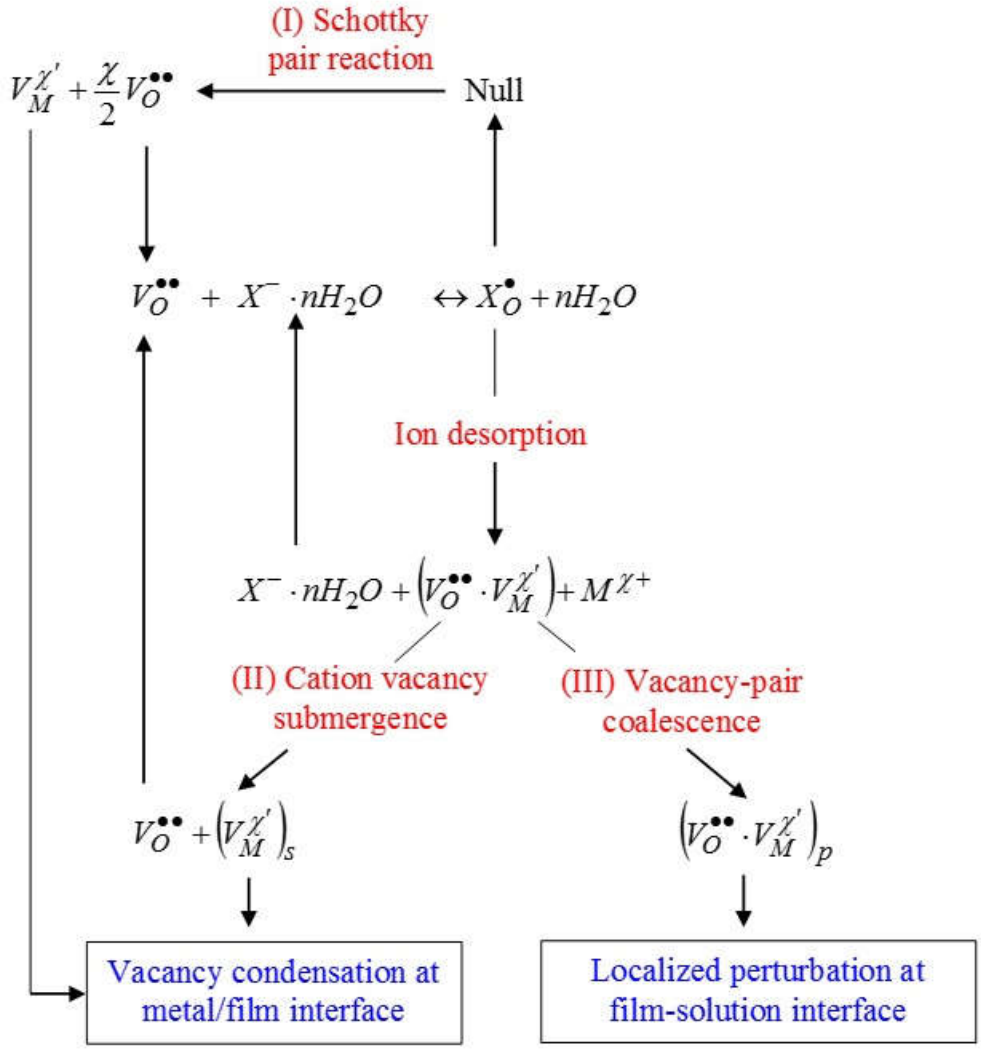

Figure 2-4: Postulated mechanisms for the chloride-induced generation of cation vacancies at the barrier/layer interface [39].

2.4 Nucleation of Metastable Pits on Metal Surfaces

Metastable pitting, in which passivity breakdown occurs followed immediately by repassivation, is now well-accepted as being an integral part of the process of pitting corrosion on a metal or alloy, culminating in the accumulation of damage via the development of stable pits. It is also well-recognized that repassivation reflects the failure on the part of the pit nucleus to establish differential aeration, which is necessary for the build-up and maintenance of the aggressive conditions of high [Cl^-] and high [H^+] (low pH) that cause the pits to grow as stable pits, until they, too, die via delayed repassivation (due to the inability of the pit to maintain differential aeration, because of the limited availability of resources of oxygen reduction on the external surfaces).

Numerous authors have reported metastable pit nucleation rate data measured under more-or-less well-defined conditions. Williams et al. [51-53] found a proportional correspondence for Type 304L SS between the nucleation frequency of metastable pits and the frequency of occurrence of propagating (stable) pits, that is $\Lambda = \lambda \exp(-\mu\tau_c)$, where Λ and λ are the rates of nucleation of stable pits and metastable pits, respectively, μ is probability of repassivation with a unit of s^{-1} for a single metastable pit, and the term $\exp(-\mu\tau_c)$ is the "probability of survival of a single (metastable pitting) event for time τ_c" [52], i.e. the rate of nucleation of stable pits is the product of the nucleation rate of metastable pits and the survival probability. They also found that the initiation rate of pitting corrosion on Type 304L SS in chloride solutions increased with chloride concentration and the metastable pitting could occur at potentials cathodic to the critical pitting potential, even in very dilute chloride solution (10 ppm), indicating a finite possibility of pitting under these circumstances. Reuter and Heusler [54] reported that the growth of surface concentration of pits on passive iron in chloride-containing borate buffer solutions accelerated to a maximum rate shortly after the first pitting incidence, and, after a certain characteristic time, a steady-state surface concentration of pits was reached. Fratesi [55] studied the pitting on Type 316L SS using both potentiodynamic polarization and the surface scratching method under potentiostatic polarization, and later developed a statistical method postulating that the scattering of the pitting potential values of Type 316L SS in chloride solutions can be attributed to the stochastic nature of pit generation. The term "stochastic", which is usually used to imply that the underlying mechanism of a process is fundamentally random and "unknowable", is inappropriate in describing pitting corrosion and the term should be dropped from our lexicon, primarily because passivity breakdown and subsequent pitting are deterministic in that they occur for well understood, mechanistic reasons in accordance with the natural laws [56].

Burstein and colleagues [57-61] performed extensive work studying the kinetics of the metastable pitting on Type 304 SS and 316L SS surfaces in chloride-containing solutions. They found that all experimentally observed pits were metastable initially and, conforming to the earlier discovery of Frankel et al. [35], that the achievement of a critical value of the pit stability product is necessary for metastable pits to transform into stable pits. They also discovered that the rate of occurrence of metastable pitting in their solutions depended on potential and chloride concentration, but, evidently, not on the electrolyte pH. These observations were interpreted in terms of their hypothesis that the propensity of a site to form a metastable pit depends on its original geometry; deeper and narrower sites are more susceptible to metastable pitting and can be activated at lower potentials and lower chloride concentration, while the opposites apply to shallower and

open sites, but this is not consistent with the observed passivity breakdown on atomically-smooth surfaces, such on liquid gallium [48].

Burstein and Mattin [57], suggest that passivity breakdown gives rise to current pulses that are of the pA order in magnitude. However, in the light of much work on the origin of electrochemical noise [62-64], it is evident that there are many processes, other than passivity breakdown, that give rise to noise at a passive metal interface, such as bubble detachment, the "flickering" of anodic and cathodic sites across the surface, as in general corrosion, and possibly the existence of intermittently active, low impedance paths along emergent grain boundaries in the nano-crystalline passive film. These paths are intermittent, because the barrier layer continuously forms at the metal/film interface and dissolves at the film/solution interface, so that the grain boundaries between the nano-crystallites are continuously redistributed with time. All of these processes can give rise to the pA pulses referred to by Burstein and Mattin, but no way exists for delineating them with regard to their source and it is for this reason that they are not generally counted as originating from passivity breakdown, as defined in this work.

It has also been found that incident, supra band-gap light inhibits passivity breakdown [43-45]. This inhibitive effect was reported to be surprisingly strong for nickel in chloride solutions and does not find explanation in any of the mechanistic postulates of the studies mentioned above, indicating that passivity breakdown is physico-electrochemically much more complex than can be accounted for by any geometric model, such as that proposed by Burstein et.al. [6-10] Recognizing that incident radiation perturbs the electronic structure of the passive film, but that breakdown must involve the crystallographic (point defect) structure, it is evident that the two structures are tightly coupled.

An important process in the development of pitting damage is the initial passivity breakdown event and, indeed, any model that is developed to predict the accumulation of pitting damage must address the kinetics of metastable pit nucleation. Numerous models have been proposed for passivity breakdown [35, 52, 58, 65], and the Point Defect Model (PDM) is one of the only a few that has been demonstrated [50, 66, 67] to be capable of yielding relationships between the dependent (e.g. pitting potential and induction time) and the common independent (e.g. $[Cl^-]$, pH, voltage) variables that permit quantitative assessment against experiment. The theory of the kinetics of metastable pit nucleation in terms of the PDM has been previously developed and has been discussed elsewhere [37, 40, 56]. Nevertheless, the theory has not been previously evaluated against experimental data. The present work, for the first time, applies the theory to the analysis of metastable pit nucleation rate data by performing optimization of the kinetic model on multiple sets of independently-determined experimental data on metastable pitting nucleation, which have been published in the literature. In Chapter 7, the theory has been successfully tested, and important parameters that govern the kinetics of metastable pits nucleation have been obtained from the optimization and are analyzed.

References

[1] F.S.P. IAEA, Vienna: International Atomic Energy Agency, (2006).
[2] J. Bel, A. Van Cotthem, C. De Bock, Paper ICEM05-1339 in "Proceedings of ICEM, 5 (2005) 4-8.
[3] S. Wickham, Galson Sciences, UK, (2005).
[4] J.J. Bel, S.M. Wickham, R.M. Gens, Proc. MRS Proceedings, 2006.
[5] S. Wickham, 1st full draft report, Report no. NIROND-TR, (2007).
[6] L. Wang, External Report of the Belgian Nuclear Research Centre, sck• cen-er-17, (2009).
[7] P. Van Marcke, W. Wacquier, Proc. ASME 2013 15th International Conference on Environmental Remediation and Radioactive Waste Management, 2013.
[8] E. Weetjens, J. Marivoet, J. Govaerts, B. Leterme, Report No. SCK• CEN-ER-215, SCK• CEN, Belgium, (2012).
[9] Z.J. Lu, D.D. Macdonald, Electrochim Acta, 53 (2008) 7696-7702.
[10] G. Bignold, Corros Sci, 12 (1972) 145-154.
[11] R.S. Guzman, J. Vilche, A. Arvia, Electrochim Acta, 24 (1979) 395-403.
[12] A. Wieckowski, E. Ghali, Electrochim Acta, 30 (1985) 1423-1431.
[13] D. Oelkrug, M. Fritz, H. Stauch, J Electrochem Soc, 139 (1992) 2419-2424.
[14] L. Veleva, M.A. Alpuche-Aviles, M.K. Graves-Brook, D.O. Wipf, J Electroanal Chem, 537 (2002) 85-93.
[15] S. Joiret, M. Keddam, X.R. Novoa, M.C. Perez, C. Rangel, H. Takenouti, Cement Concrete Comp, 24 (2002) 7-15.
[16] D.D. Macdonald, D. Owen, J Electrochem Soc, 120 (1973) 317-324.
[17] M. Valcarce, M. Vázquez, Electrochim Acta, 53 (2008) 5007-5015.
[18] A.J. Davenport, J.A. Bardwell, C.M. Vitus, J Electrochem Soc, 142 (1995) 721-724.
[19] P. Schmuki, S. Virtanen, A.J. Davenport, C.M. Vitus, J Electrochem Soc, 143 (1996) 574-582.
[20] Z. Szklarska‐Smialowska, T. Zakroczymski, C.J. Fan, J Electrochem Soc, 132 (1985) 2543-2548.
[21] S. Haupt, H. Strehblow, Langmuir, 3 (1987) 873-885.
[22] J.A. Bardwell, B. MacDougall, M. Graham, J Electrochem Soc, 135 (1988) 413-418.
[23] J.A. Bardwell, G.I. Sproule, D.F. Mitchell, B. MacDougall, M.J. Graham, J. Chem. Soc., Faraday Trans., 87 (1991) 1011-1019.
[24] E. Verwey, Physica, 2 (1935) 1059-1063.
[25] N. Cabrera, N. Mott, Reports on progress in physics, 12 (1949) 163.
[26] K. Vetter, F. Gorn, Electrochim Acta, 18 (1973) 321-326.
[27] N. Sato, M. Cohen, J Electrochem Soc, 111 (1964) 512-519.
[28] L.F. Lin, C.Y. Chao, D.D. Macdonald, J Electrochem Soc, 128 (1981) 1194-1198.
[29] C.Y. Chao, L.F. Lin, D.D. Macdonald, J Electrochem Soc, 128 (1981) 1187-1194.
[30] C.Y. Chao, L.F. Lin, D.D. Macdonald, J Electrochem Soc, 129 (1982) 1874-1879.
[31] D.D. Macdonald, Pure Appl. Chem, 71 (1999) 951-978.
[32] G. Burstein, C. Liu, R. Souto, S. Vines, Corrosion Engineering, Science and Technology, 39 (2004) 25-30.
[33] G. Frankel, J Electrochem Soc, 145 (1998) 2186-2198.
[34] Z. Szklarska-Smialowska, Corrosion, 27 (1971) 223-233.
[35] G. Frankel, L. Stockert, F. Hunkeler, H. Boehni, Corrosion, 43 (1987) 429-436.
[36] D.E. Williams, J. Stewart, P.H. Balkwill, Corros Sci, 36 (1994) 1213-1235.

[37] L. Lin, C. Chao, D. Macdonald, J Electrochem Soc, 128 (1981) 1194-1198.
[38] D.D. Macdonald, Pure and Applied Chemistry, 71 (1999) 951-978.
[39] D.D. Macdonald, J Electrochem Soc, 139 (1992) 3434-3449.
[40] G. Engelhardt, D. Macdonald, Corrosion, 54 (1998) 469-479.
[41] S. Yang, D.D. Macdonald, Electrochim Acta, 52 (2007) 1871-1879.
[42] M. Urquidi‐Macdonald, D.D. Macdonald, J Electrochem Soc, 136 (1989) 961-967.
[43] C.B. Breslin, D.D. Macdonald, E. Sikora, J. Sikora, Electrochim Acta, 42 (1997) 137-144.
[44] S. Lenhart, M. Urquidi-Macdonald, D. Macdonald, Electrochim Acta, 32 (1987) 1739-1741.
[45] D. Macdonald, E. Sikora, M. Balmas, R. Alkire, Corros Sci, 38 (1996) 97-103.
[46] K. Sugimoto, S. Matsuda, Y. Ogiwara, K. Kitamura, J Electrochem Soc, 132 (1985) 1791-1795.
[47] V. Maurice, W. Yang, P. Marcus, J Electrochem Soc, 145 (1998) 909-920.
[48] D.J. Ellerbrock, D.D. Macdonald, J Electrochem Soc, 141 (1994) 2645-2649.
[49] P. Natishan, E. McCafferty, J Electrochem Soc, 136 (1989) 53-58.
[50] Y. Zhang, D.D. Macdonald, M. Urquidi-Macdonald, G.R. Engelhardt, R.B. Dooley, Corros Sci, 48 (2006) 3812-3823.
[51] D.E. Williams, J. Stewart, P.H. Balkwill, Corros Sci, 36 (1994) 1213-1235.
[52] D.E. Williams, C. Westcott, M. Fleischmann, J Electrochem Soc, 132 (1985) 1796-1804.
[53] D.E. Williams, C. Westcott, M. Fleischmann, J Electrochem Soc, 132 (1985) 1804-1811.
[54] M. Reuter, K.E. Heusler, Electrochim Acta, 35 (1990) 1809-1814.
[55] R. Fratesi, Corrosion, 41 (1985) 114-117.
[56] G. Engelhardt, D.D. Macdonald, Corros Sci, 46 (2004) 2755-2780.
[57] G. Burstein, S. Mattin, Philosophical magazine letters, 66 (1992) 127-131.
[58] P.C. Pistorius, G.T. Burstein, Philos T Roy Soc A, 341 (1992) 531-559.
[59] G. Ilevbare, G. Burstein, Corros Sci, 43 (2001) 485-513.
[60] P. Pistorius, G. Burstein, Corros Sci, 36 (1994) 525-538.
[61] G. Burstein, P. Pistorius, S. Mattin, Corros Sci, 35 (1993) 57-62.
[62] M.T. Smith, D.D. Macdonald, Corrosion, 65 (2009) 438-448.
[63] X. Guan, T. Zhu, D.D. Macdonald, Proc. CORROSION 2006, 2006.
[64] C. Liu, D. Macdonald, E. Medina, J. Villa, J. Bueno, Corrosion, 50 (1994) 687-694.
[65] T. Shibata, T Iron Steel I Jpn, 23 (1983) 785-788.
[66] Y. Zhang, M. Urquidi-Macdonald, G.R. Engelhardt, D.D. Macdonald, Electrochim Acta, 69 (2012) 12-18.
[67] S. Sharifi-Asl, F. Mao, P. Lu, B. Kursten, D.D. Macdonald, Corros Sci, (2015).

Chapter 3 Experimental

3.1 Materials

The carbon steel used in this work was cut from a CarElso 70 SOHIC slab specially designed for the Supercontainers and was provided by ArcelorMittal. The chemical composition of the steel is listed in Table 3-1. The carbon steel specimen was investigated in a typical three-electrode cell. The simulated concrete pore solution (SCPS) electrolyte was prepared by adding NaOH into a clear saturated $Ca(OH)_2$ solution, adjusting the pH upward to 13.5 at 25 °C. The final formula of the SCPS is approximately sat. $Ca(OH)_2$ + 0.428 M NaOH. All chemicals used were of analytical reagent grade. Note that precipitation of $Ca(OH)_2$ would occur during addition of NaOH into the clear sat. $Ca(OH)_2$ solution, because the extra OH^- anions introduced from NaOH shifted the equilibrium of the dissolution reaction of $Ca(OH)_2$ to the left, i.e. favoring the formation of solid phase $Ca(OH)_2$. The SCPS was kept in quiescent status until all the precipitates settled down at the bottom of the container and then the clear, upper part of the solution was then poured out of the container for all subsequent experiments. For passivity breakdown studies, where additional solutions with lower pH values were needed, sat. $Ca(OH)_2$ having a pH of about 12.4 and phosphate buffer solution with a pH of 11.5 were prepared, added with NaCl to reach different chloride ion concentrations (0.01 M, 0.1 M, 0.5 M and 1 M).

The saturated calomel reference electrode (SCE) was connected to the electrolyte by a straight Luggin probe equipped with a porous zirconia frit at the tip. The Luggin probe was filled with the same SCPS as in the cell. The tip of the Luggin probe was placed about 0.5 cm from the specimen surface, in order to avoid shielding of the surface and hence avoid locally inhomogeneous distribution in the potential and current. Concerns might exist regarding the dissolution of glass and zirconia in the highly alkaline SCPS, which releases contaminative ions into the solution. However, the author and colleagues previously carried out a long-term experiment lasting for one year using the same SCPS and glassware [1] and had observed no apparent dissolution effect. Thus, it can be assumed that the dissolution rate of the glassware and frit was negligible, leading to no contamination during the course of the present experiment (about two weeks).

The working electrode was a carbon steel cylinder with a diameter of 10 mm and a length of 15 mm, being coupled to an insulated copper wire by thread connection. The bottom of the cylinder, with an area of 0.79 cm^2, would be exposed to the solution as the test surface. For passivity studies, a stop-off lacquer (MICCROStop®) was applied on the side surface of the cylinder to prevent crevice corrosion before the specimen was cast in epoxy resin (Buehler®). For passivity breakdown experiment, the peripheral and the top area of the cylinder were masked using Kapton® polyimide film. The test surface was wet-ground to a 1200-grit finish by abrasive paper and then rinsed with deionized water and ethanol, after which the working electrode was immediately immersed into the solution. A 5 cm × 5 cm platinum gauze (99.998%) was placed facing the test surface as the counter electrode. After assembly of the experimental apparatus, as depicted in Figure 3-1, the cell contents were vigorously purged with ultra-high purity argon gas (99.999%) for two hours to expel oxygen. Deaeration was then continued throughout the entire experiment by injecting argon gas with lower flow rate into the solution to avoid contamination

by oxygen. A Gamry potentiostat and a Gamry Faraday cage were utilized in all electrochemical work.

Table 3-1: Chemical composition (wt%) of Carelso 70 SOHIC carbon steel.

C	Mn	P	S	Si	Cu	Ni	Cr	Mo	Al
0.15	0.980	0.005	0.0005	0.324	0.043	0.050	0.082	0.009	0.034
Nb	**Zr**	**V**	**Ti**	**Co**	**B**	**H***	**N**		
0.006	0.001	0.001	0.001	0.005	0.0001	1.95	0.0034		

*unit of H is ppm

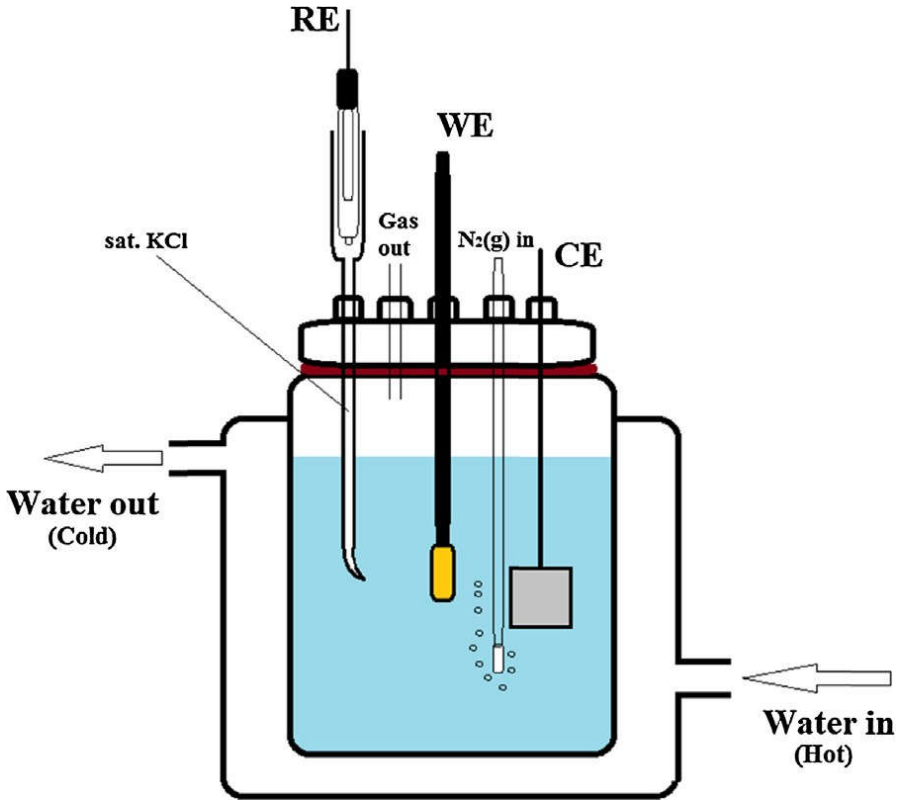

Figure 3-1: Schematic of the electrochemical cell used both in the passivity and passivity breakdown experiments.

3.2 Procedures for Passivity Studies

Prior to commencing any electrochemical experiments, a cathodic current density (-50 $\mu m/cm^2$) was applied for 5 minutes to reduce any air-formed oxide film, so that a fresh and a more reproducible initial test surface could be created. A potentiodynamic scan was performed from -1000 mV_{SHE} to +800 mV_{SHE} at a rate of 0.1667 mV/s to determine the approximate passive range of the carbon steel. Several potentials were then selected within the passive region, but close to the cathodic end as the applied potentials (from -700 mV_{SHE} to 0 mV_{SHE} with an interval of 100 mV, as reported in Chapter 4), in order to simulate the anoxic conditions that exist in the repository. After polarization, the working electrode was removed from the cell and re-polished to guarantee the freshness of the sample for ensuing tests. The solution was also replaced and again deaerated.

In the following experiments, the applied potential was initially raised step-by-step in increments of 100mV from the most negative value of the applied potential range (-700 mV_{SHE}) and then, after the highest film formation potential (0 mV_{SHE}) was reached, the process was reversed by stepping the potential in the negative direction in 100 mV decrements back to the initial applied potential, in order to examine the corrosion irreversibility of carbon steel. At each applied potential, three types of experiments were conducted consecutively:

(i) 24 hours of potentiostatic polarization to ensure the achievement of the "practical" steady-state (the "true" steady-state might take much longer times that are difficult to realize in laboratories), as indicated by the constancy of the recorded current density and demonstrated by additional tests (Chapter 4);

(ii) Electrochemical impedance spectroscopy (EIS) measurement within a frequency range between 10000 Hz and 0.01 Hz;

(iii) Mott-Schottky test that was carried out by sweeping the potential cathodically from the applied potential with a step of 25mV to -800 mV_{SHE} while simultaneously measuring the system interfacial capacitance at 5000 Hz.

After completing the Mott-Schottky measurement, the potential was stepped immediately to the next value (i.e. 100 mV more positive in the anodic potential stepping or 100 mV more negative in the cathodic potential stepping), and the three types of experiments described above were repeated. EIS data were recorded twice at each potential by scanning the frequency from the high (10000 Hz)-to-low (0.01 Hz) and then immediately in the low-to-high direction. Attempts to measure impedance down to 0.001 Hz were deterred by poor data quality at very low frequencies.

3.3 Procedures for Passivity Breakdown Studies

Passivity breakdown experiments were performed in three solutions, i.e., SCPS, sat. $Ca(OH)_2$ and phosphate buffer solution, which have different pH values of, respectively, 13.5, 12.4 and 11.5 at 25 °C, such that the effect of pH on passivity breakdown can be studied. NaCl was added to these solutions to study the effect of chloride concentration on passivity breakdown (from 0.01 M to 1 M). Experiments in all three solutions have been carried out at 25 °C. Additional tests at 55 °C and 85 °C were conducted in sat. $Ca(OH)_2$ to investigate the effect of temperature. Note that the pH of sat. $Ca(OH)_2$ will change as the temperature increases as shown in Table 3-2. After each specimen was placed in the deaerated electrolyte, cathodic polarization (-50 $\mu m/cm^2$) was applied for 5 min as an initial conditioning treatment followed by exposure at open-circuit until reaching a stable open circuit potential prior to potentiodynamic polarization. The breakdown potential of the sample was then determined potentiodynamically by sweeping the potential in the positive direction at different potential scan rates (from 0.1667 mV/s to 10 mV/s) until the measured current density increases significantly. The potentiodynamic experiments at the sweep rate of 0.1667 mV/s were typically repeated 15 times to obtain the statistical distribution of the passivity breakdown potential. All of the samples, after finishing potentiodynamic polarization, were examined under an Olympus optical microscope to make sure that the observed increase in the current density is due to the pitting corrosion, not other forms of localized corrosion attacks, such as crevice corrosion at the specimen periphery.

Table 3-2: Measured pH of sat. $Ca(OH)_2$ + NaCl as a function of temperature and chloride ion concentration.

$[Cl^-]$	pH (25 °C)	pH (55 °C)	pH (85 °C)
0.01 M	12.39	11.43	10.65
0.1 M	12.42	11.46	10.69
0.5 M	12.45	11.49	10.73
1 M	12.46	11.51	10.75

References

[1] S. Sharifi-Asl, D.D. Macdonald, A. Almarzooqi, B. Kursten, G.R. Engelhardt, J Electrochem Soc, 160 (2013) C316-C325.

Chapter 4 Experimental Results and Discussion

4.1 Potentiodynamic Scan

Figure 4-1 shows the potentiodynamic scan of carbon steel in the deaerated SCPS. The reason of starting the scan from an initial potential much lower than the open circuit potential is to reveal the complete passive region of carbon steel, considering that the passive film on iron or carbon steel is expected to form at very negative potentials in high pH solutions according to thermodynamics. A wide passive region ranging approximately from -700 mV_{SHE} up to 800 mV_{SHE} can be observed in the polarization curve, along with two minor oxidation peaks locating at around -550 mV_{SHE} (Peak I) and -350 mV_{SHE} (Peak II). The increase in current density starting at around 750 mV_{SHE} is due to the onset of oxygen evolution.

The absence of an apparent active-to-passive activation peak in the polarization curve is consistent to the finding in numerous studies [1-12] that iron becomes passive readily in alkaline solutions even at very negative potentials (e.g. ~ -800 mV_{SHE}) by forming a film primarily comprising Fe_3O_4 or $Fe(OH)_2$, determined by employing various techniques such as cyclic voltammetry, rotation-disk electrode, XPS, Raman Spectroscopy, and EIS. The film formation can also be validated by noticing that the passive region lies within potentials more anodic to the equilibrium potentials for couples of $Fe/Fe(OH)_2$ and Fe/Fe_3O_4 under the conditions of the SCPS (E_a^e and E_b^e respectively in Figure 4-1). The results in the literature cited above also demonstrated that, albeit soluble anionic ferrous complexes (e.g. $HFeO_2^-$ and FeO_2^{2-}) are the stable species in strongly alkaline solutions as dictated by thermodynamics, oxide passive films are still observed to develop readily at least in solutions with the pH lower than 14 (e.g. 1 M NaOH) at negative potentials. Formation of oxide film on iron has been reported in 5 M NaOH at about -850 mV_{SHE} [8], although the film was found to be unstable in NaOH solutions at the concentration greater than 4 M [13]. It has been indicated [13-16] that NaOH or KOH solutions as concentrated as 10 M were needed to initiate noticeable dissolution of iron in forms of $HFeO_2^-$ and FeO_2^{2-}. Peaks I and II are found to coincide well with the peaks observed in the cyclic voltammetric work on iron in alkaline solutions [1, 3-6, 12, 17, 18], which correspond to the oxidation of $Fe(OH)_2$ to Fe_3O_4 [or $Fe(OH)_2$ to FeOOH] and Fe_3O_4 to Fe_2O_3, respectively.

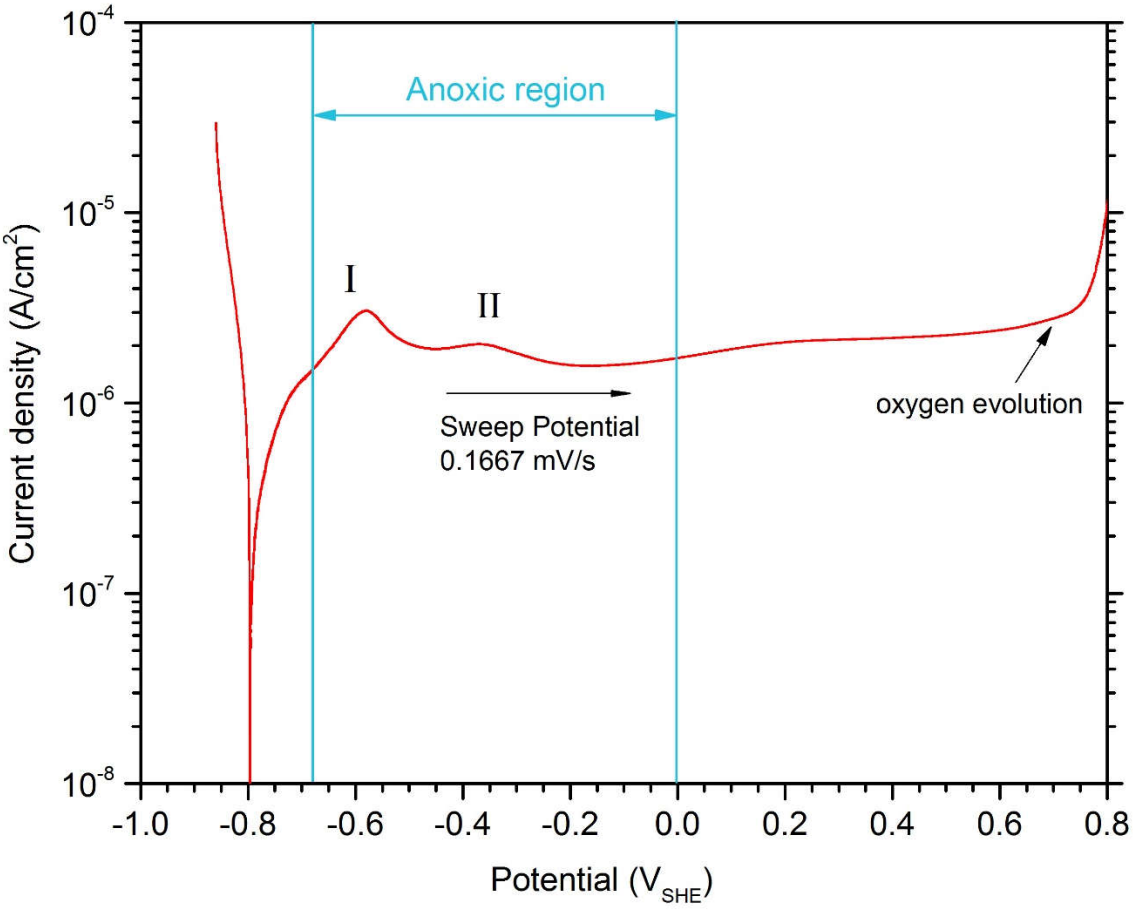

Figure 4-1: Potentiodynamic scan curves for carbon steel in the deaerated SCPS (pH = 13.5, 25°C) from -900 mV_{SHE} to +800 mV_{SHE} at a sweep rate of 0.1667 mV/s.

4.2 Potentiostatic Polarization

Based on the potentiodynamic polarization curve, eight applied potentials (from -700 mV_{SHE} to 0 mV_{SHE} in increments of 100 mV) were selected for the following potentiostatic study, which are close to the cathodic end of the passive region, in order to simulate the very negative corrosion potential of carbon steel in the repository under anoxic condition.

The steady-state current density achieved after 24-hour potentiostatic polarization at each film formation potential was observed to have a negative value at potentials cathodic to -200 mV_{SHE}. This observation has been elaborated in author's previous publication [19], which reflects the fact that, at these film formation potentials, the open circuit potential is more positive than the polarization potential and that the measured current density comprises two components, the partial anodic current density and the partial cathodic current density, with the latter dominating the former in determining the net current density. Thus, the partial cathodic reaction (i.e. hydrogen evolution by water reduction under the prevailing anoxic conditions) gives rise to a negative observed current density. However, it is important to stress that, even though the total current density is negative, the partial anodic current density cannot be ignored in analyzing the experimental data, because it is directly associated with the corrosion rate of carbon steel, which always has a finite, non-zero value for passive corrosion (i.e. passivity does not completely immunize the metal from dissolution) and has to be determined to assess the corrosion damage of the carbon steel overpack over its >100,000-year service-life.

As the potential rises, the total current density was found shifting in the positive direction, as well as becoming more stable and exhibiting fewer fluctuations. This trend can be probably ascribed to the thicker passive film generated on the metal surface at higher potentials and less perturbation brought about by the cathodic reaction (i.e. hydrogen evolution). It is also observed that the system, in response to the cathodic potential stepping, achieves the "practical" steady-state more rapidly, compared with the anodic stepping, during the potentiostatic polarization and is characterized by polarization curves that show much smaller fluctuations, which is an exemplary indication of the persistence of the barrier layer upon cathodic reduction.

4.3 Potentiostatic EIS

EIS is well established as a powerful *in situ* technique for studying electrochemical and corrosion systems [20, 21]. Impedance is a complex number that describes the current response of a system to the applied voltage perturbation, which is very small in magnitude (~10 mV) and usually in sinusoidal form. EIS measures the impedance of a system over a wide range of frequencies, accessing information of various processes (i.e. with different characteristic relaxation times) occurring within the system. It was applied in the present work to investigate the nature of the processes that occur at the carbon steel/passive film/solution interfaces in the SCPS environments.

4.3.1 Validity of Impedance Data

It has been articulated [22] that, in order to interpret a physico-electrochemical system in terms of linear models (*i.e.*, models that are described by linear differential equations), such as the PDM and the Mixed Potential Model (detailed in Chapter 5), the impedance of the system has to satisfy four general conditions: causality, stability, linearly, and finiteness. While the rate expressions in electrochemical models, in general, and in the PDM, in particular, are exponential functions in voltage and film thickness, they are readily linearized by exponential expansion and in the limit of small perturbations, retaining only the linear terms.

Since the stability of the electrochemical system during the EIS measurements is critical to obtaining viable data for further analysis and model optimization, the quality of the EIS data was checked both experimentally and theoretically, with the latter being performed using the Kramers-Kronig transforms. The data were checked experimentally by scanning the frequency from high-to-low and then immediately back from low-to-high, with the impedance being measured at ten frequencies within each decade of each scan, to ascertain that the same values were obtained at equivalent frequencies in the two directions. If the system is in the steady state, which means that the thickness and current density are independent of time, the impedance data should match in the two frequencies scan directions. Figure 4-2 shows the impedance spectra of these two opposite frequency scans in Bode planes obtained at 0 mV_{SHE} and -600 mV_{SHE} in the anodic potential stepping after 24-hour polarization. Very good agreement between the results from the opposite scans is observed at both potentials, which demonstrates the establishment of an "operational" steady state as well as demonstrating the stability of the system. It should be noted that the potential had to be held constant for a sufficient time that the bi-layer passive film had become stable, thereby ensuring reproducibility of the data. Notwithstanding the observation that the recorded current density at higher film formation potentials became invariant with only very small fluctuations (order of 1 nA/cm^2) after a couple hours, extension to more than 12 hours was found to be necessary in order that the high-to-low and low-to-high impedance data to become fairly coincident for all film formation potentials, and an even longer 24-hour of potentiostatic polarization was selected to further consolidate the steady-state.

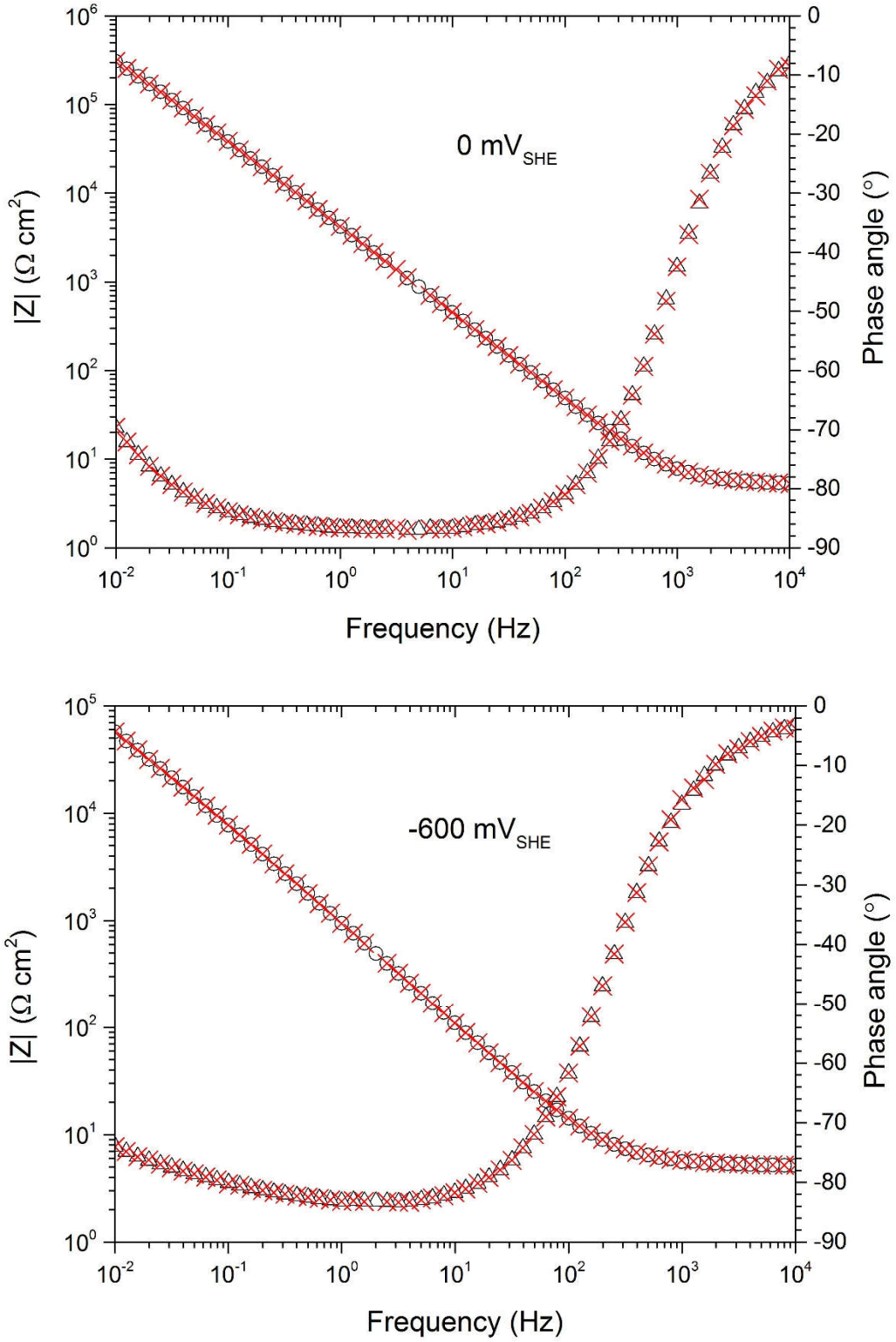

Figure 4-2: EIS spectra measured on carbon steel after being polarized at 0 mV_{SHE} and -600 mV_{SHE} in the anodic potential stepping for 24 hours in the N_2-deaerated SCPS, including both high-to-low (black open circles) and low-to-high (red crosses) frequency scans.

Kramers-Kronig (K-K) transformation is adopted here to theoretically confirm the compliance of the system under investigation with linear system theory. K-K transformation calculates the real part from the imaginary part (or vice versa) of the response function (i.e. impedance in the application of EIS) based on the interrelationship between analyticity and causality. Because of its purely mathematical origin from the definition of causality (via Cauchy's theorem), and because it does not assume any physical properties of the system, it is an ideal tool for examining data that originate from experiments under various circumstances that may result in violation of the constraints of linear systems. The software contained in Gamry Echem Analyst was used to conduct K-K transformations and to compute the fractional residual errors of the transformed data. Figure 4-3 exhibits the transformation result of the impedance data obtained at -200 mV_{SHE} and -400 mV_{SHE}, where the real and imaginary components calculated by K-K transformation are compared with experimental components. Again, good agreement between the experimental and transformed data exists within the entire frequency range. It should be noted that, although the residual errors of K-K transforms are observed to always spike up at frequencies larger than 500 Hz (Figure 4-4), those enhanced errors are still very small (< 0.4%) and, for the majority of the frequencies, the errors fall within an even more confined range of 0.1%, thereby verifying the causality, stability, and the linearity of the system. The origin for the increased residual errors at high frequencies has yet to be determined decisively. Those data points with errors that are clearly beyond the normal range of errors were rejected in the subsequent optimization process to ensure the precision of the optimization results.

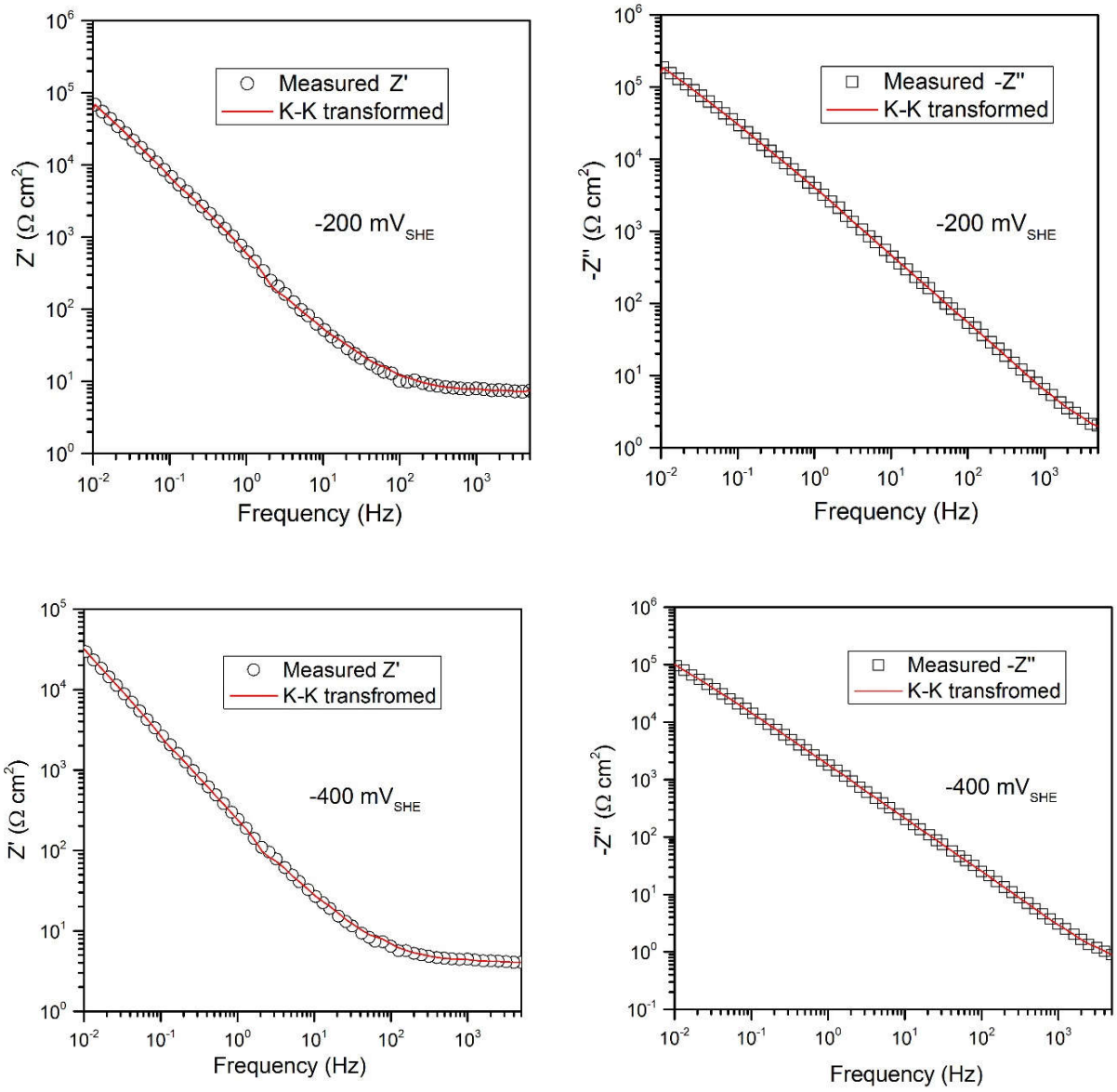

Figure 4-3: Kramers-Kronig transforms of the real and imaginary components of the impedance data for carbon steel in the deaerated SCPS (pH = 13.5, 25◦C) measured at −200 mV_{SHE} (upper) and -400 mV_{SHE} (lower) during the anodic potential stepping.

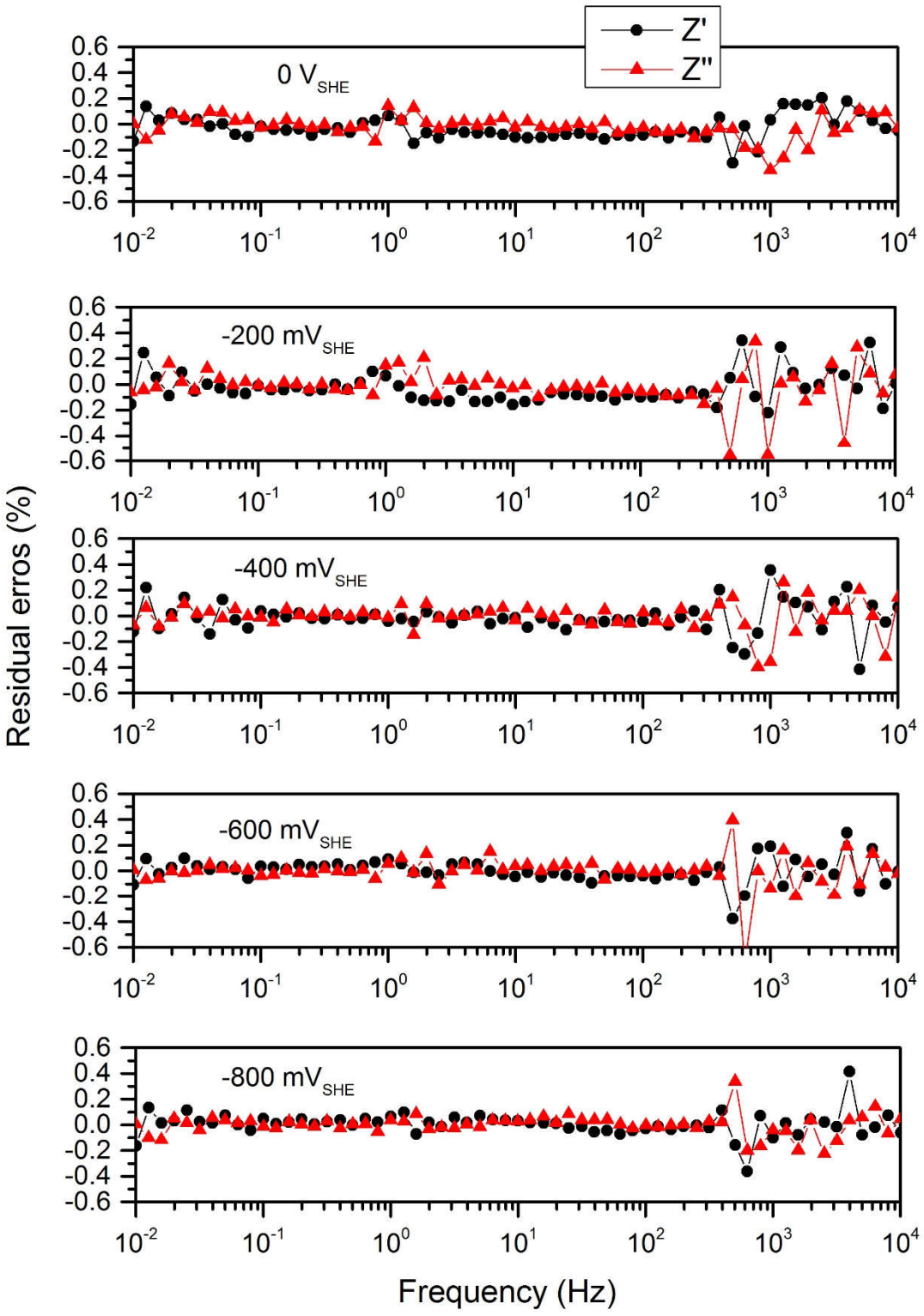

Figure 4-4: Residual errors of Kramers-Kronig transforms of the real and imaginary components of the EIS results for carbon steel in the N_2-deaerated SCPS measured at different potentials during the anodic potential stepping.

4.3.2 The EIS Results

The EIS results for all applied potentials in both anodic and cathodic potential stepping are presented in Nyquist and Bode planes in Figure 4-5 to Figure 4-8. Only the high-to-low frequency scan results are included in the figures for the sake of clarity. It is discovered from the overlaid EIS results that, within the entire potential range, there is a clearly-defined trending in the impedance spectra as the potential is stepped in the anodic or cathodic direction. For the case of the anodic potential stepping, as shown in the Bode plot in Figure 4-6, the modulus of the impedance of the film gradually increases within the entire frequency range as the potential was stepped anodically from -700 mV_{SHE}, which is a result of the continuous thickening of the barrier layer and the development of the bi-layer structure in the film. The phase angle vs. frequency curves for these potentials have very similar shapes and are just slightly shifted in position, progressively toward more negative phase angles as the potential shifts. In the Nyquist plot (Figure 4-5), the $-Z''$ vs. Z' curves are observed to extend in length with both $-Z''$ and Z' values increasing as the potential is raised from -700 mV_{SHE}, a reflection of the increasing modulus of impedance, too. Likewise, film dissolution causes a decrease in the modulus of the impedance when the potential declines from 0 mV_{SHE} (Figure 4-8).

The phase angles of the impedance at higher potentials are found generally larger more negative than those at lower potentials. This tendency indicates that the semiconducting passive film behaves progressively toward being a pure capacitor (phase angle equals to -90°) when the film formation potential is more positive. Additional capacitance character of the film is generally acknowledged to have an effect of improving the protective capability, as defined by the value of passive current density, of the barrier layer due to the greater transfer resistance that hinders species transportation across the film. Thus, the more negative phase angle suggests that the film becomes more protective of the carbon steel substrate at higher potentials.

Figure 4-9 to Figure 4-11 错误!未找到引用源。 display the comparison of the impedance spectra at equivalent applied potentials of -100 mV_{SHE}, -300 mV_{SHE}, and -700 mV_{SHE}, but obtained in the opposite potential stepping directions. At each potential, the passive film formed during the cathodic potential stepping has a larger imaginary component in the impedance. Compared with the real component, where only a slight difference appears between the results from the two potential stepping directions, the difference in the imaginary component within the entire frequency range is more noteworthy, especially at low frequencies. The larger imaginary component indicates an enhanced capacitance character of the film, and hence the film existing on carbon steel during the cathodic stepping is more protective than that during the anodic stepping at equivalent potentials.

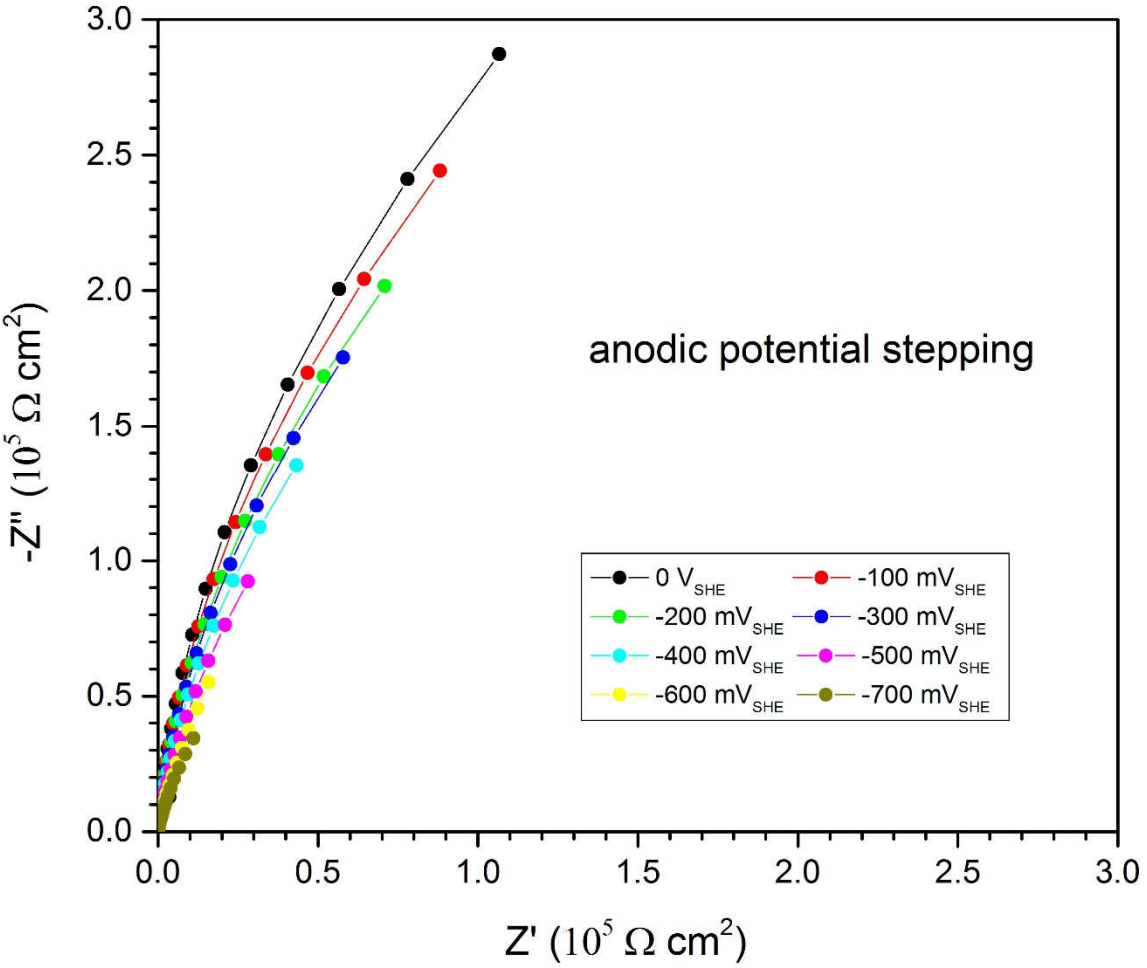

Figure 4-5: Nyquist diagram of the EIS results for carbon steel polarized at different film formation potentials after 24 hours in the deaerated SCPS. The applied potential was stepped from -700 mV_{SHE} in the anodic direction up to 0 V_{SHE}.

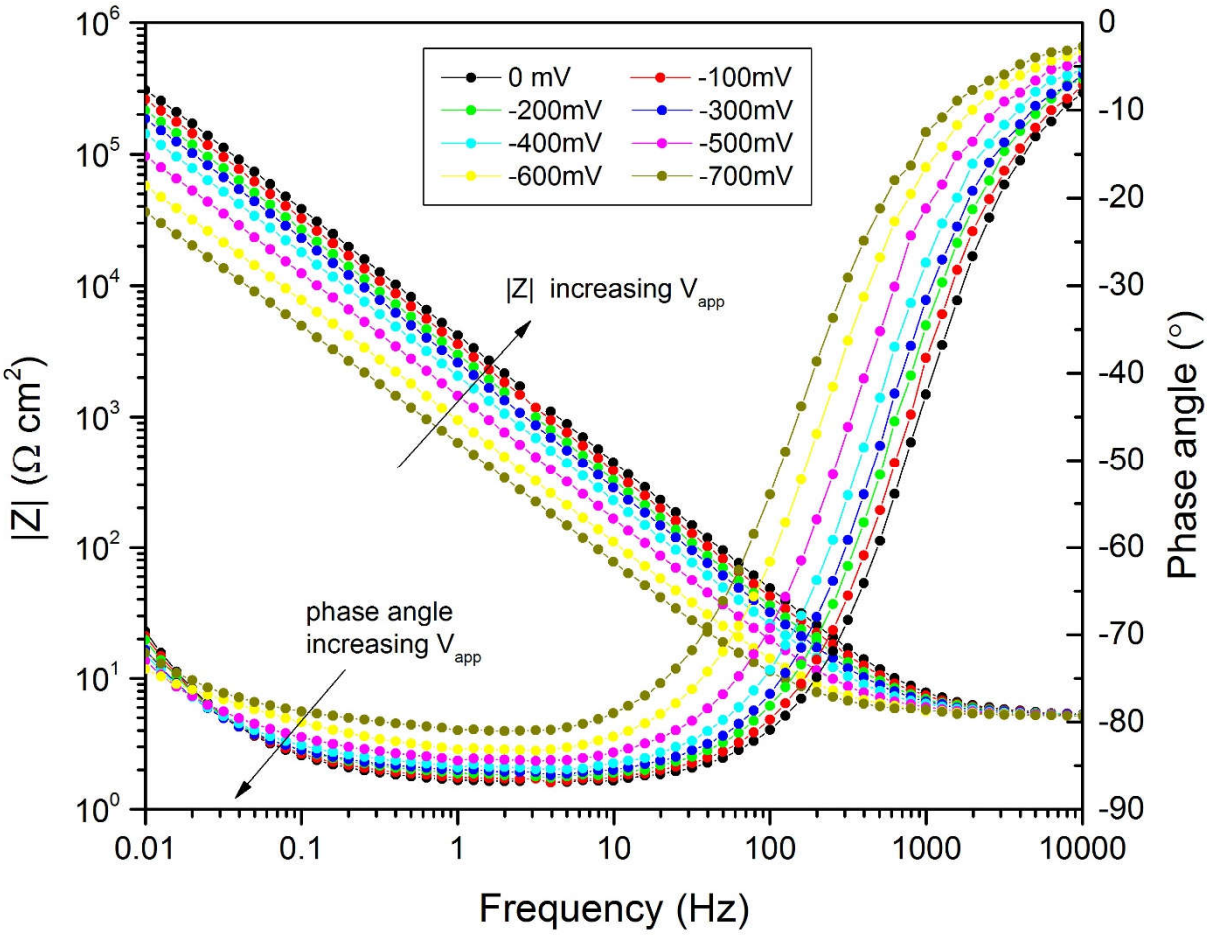

Figure 4-6: Bode diagram of the EIS results for carbon steel polarized at different film formation potentials after 24 hours in the deaerated SCPS. The applied potential was stepped from -700 mV_{SHE} in the anodic direction up to 0 V_{SHE}.

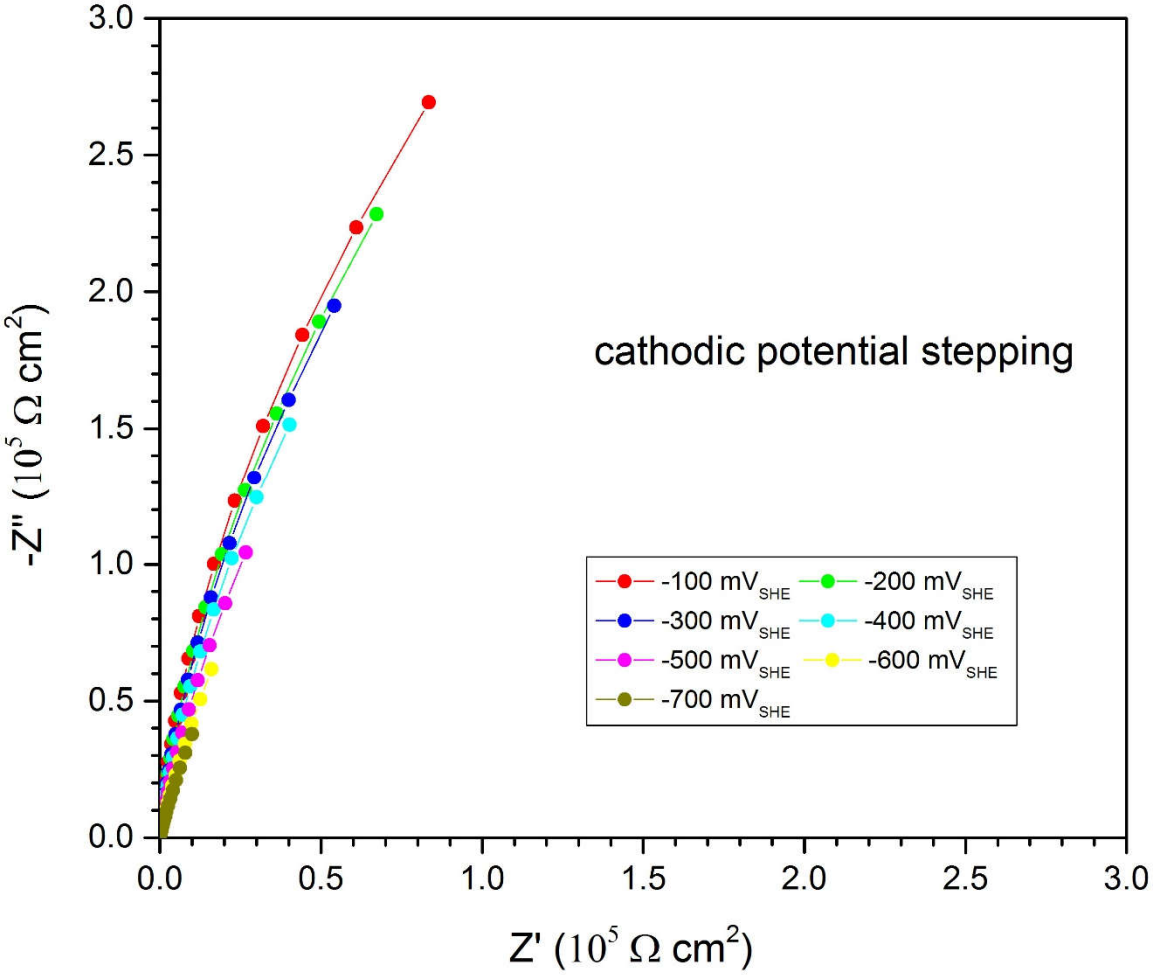

Figure 4-7: EIS spectra for carbon steel polarized at different film formation potentials after 24 hours in the deaerated SCPS. The applied potential was stepped from 0 V_{SHE} in the cathodic direction down to -700 mV_{SHE}.

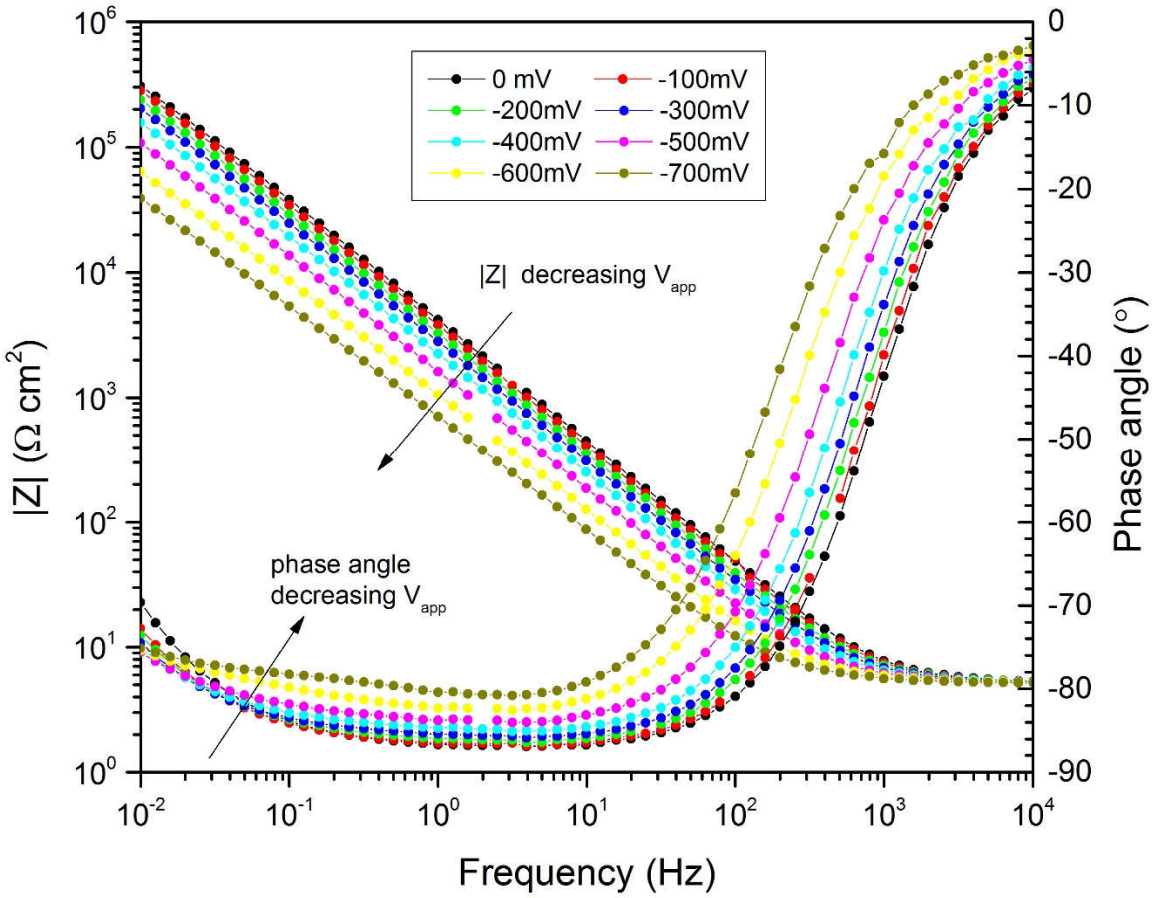

Figure 4-8: Bode diagram of the EIS results for carbon steel polarized at different film formation potentials after 24 hours in the deaerated SCPS. The applied potential was stepped from 0 V_{SHE} in the cathodic direction down to -700 mV_{SHE}.

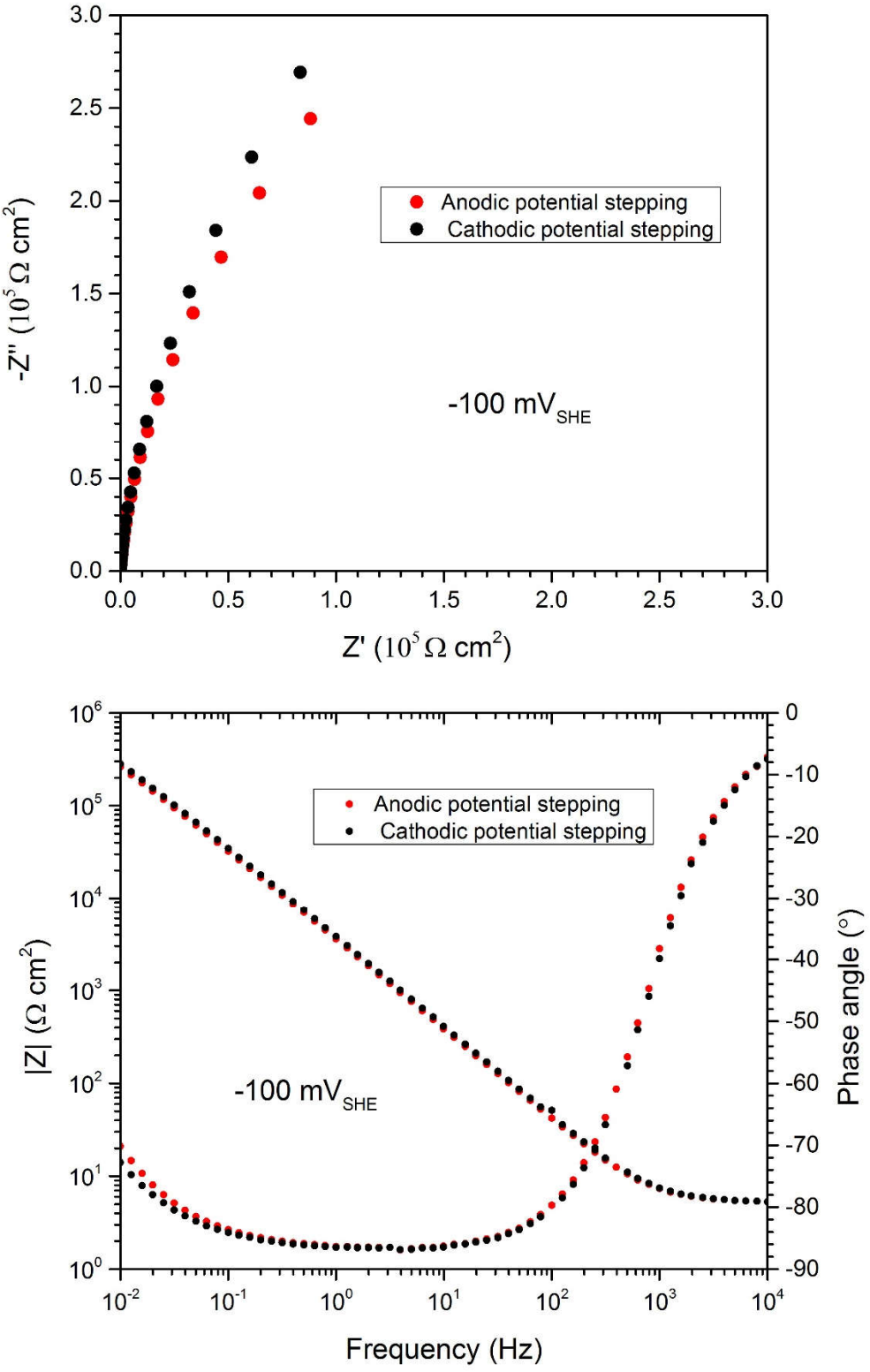

Figure 4-9: Comparison of the EIS results for carbon steel in the N_2-deareated SCPS obtained from the opposite potential stepping directions at −100 mV_{SHE}.

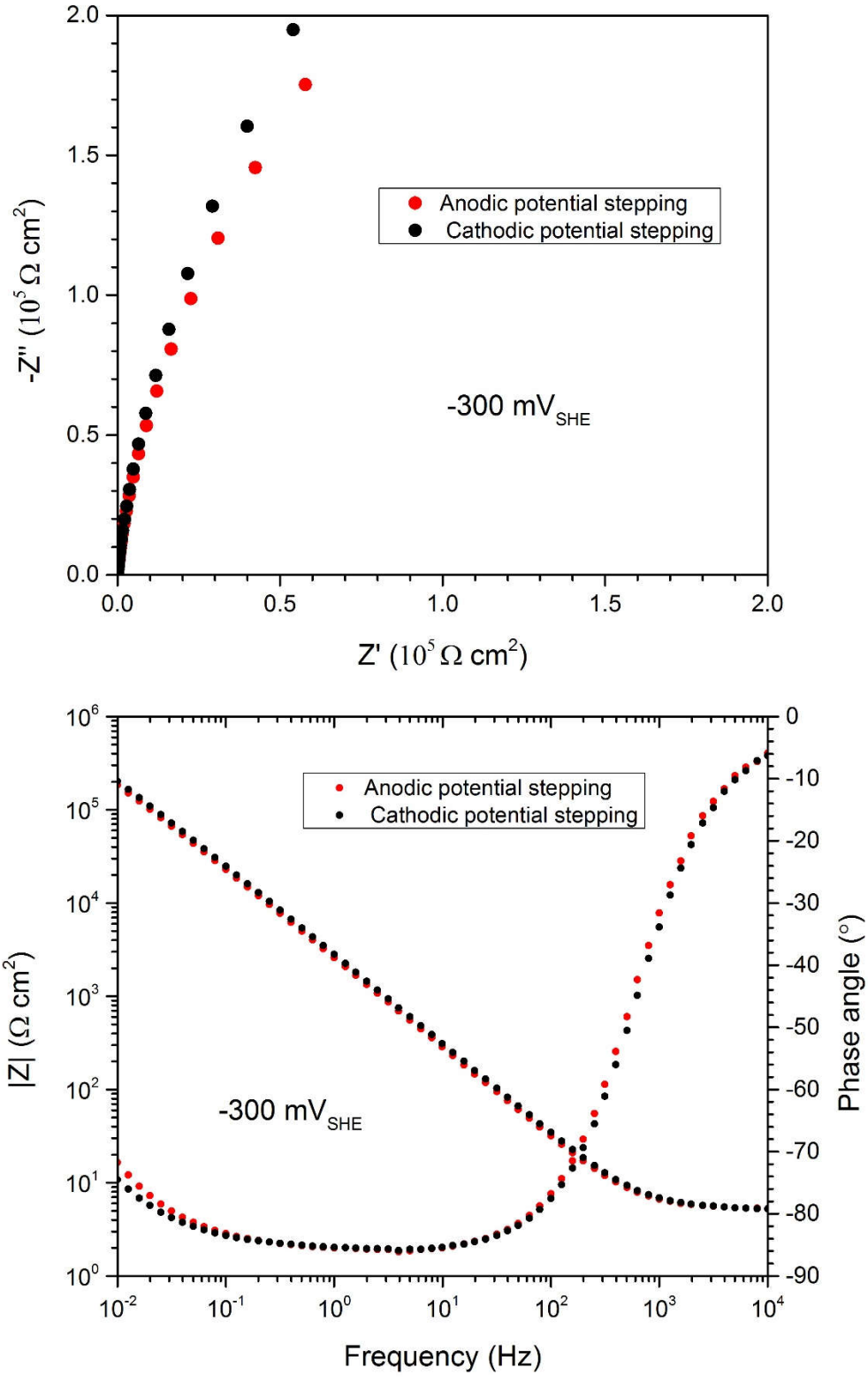

Figure 4-10: Comparison of the EIS results for carbon steel in the N_2-deareated SCPS obtained from the opposite potential stepping directions at −300 mV_{SHE}.

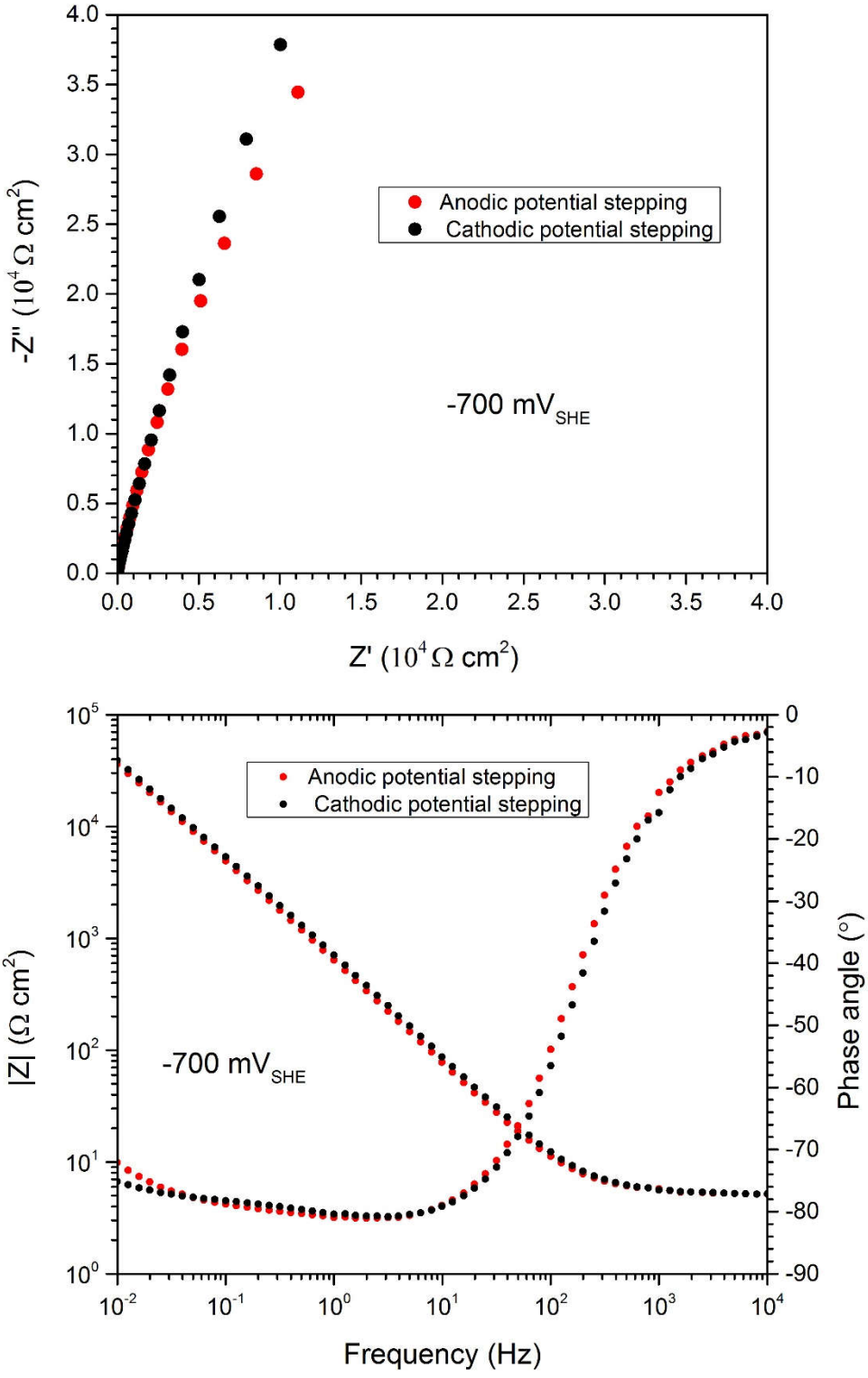

Figure 4-11: Comparison of the EIS results for carbon steel in the N_2-deareated SCPS obtained from the opposite potential stepping directions at −700 mV_{SHE}.

4.4 Qualitative Mott-Schottky Analysis

The Mott-Schottky (M-S) analysis was performed in order to estimate the dopant density and the general defect structure in the passive film on carbon steel at different film formation potentials. In light of the many issues in applying classical M-S theory to passive films that are usually very thin and highly disordered (e.g. comparable dimension of the depletion region and the film thickness, degeneration of the film, potential and frequency dependence of the dopant density, limited linear region, et al. [23-25]), it is difficult to justify unequivocally the quantitative accuracy of the data of M-S tests. Thus, the M-S analysis was only used qualitatively and semi-quantitatively in this study to examine, in a general manner, how the point-defect structure of the film changes with film formation potential and what kind of effect the opposite potential stepping directions have on the change in dopant density.

The basic M-S equation is written as:

$$\frac{1}{C_{sc}^2} = \frac{\pm 2}{\varepsilon_f \varepsilon_0 e N}\left(V_{app} - V_{fb} - \frac{kT}{e}\right) \tag{4-1}$$

where the positive sign is for n-type semiconductors and negative sign is for p-type semiconductors. C_{sc} is the space charge capacitance, ε_f is the dielectric constant of the passive film ($\varepsilon_f = 30$ is assumed), $\varepsilon_0$is the vacuum permittivity, e is the electronic charge, N is the dopant density, V_{app} is the applied potential, V_{fb} is the flat-band potential of the film, k is Boltzmann's constant, and the term kT/e equals approximately 25.6 mV at ambient temperature. If C_{sc}^{-2} is plotted versus V_{app}, a slope of $\pm 2/(\varepsilon_f \varepsilon_0 e N)$ can be expected, and from the magnitude of the slope the dopant density may be obtained, while the sign of the slope identifies the electronic type of the semi-conductor film.

C^{-2} vs. V profiles have been constructed for each film formation potential that is positive to -500 mV_{SHE} (including -500 mV_{SHE}), as shown in Figure 4-12, by sweeping the potential quickly in the negative direction from the film formation potential to -800 mV_{SHE}, after completing the EIS measurement at that film formation potential. The imaginary component of the impedance, Z'', was measured at a frequency of 1000 Hz as the potential was swept cathodically at a step of 25 mV. Such means was adopted to "freeze-in" the crystallographic defect structure and to accomplish the measurement before the barrier layer had a chance to change; these constraints rendering the passive film more akin to a classical, abrupt junction diode as used in the original derivation of M-S relationship, and hence improving the quality of the data, to some extent, as further discussed later.

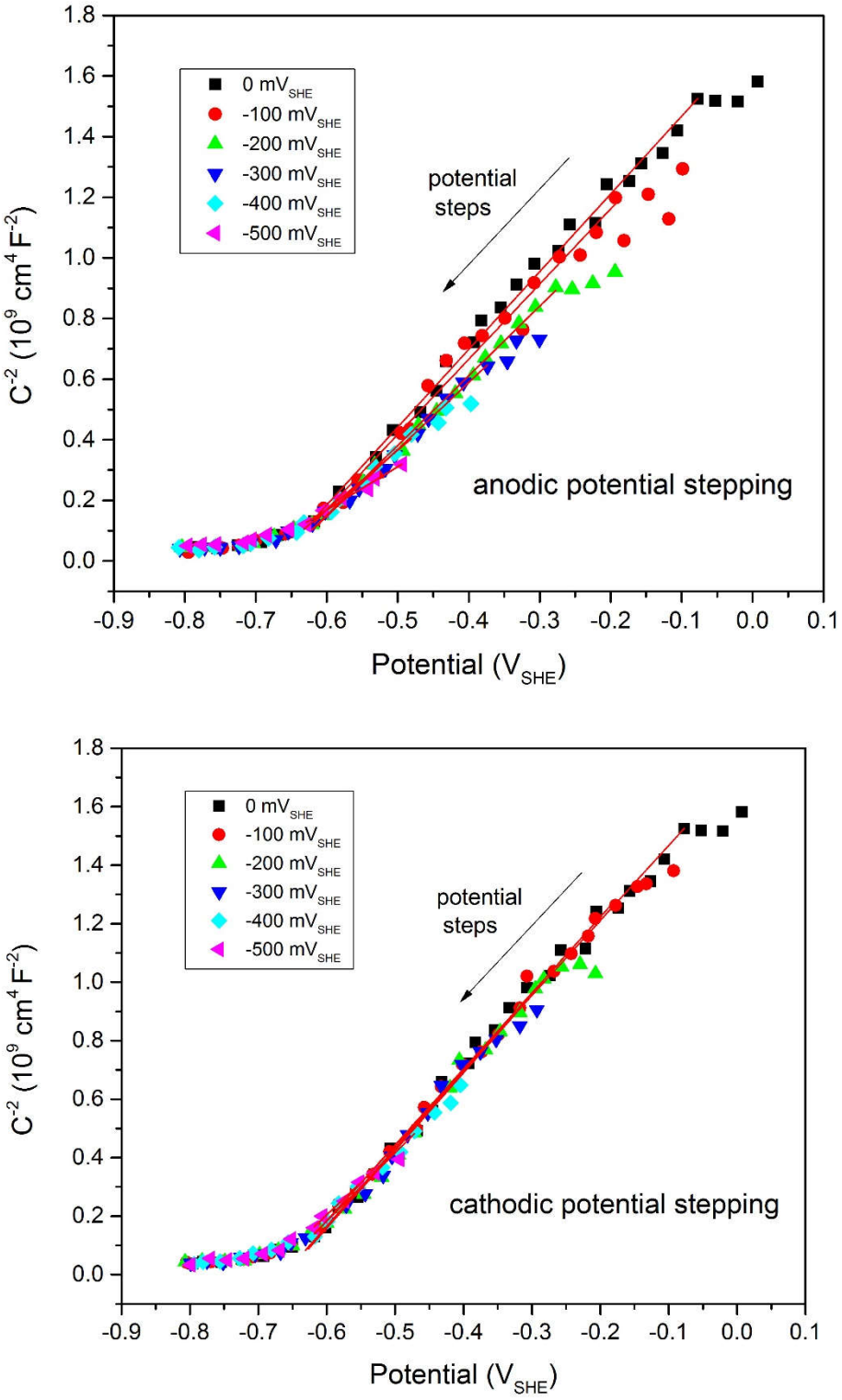

Figure 4-12: Mott-Schottky plots of the passive film on carbon steel in the deaerated SCPS obtained by stepping potential from each film formation in the negative direction to −800 mV_{SHE} with a step of 25 mV and a measuring frequency of 5000 HZ during the anodic potential stepping (upper) and the cathodic potential stepping (lower). Red straight lines are the linear fitting results of the linear region in the C^{-2} vs. V curves.

The approach implemented of sweeping the potential in the negative direction while simultaneously measuring the capacitance was designed to address the concern that measuring the capacitance at a series of potentials away from the film formation potential under quasi steady-state conditions may change the dimension of the passive film, which would result in the experiment not being in good confluence with M-S theory. This is because M-S theory assumes that: (i) the dimension of the coordinate perpendicular to the junction is infinite; (ii) the film thickness is much larger than the width of the depletion region; (iii) the dopant (defect) concentration is independent of voltage, and (iv) the dopant concentration is sufficiently small that the junction is not degenerate (that is, the Fermi level moves above the conduction band edge for n-type doping or moves below the valence band edge for p-type doping). It is doubtful that any of these condition is ever satisfied in M-S analysis, where the capacitance is measured at each voltage after steady-state is achieved, because simple calculation shows that, for the high dopant levels present in passive films ($10^{20} \sim 10^{22}$ cm^{-3}): (i) the system should be degenerated; (ii) the thickness of the depletion region and the thickness of the film are of the same order; and (iii) the PDM predicts that the defect concentration in the steady-state is a function of voltage. Based on the experimental observations reported in this dissertation and other work, the lowering of the applied voltage does not cause obvious dissolution of the passive film on carbon steel, at least not significantly within the short time at each voltage. Accordingly, sweeping the potential cathodically from film formation value at a sufficiently fast sweep rate, as adopted here, is able to minimize any change in passive film thickness during the measurement and results in the dopant (defect) concentration being "frozen-in" and hence being independent of voltage, thereby ensuring that the recorded C^{-2} vs. V profile reflects the theoretical basis of the Mott-Schottky relationship.

The positive slopes of C^{-2} vs. V curves are consistent with the finding that passive film on carbon steel is an n-type semiconductor [26-29], due to the presence of electronic donors that are possibly oxygen vacancies and/or iron interstitials. Which of these two types of defect is the dominant donor species in the passive film on carbon steel will be examined later by PDM optimization.

It can be seen in Figure 4-12 that a fairly good linearity can be observed in all the curves at potentials more positive to -600 mV_{SHE}, which is consistent to the finding of several previous studies [25-27, 29], although non-linearity of M-S plots were reported in some other work [30-33], which has been propounded to result from various reasons such as formation of inversion layer, surface states [29], existence of second donor level within the band gap [24, 32], and distribution of donor states [31]. A slight "bent-down" deviation from linearity does exist at the most positive potentials in the M-S curves shown in Figure 4-12. However, because this deviation occurs in all the curves disregarding at what potential the film was formed, it is unlikely to result from surface states or intra-band donor levels, which will render the curves non-linear at certain potentials that corresponds to the specific energy levels. Also, the film formation potentials in this work were too negative to yield an inversion layer in the band structure of the barrier layer. In light of the observation that the deviation is always confined within the most positive potentials in an M-S curve, coinciding with the first couple of potentials at which the capacitance was measured after each M-S experiment commenced, the deviation is believed to be caused by the charging of the interfacial capacitance during the initial stage of the experiment. In order to make the subsequent analysis on the C^{-2} vs. V curves self-consistent, the linear region for each curve is defined as the potential range between -600 mV_{SHE} and the fourth most positive potential within a measurement (i.e. to exclude "bent-down" part).

The single slope of the linear region in both ascending and descending potential stepping directions suggests that a single donor level was uniformly distributing in the passive film at each film formation potential during the experiment. It should be pointed out that the measured impedance of the passive film has been observed to vary with frequency [20, 25] and thus the frequency dispersion has to be taken into account so as to obtain the exact value for the capacitance of the passive film, a topic that has been elaborated in Ref. [34, 35]. In order to examine the effect of such frequency dispersion on the M-S results obtained in our specific system, M-S experiments employing a wide range of frequencies (10^{-1} Hz to 10^{4} Hz) has been carried out in the steady state at film formation potential of 0 V_{SHE}. The resulting M-S profiles are shown in Figure 4-13 and the corresponding donor densities and flat-band potentials calculated from the slopes and intercepts of the linear regions of the curves are plotted in Figure 4-15 as a function of frequency. Note that the linear region gradually narrows as the applied frequency decreases. It can be observed that both N_d and V_{fb} decrease (more negative for V_{fb}) with the logarithm of frequency and, more importantly, the frequency dispersion seemingly exerts fairly small impact on the donor density in the film formed on carbon steel in the SCPS. The value of N_d varies only by a factor of about 4 over a broad five-order-of-magnitude frequency rang. Combining this observation with the circumstance that the detailed electronic properties of the film are of less concern in terms of the objective and scope of the present project, the effect of frequency dispersion was not incorporated into the analysis of M-S results in this work.

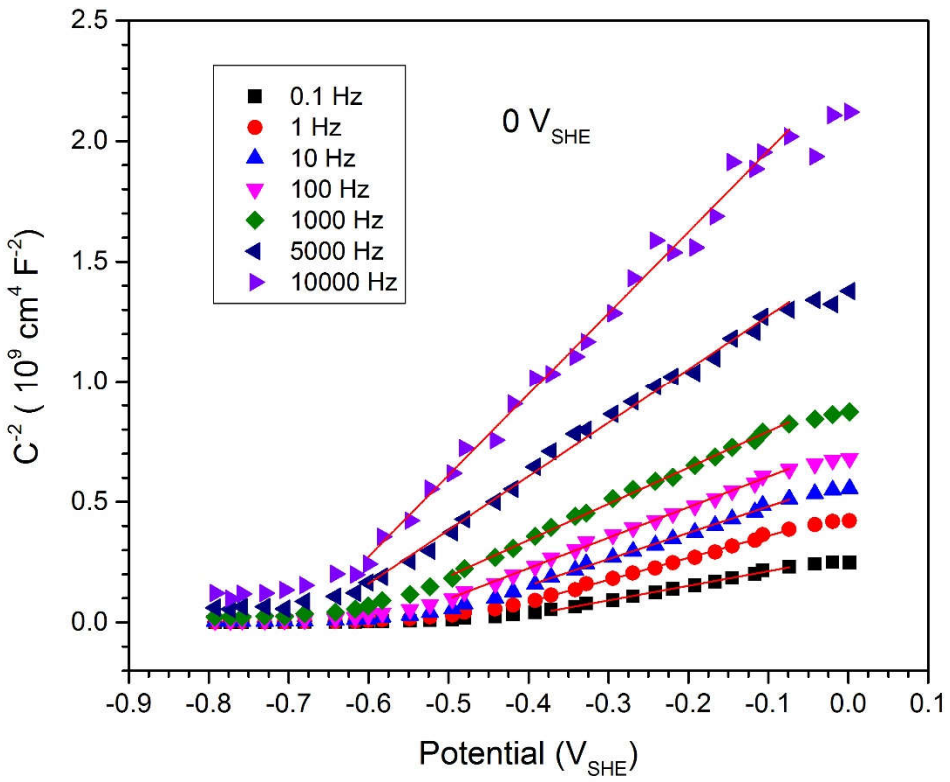

Figure 4-13: Effect of the adopted frequency on the Mott-Schottky profiles measured at 0 V_{SHE}. Three hours of potentiostatic polarization at 0 V_{SHE} were carried out after each measurement to re-establish the steady state of the passive system.

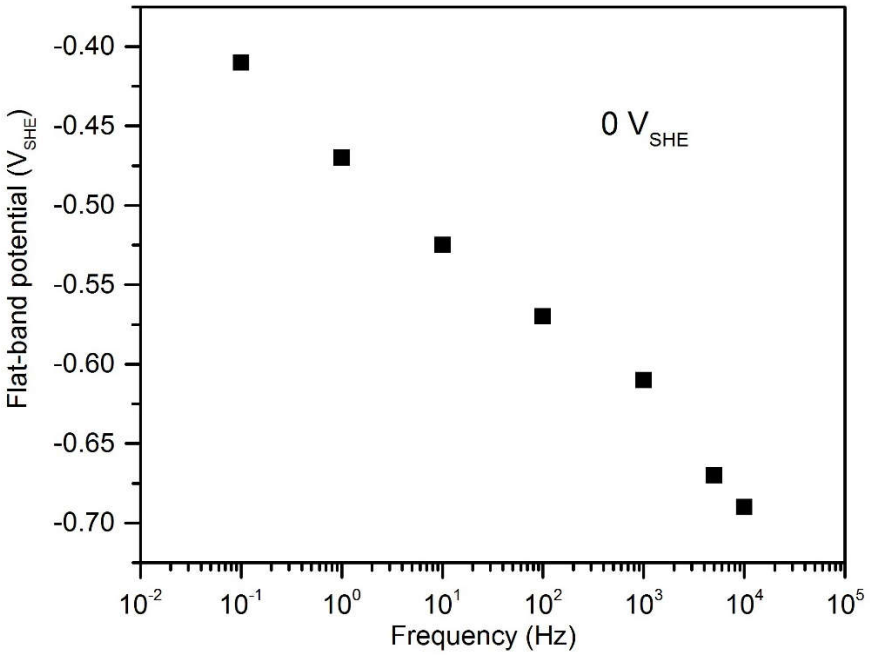

Figure 4-14: Effect of frequency on the flat-band potential calculated from the intercepts of the measured Mott-Schottky profiles at 0 V_{SHE}.

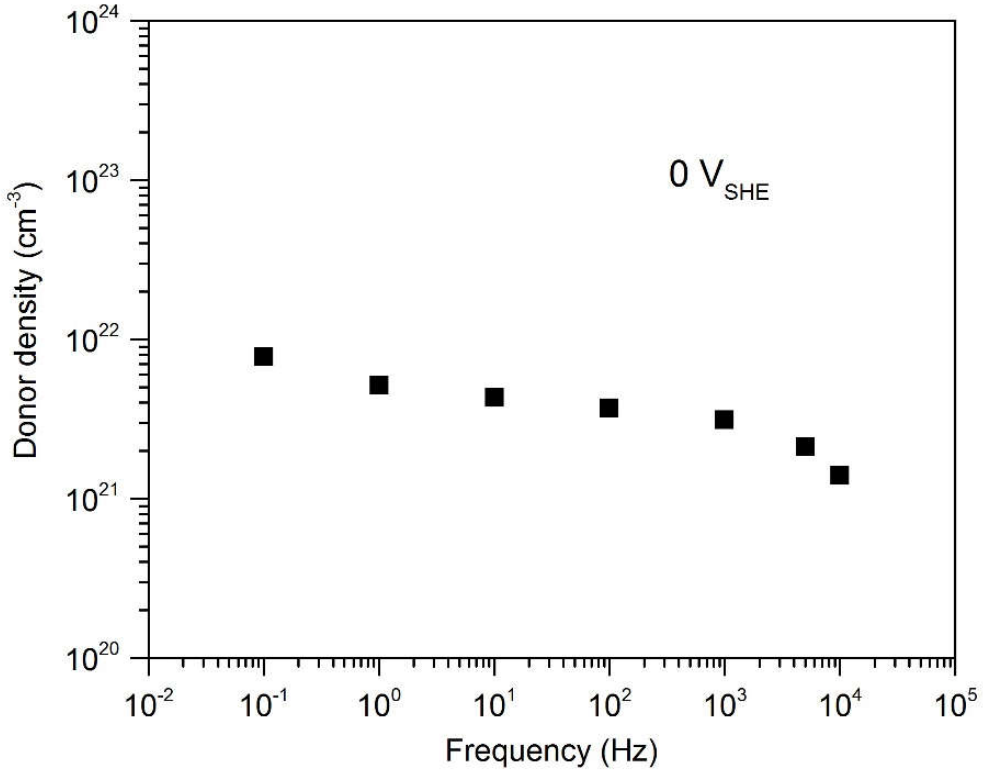

Figure 4-15: Effect of frequency on the donor density calculated from the slopes of the measured Mott-Schottky profiles at 0 V_{SHE}.

The donor density, $N_{d,}$ at each steady-state potential has been calculated from the slopes of the linear region in C^{-2} vs. V profiles and is plotted versus the film formation potential in Figure 4-16. Despite the equivocality in the results of N_d as detailed above, it is evident that N_d exhibits the trending of declining markedly as the potential is raised but remaining almost constant (scattering around 1.86×10^{21} cm^3) after the potential stepping is reversed. The decrease in donor concentration with ennobling voltage has been observed in multiple studies [29, 36-38], a phenomenon may be attributed to the thickening of the passive film which allows atoms and point defects ampler space to arrange themselves and assume a more stable structure with reduced extent of defects or imperfection [25, 29]. The decreasing N_d from the anodic potential stepping can be successfully fitted in an exponential form as demonstrated by the PDM in Ref. [38]:

$$N_d = [0.015\exp(-0.907) + 1.88]\times10^{21}\ \text{cm}^3 \tag{4-2}$$

The constancy of N_d at descending potentials is consistent with the PDM, too, which postulates that the defect generation reactions at m/bl interface are irreversible [39, 40]. Since the diffusivities of the defects are inherently very low ($\sim10^{-16}$ cm^2/s, see later in Section 6.5), the defects structure becomes "locked-in" when formed on positive stepping of the potential, but, upon negative stepping, the defects are not annihilated effectively, because the interfacial reactions occurring between metal and barrier layer are inherently irreversible. In addition, the film thins only by dissolution at the bl/ol interface (Reaction 7 in Figure 2-2), a process that does not involve the defects. Accordingly, the donor density tends to be a constant at the last value on forward potential stepping, which is exactly what is observed here. Based on this finding, it is further postulated that the kinetic irreversibility of the passive state is tightly associated with the discrepancy in the defect structure of the passive film upon opposite potential excursion directions.

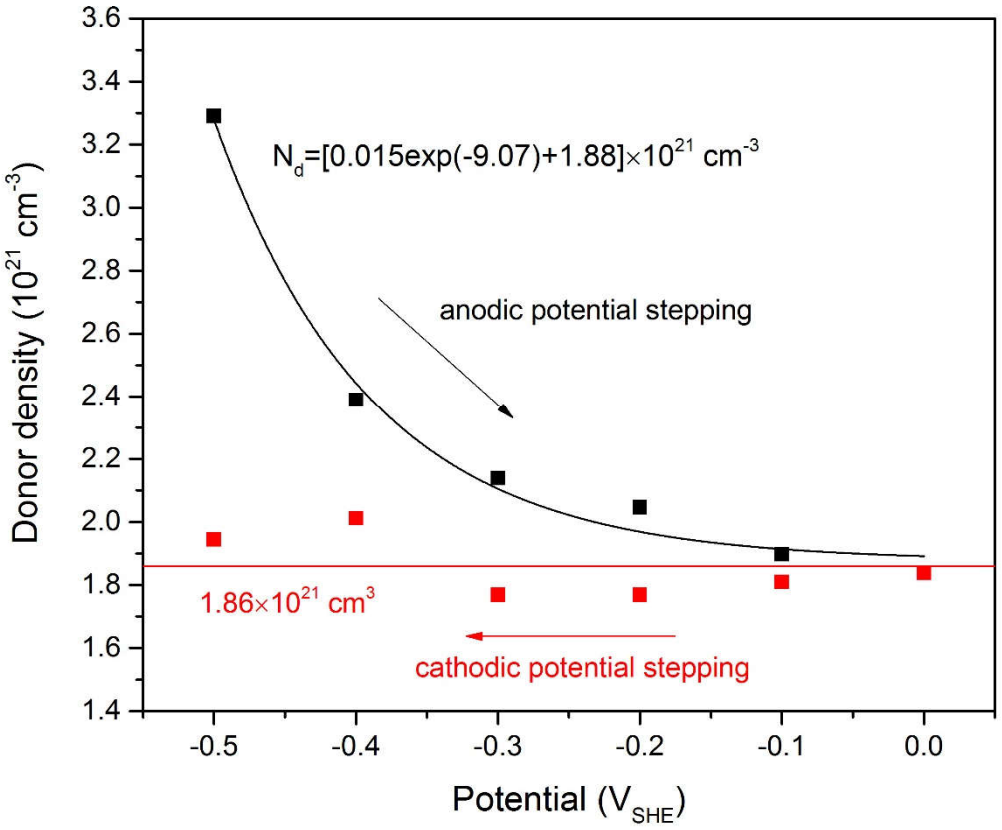

Figure 4-16: Donor density within the passive film on carbon steel in the N_2 deaerated SCPS estimated from Mott-Schottky analysis versus the film formation potential for both the anodic and the cathodic potential stepping.

References

[1] S. Haupt, H. Strehblow, Langmuir, 3 (1987) 873-885.
[2] D. Thierry, D. Persson, C. Leygraf, N. Boucherit, A. Hugot-Le Goff, Corros Sci, 32 (1991) 273-284.
[3] P. Schmuki, M. Büchler, S. Virtanen, H. Isaacs, M. Ryan, H. Böhni, J Electrochem Soc, 146 (1999) 2097-2102.
[4] L. Freire, X.R. Novoa, M.F. Montemor, M.J. Carmezim, Mater Chem Phys, 114 (2009) 962-972.
[5] S. Joiret, M. Keddam, X.R. Novoa, M.C. Perez, C. Rangel, H. Takenouti, Cement Concrete Comp, 24 (2002) 7-15.
[6] A. Hugot‐Le Goff, J. Flis, N. Boucherit, S. Joiret, J. Wilinski, J Electrochem Soc, 137 (1990) 2684-2690.
[7] P. Ghods, O.B. Isgor, J.R. Brown, F. Bensebaa, D. Kingston, Appl Surf Sci, 257 (2011) 4669-4677.
[8] H. Zhang, S.M. Park, J Electrochem Soc, 141 (1994) 718-724.
[9] G. Bignold, Corros Sci, 12 (1972) 145-154.
[10] L. Veleva, M.A. Alpuche-Aviles, M.K. Graves-Brook, D.O. Wipf, J Electroanal Chem, 537 (2002) 85-93.
[11] M. Valcarce, M. Vázquez, Electrochim Acta, 53 (2008) 5007-5015.
[12] A. Wieckowski, E. Ghali, Electrochim Acta, 30 (1985) 1423-1431.
[13] J.-Y. Zou, D.-T. Chin, Electrochim Acta, 33 (1988) 477-485.
[14] K. Bouzek, I. Roušar, H. Bergmann, K. Hertwig, J Electroanal Chem, 425 (1997) 125-137.
[15] R. Armstrong, I. Baurhoo, Journal of Electroanalytical Chemistry and Interfacial Electrochemistry, 40 (1972) 325-338.
[16] R. Armstrong, I. Baurhoo, Journal of Electroanalytical Chemistry and Interfacial Electrochemistry, 34 (1972) 41-46.
[17] D.D. Macdonald, D. Owen, J Electrochem Soc, 120 (1973) 317-324.
[18] R.S. Guzman, J. Vilche, A. Arvia, Electrochim Acta, 24 (1979) 395-403.
[19] P. Lu, B. Kursten, D.D. Macdonald, Electrochim Acta, 143 (2014) 312-323.
[20] B.D. Cahan, C.T. Chen, J Electrochem Soc, 129 (1982) 474-480.
[21] D.D. Macdonald, Electrochim Acta, 35 (1990) 1509-1525.
[22] D.D. Macdonald, M. Urquidimacdonald, J Electrochem Soc, 132 (1985) 2316-2319.
[23] A. Goossens, M. Vazquez, D.D. Macdonald, Electrochim Acta, 41 (1996) 35-45.
[24] U. Stimming, J.W. Schultze, Ber Bunsen Phys Chem, 80 (1976) 1297-1302.
[25] A. Di Paola, Electrochim Acta, 34 (1989) 203-210.
[26] Y.F. Cheng, C. Yang, J.L. Luo, Thin Solid Films, 416 (2002) 169-173.
[27] J. Liu, D.D. Macdonald, J Electrochem Soc, 148 (2001) B425-B430.
[28] E. Sikora, D.D. Macdonald, J Electrochem Soc, 147 (2000) 4087-4092.
[29] K. Azumi, T. Ohtsuka, N. Sato, J Electrochem Soc, 134 (1987) 1352-1357.
[30] G. Nogami, J Electrochem Soc, 132 (1985) 76-81.
[31] M.H. Dean, U. Stimming, The Journal of Physical Chemistry, 93 (1989) 8053-8059.
[32] A. Simoes, M. Ferreira, B. Rondot, M. da Cunha Belo, J Electrochem Soc, 137 (1990) 82-87.
[33] Y.F. Cheng, J.L. Luo, Electrochim Acta, 44 (1999) 2947-2957.
[34] S.P. Harrington, T.M. Devine, J Electrochem Soc, 155 (2008) C381-C386.

[35] G. Brug, A. Van Den Eeden, M. Sluyters-Rehbach, J. Sluyters, Journal of electroanalytical chemistry and interfacial electrochemistry, 176 (1984) 275-295.
[36] I. Nicic, D.D. Macdonald, J Nucl Mater, 379 (2008) 54-58.
[37] E. Sikora, D.D. Macdonald, Electrochim Acta, 48 (2002) 69-77.
[38] E. Sikora, J. Sikora, D.D. MacDonald, Electrochim Acta, 41 (1996) 783-789.
[39] D.D. Macdonald, S.R. Biaggio, H. Song, J Electrochem Soc, 139 (1992) 170-177.
[40] D.D. Macdonald, M. Urquidi‐Macdonald, J Electrochem Soc, 137 (1990) 2395-2402.

Chapter 5 The Mixed Potential Model for Passive Systems

As discussed above, the corrosion rate of the metal is controlled by the positive anodic partial current density passing through the test surface, and therefore only knowledge of the negative total current density itself is not viable for predicting corrosion damage of carbon steel, unless a method is developed such that the partial anodic current density concealed in the total current density can be obtained. A Mixed Potential Model (MPM) combining the PDM to describe the partial anodic process and the Butler-Volmer equation to describe the cathodic process has been successfully developed, which allowed us to deconvolve the negative net current and to recover the passive current density for determination of the corrosion rate. In this MPM, the anodic partial current, which is microscopically brought about by the migration of various types of point defects through the passive film, is simulated by the PDM as described previously [Eq. (2-11)], while the cathodic current contributed by the cathodic partial process occurring in the system is treated by the Butler-Volmer equation that incorporates thermodynamic, kinetic, and mass-transport properties of the partial cathodic reaction. Adding these two partial currents yields the simulated total current density that can be tested by the actual current measurement in data optimization. The impedance induced by each partial current can then be calculated and combined with other impedance components at the interfaces to simulate the total observed impedance.

5.1 Incorporation of Partial Anodic Reactions

The seven fundamental point defect reactions (Figure 2-2), on which the PDM is based, do not address the cathodic reactions but only the formation of anodic passive film. Therefore, the original PDM has been employed to account for the partial anodic reactions. Results of Mott-Schottky analysis presented above in Chapter 4 has demonstrated that the passive film formed on carbon steel at lower potentials in alkaline solutions has an n-type semiconductor character, which indicates that metal vacancies are not the major point defect species existing within the film, and hence, Reactions (1) and (4) are excluded in the subsequent employment of the PDM on carbon steel studies. Correspondingly, expression for the anodic partial current density in steady state, which is equivalent to the steady state current density shown in Eq. (2-11), can be simplified as:

$$i_{anod} = i_{ss} = \delta F[k_2^0 \mathrm{e}^{a_2 V} \mathrm{e}^{b_2 L_{ss}} \mathrm{e}^{c_2 \mathrm{pH}} + k_7^0 \mathrm{e}^{a_7 V} \mathrm{e}^{c_7 \mathrm{pH}} \cdot (C_H / C_H^0)^n] \tag{5-1}$$

Then, by taking the derivative of i_{ss} in Eq. (5-1) with respect to the applied potential, V, the steady state current density is related to the applied potential by:

$$\left(\frac{\partial \ln i_{ss}}{\partial V}\right)_{pH, C_{M^{\delta+}}} = \alpha \alpha_7 (\delta - \chi) \gamma \tag{5-2}$$

where χ is the oxidation state of the metal in the barrier layer. Therefore, depending upon the values of the oxidation states of iron cations, δ and χ, the steady state current density would increase ($\delta > \chi$) or decrease ($\delta < \chi$) with potential, or stays potential-invariant ($\delta = \chi$).

The faradaic impedance Z_F originating from the fundamental point defect reactions, or the anodic reactions, have been derived in the latest PDM treating the passive film as a two-layer structure. Detailed interpretation and derivation of Z_F has been elaborated in Ref. [1], where linearization of the current response over small changes in applied potential (sinusoidal modulation) is employed as the approach to define the admittance and other parameters. To avoid repetition, only important formulae for calculating Z_F are presented here:

$$Z_F = 1/Y_F \tag{5-3}$$

$$Y_F = Y_F^0/(1 + R_{ol}Y_F^0) \tag{5-4}$$

$$Y_F^0 = I_U + I_L\frac{\Delta L}{\Delta U} + I_i^0\frac{\Delta C_i^0}{\Delta U} \tag{5-5}$$

and

$$I_U = F(\chi k_2 a_2 + \chi k_3 a_3) \tag{5-6}$$

$$I_L = -F(\chi k_2 b_2 + \chi k_3 b_3) \tag{5-7}$$

$$I_i^0 = F(\delta - \chi)k_5 \tag{5-8}$$

$$\frac{\Delta L}{\Delta U} = \frac{\Omega(k_3 a_3 - k_7 a_7)}{j\omega + \Omega k_3 b_3} \tag{5-9}$$

The derivation of $\Delta C_i^0/\Delta U$ is not presented here, which can be found in Ref. [1], due to the limited space. In the equations above, k_i, a_i, and b_i are parameters as defined in Table 2-3. Y_F^0 is the faradaic admittance across the barrier layer, while Y_F is the faradaic admittance across the whole film. Ω is the molar volume of the barrier layer per cation.

5.2 Incorporation of Partial Cathodic Reaction

The partial anodic reactions have been addressed in the above section and, next, the partial current density and impedance related to the cathodic reaction needs to be treated to complete the MPM. The dominant cathodic reaction in the electrochemical cell is judged to be hydrogen evolution reaction (HER) by water reduction:

$$2H_2O + 2e^- = H_2(g) + 2OH^- \quad (5\text{-}10)$$

Oxygen reduction is ruled out due to the oxygen content in the solution being rendered very low by continual sparging of argon gas into the cell during the entire experiment. Note that, although there are two electrons in the expression of Reaction (5-10), it has been generally acknowledged [2, 3] that the HER occurring in alkaline solutions proceed via one-electron transfer steps:

$$M + H_2O + e^- \Leftrightarrow M\text{-}H + OH^- \quad (5\text{-I})$$

$$M\text{-}H + H_2O + e^- \Leftrightarrow M + H_2 + OH^- \quad (5\text{-II})$$

and/or a chemical recombination reaction in which no electrons participates:

$$M\text{-}H + M\text{-}H \Leftrightarrow 2M + H_2 \quad (5\text{-III})$$

In the reactions above, Reaction (5-I) represents the adsorption of a hydrogen atom on the surface of the metallic electrode by forming a hydrogen bond with the metal atom, M-H. The adsorbed hydrogen atom can later be discharged in the form of hydrogen gas molecule by combining with another hydrogen atom via either Reaction (5-II) or (5-III) or both simultaneously. In view of the observation that the measured current density was dependent on potential, the HER is considered to proceed primarily via Reactions (5-I) to (5-III) with only Reactions (5-I) and (5-II) contributing to the partial cathodic current, because there is no electron taking part in Reaction (5-III). By further assuming that Reactions (5-I) and (5-II) are irreversible, which is viable at sufficiently negative overpotentials (>100 mV), and their transfer coefficients are equal, the cathodic current density, according to Butler-Volmer equation, can be written as:

$$i_{cath} = -2F\frac{k_I k_{II}}{k_I + k_{II}}\exp(-\alpha_c\frac{F\eta}{RT}) = -2Fk_c\exp(-\alpha_c\frac{F\eta}{RT}) \quad (5\text{-}11)$$

where k_{I} and k_{II} are the apparent rate constants for Reactions (5-I) and (5-II), respectively, which have units of mol cm^{-2} s^{-1}; k_c is a nominal rate constant, which approximately equals k_{I} when k_{II} is much larger than k_{I}, indicating Reaction (5-I) being the rate determining step, and vice versa; α_c is the transfer coefficient of the hydrogen evolution reaction; η is the cathodic overpotential for the HER. Since there is abundant source of the water, the species that is consumed in the HER, it is assumed that the system will be kinetically controlled within the applied potential range, i.e., no diffusional part has been taken into account in Eq. (5-11).

Eq. (5-11) can be written in an alternative form by adopting Tafel slope:

$$i_{cath} = -2Fk_c \exp\left(-\alpha_c \frac{F\eta}{RT}\right) = i_0 \exp(-\frac{2.303}{b_c}\eta) \tag{5-12}$$

and

$$b_c = 2.303RT/(\alpha_c F) \tag{5-13}$$

where i_0 and b_c are the exchange current density and the Tafel slope for the HER on the passive film of carbons steel.

Noting the observations [4-10] that the kinetics of HER occurring on the passive film surface behave differently as that occurring on a film-free surface, further modification has been made to the cathodic part. Evidences in the Ref. [4-10] have shown that the formation of anodic films have a profound impact on the kinetics of the redox reactions occurring at various metal surfaces and, hence, the quantum-mechanical effect of electrons tunneling across the film [11-13] need to be taken into account to describe the partial cathodic current density more accurately. Bao et al. [4] explained such impact by combining the quantum mechanical electron tunneling theory and the PDM, which describes the tunneling effect using a tunneling constant and ascribed the enhanced magnitude of the Tafel slope to the extra energy barrier brought about by electrons tunneling across the thin film. According to theory developed by Bao et al. [4], the quantum mechanical tunneling across a thin oxide film of thickness L on a metal surface yields a tunneling exchange current density, i_0, that can be expressed in the following simple form:

$$i_0 = \widehat{i_o} \exp\left(-\hat{\beta} L_{ss}\right) \tag{5-14}$$

where $\hat{\beta}$ is the tunneling constant (cm^{-1}), which defines the blocking character of the film, and $\widehat{i_o}$ is the "film-free" redox reaction current density. Furthermore, knowing that $L_{ss} \propto \frac{1-\alpha}{\varepsilon} V$ from Eq. (2-10) and combining Eqs. (5-12) to (5-14) yields

$$\ln i_{cath} = \ln \widehat{i_o} - \left(\frac{2.303}{b_c} + \frac{\hat{\beta}(1-\alpha)}{\varepsilon}\right)\eta + const. \tag{5-15}$$

Thus, by using the same Tafel form, the Tafel slope for the HER on completely film-free surface, $\widehat{b_c}$, satisfies the following relationship:

$$\frac{2.303}{\widehat{b_c}} = \frac{2.303}{b_c} + \frac{\hat{\beta}(1-\alpha)}{\varepsilon} \tag{5-16}$$

Noting that the term $\hat{\beta}(1-\alpha)/\varepsilon$ is positive, the Tafel slope of HER on the film surface is expected to be much larger than that on a film-free surface, indicating that the cathodic current density will be less dependent on the applied voltage, i.e. $b_c > \widehat{b_c}$.

By taking the derivative of i_{cath} with respect to E, we derive the admittance of cathodic reaction as:

$$Y_{cath} = \frac{di_{cath}}{dE} = 2\alpha_c \frac{F^2}{RT} k_c \exp\left[-\alpha_c \frac{F}{RT}\left(E - E_{eq}\right)\right] = -\alpha_c \frac{F}{RT} i_{cath} \tag{5-17}$$

and the impedance of the cathodic reaction is then:

$$Z_c = {Y_{cath}}^{-1} = R_c \tag{5-18}$$

There is no imaginary part in the expression of Z_c, so the impedance is denoted as a resistance, R_c. The total current density produced by the system is then the sum of Eq. (5-1) and Eq. (5-16):

$$i_{total} = i_{anod} + i_{cath} \tag{5-19}$$

which will have a negative value if the magnitude of (negative) i_{cath} is larger than that of the (positive) i_{anod}.

At this point, the current densities and impedance attributed to both the partial anodic and the partial cathodic processes, as well as the total current density and total impedance observed in the system, have been simulated by the MPM. The simulated total current density and impedance will be tested against the experimental data during the process of optimization of the MPM, which will eventually yield the fundamental kinetic parameters of the anodic point defect reactions and cathodic hydrogen evolution, as detailed in the next chapter.

References

[1] S. Sharifi-Asl, M.L. Taylor, Z. Lu, G.R. Engelhardt, R. Kursten, D.D. Macdonald, Electrochim Acta, 102 (2013) 161-173.
[2] A. Lasia, A. Rami, J Electroanal Chem, 294 (1990) 123-141.
[3] Y. Choquette, L. Brossard, A. Lasia, H. Menard, J Electrochem Soc, 137 (1990) 1723-1730.
[4] J. Bao, D.D. Macdonald, J Electroanal Chem, 600 (2007) 205-216.
[5] J. Boodts, S. Trasatti, Journal of applied electrochemistry, 19 (1989) 255-262.
[6] R. Torresi, O. Camara, C. De Pauli, M. Giordano, Electrochim Acta, 32 (1987) 1291-1301.
[7] T.P. Moffat, H. Yang, F.R.F. Fan, A.J. Bard, J Electrochem Soc, 139 (1992) 3158-3167.
[8] S. Schuldiner, J Electrochem Soc, 115 (1968) 362-365.
[9] T. Dickinson, R. Greef, L. Wynne-Jones, Electrochim Acta, 14 (1969) 467-489.
[10] J. Schultze, K. Vetter, Electrochim Acta, 18 (1973) 889-896.
[11] W. Schmickler, Journal of Electroanalytical Chemistry and Interfacial Electrochemistry, 84 (1977) 203-207.
[12] W. Schmickler, J. Ulstrup, Chemical Physics, 19 (1977) 217-232.
[13] H. Gerischer, Electrochim Acta, 35 (1990) 1677-1699.

Chapter 6 Optimization of the Mixed Potential Model on EIS Data

6.1 Introduction to the Optimization

As demonstrated in Chapter 5, the faradaic impedance, Z_F, arising from the interfacial point defect reactions at m/bl and bl/ol(s) interfaces is a function of the set of the kinetic parameters (i.e. standard rate constants and transfer coefficients) of the point defect reactions occurring at the interfaces of the barrier layer. Therefore, it is possible that, by first measuring the impedance of the system and then performing optimization of the MPM on the experimentally measured impedance data, the values of those kinetic parameters governing Z_F, a contributory part of the total impedance of the system, can be extracted. Note that, because it is always the total impedance of the electrochemical system that is measured, which comprises all of the contributory interfacial phenomena including those occurring at the metal\film\solution interfaces plus the solution resistance, additional components need to be combined with Z_F in order to represent the total impedance of the system, on which the optimization was done (i.e. we know of no way to experimentally determine exclusively the faradaic impedance of the barrier layer of a passive film in an aqueous solution). The simulation of the total system impedance is achieved in this work by combination of the analog approach (equivalent electrical circuit) and the analytic model (the MPM).

Because the optimization is primarily based on the EIS data, a proper equivalent circuit, which serves as the operational body of impedance, is critical to obtaining valid and accurate results. A well-designed equivalent circuit should accurately represent all electrochemical processes that make contributions to the total impedance of the system. Several circuits have been proposed for the optimization within this work, and after tests and trials the circuit depicted in Figure 6-1 is adopted, which provides the best convergence of simulation and experimental results, as well as yielding parameters with reasonable values and sound physical meanings, as demonstrated in following sections.

In general, the equivalent circuit in Figure 6-1 contains two segments in series: the right-hand side circuit that includes R_s and a parallel R_{ol}-C_{ol} combination embodies the impedance contribution from the outer-layer and the solution, while the portion of the circuit on the left is attributed to the phenomena occurring within the barrier layer and at its interfaces. The barrier layer segment can be further split into two branches in parallel: an anodic-reaction branch and a cathodic-reaction branch. The former includes the faradaic impedance, Z_F, the Warburg impedance, W, which associates with the transport of defects across the barrier layer, and C_g, the geometric capacitance, which occurs because of storage of electronic charge at two interfaces that are separated by the dielectric barrier layer. A constant phase element is adopted here to characterize the time-constant dispersion of C_g, which is possibly due to the non-uniform thickness distribution of the barrier layer on a polycrystalline metallic surface, although it was reported by Cattarin et al. [1] that this inhomogeneity of thickness cannot be accurately modelled by a constant phase element.

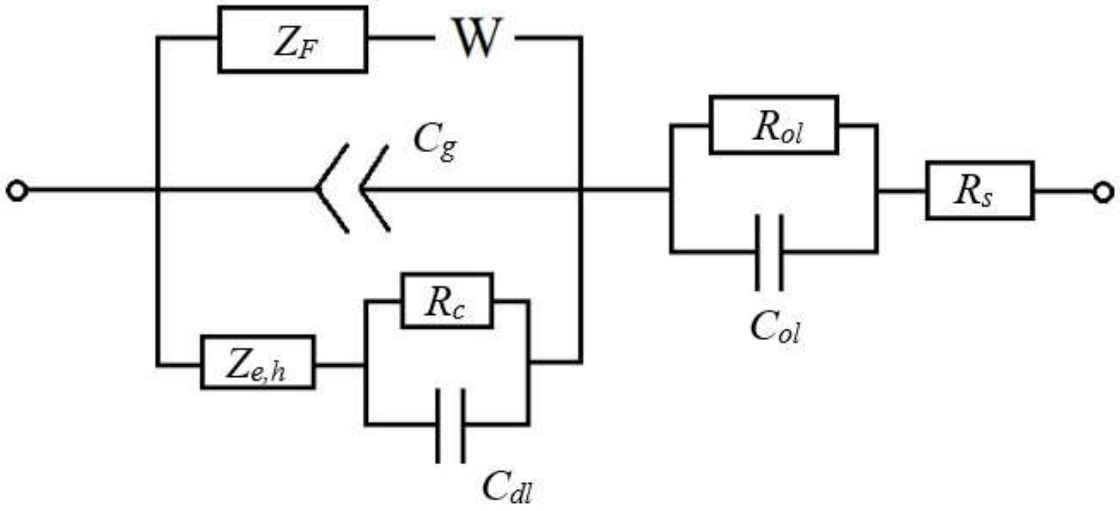

Figure 6-1: The equivalent electrical circuit designed for simulating the total interfacial impedance of the passive system of carbon steel in the SCPS.

A circuit comprising $Z_{e,h}$ in series with a parallel R_c-C_{dl} combination is placed in parallel to the anodic branch to represent the impedance of the cathodic hydrogen evolution that is assumed occurring at the bl/ol interface, where $Z_{e,h}$ is the diffusional impedance of electrons and/or electronic holes through barrier layer (detailed derivation presented in Ref. [2]), R_c is the resistance of charge transfer via the cathodic reaction as defined in Eq. (6) and C_{dl} is the capacitance of the double layer. No diffusional impedance is assigned to the cathodic reaction, due to the abundant source of water, the species that is reduced. Since there is almost no free electrons existing in the SCPS (i.e. the extent of solvation of electrons is very small and regarded as being negligible), $Z_{e,h}$ is arranged in series with the cathodic reaction so that the electronic charges travelling across the barrier layer can be accepted by the redox couple of H_2O/OH^-.

At last, based on the adopted equivalent circuit, the total impedance of the interfacial system can be written as

$$Z_{total} = [(Z_F + Z_W)^{-1} + Z_{C_g}^{-1} + Z_{cath}^{-1}]^{-1} + Z_{ol} + R_s \tag{6-1}$$

where Z_{cath} and Z_{ol} are the impedance of the cathodic-reaction branch and that of the outer-layer, respectively:

$$Z_{ol} = [R_{ol}^{-1} + j\omega C_{ol}]^{-1} \tag{6-2}$$

and

$$Z_{cath} = [R_c^{-1} + j\omega C_{dl}]^{-1} \tag{6-3}$$

With the selected equivalent circuit and the developed theory of the MPM, the optimization of the MPM on the EIS data can be started. IGOR Pro (version 6.22A) commercial software employing a genetic algorithm was used in this work for conducting the optimization. In general, the optimization process aims to search a set of qualified optimization results, including the kinetic parameters of the (anodic) point defect reactions and the (cathodic) hydrogen evolution reaction, the parameters related to the passive electrical components in the equivalent circuit, and all other unknown parameters that appear in the derivation of the MPM presented in Chapter 5. In order to be considered qualified, the set of optimization results must have values with appropriate physical meaning for all parameters and must be able to generate a simulated steady-state total current density and a simulated total impedance of the system, simultaneously, that match the experimental data. The optimization process was started by assigning reasonable initial values and ranges to each of the parameters ("initial guesses") based on scientific approximation, literature, and previous optimization work. For instance, the transfer coefficients of the point defect reactions have to fall between 0 and 1; the double layer capacitance has been generally reported to have values of $10^{-5} \sim 10^{-7}$ F/cm^2; experiences from previous optimization work in this research group indicate that 10^{-10} mol cm^{-2} s^{-1} is a good initial value to start with for the standard rate constants, etc. The ranges of the parameters can be later adjusted, e.g. shifted and/or narrowed, to expedite the optimization process and produce more accurate optimization results. The Igor Pro genetic algorithm was then executed to perform the optimization. By the end of the optimization, we expect to obtain the standard rate constants, k_i^o, transfer coefficients, α_i, for the ith fundamental interfacial point defect reactions (Figure 2-2); the rate constant and transfer coefficient for the hydrogen evolution reaction by water reduction, k_c, α_c, respectively; the Warburg coefficient, σ, for Z_W; the parameters for all other components in the equivalent circuit, and, eventually, the deconvolved anodic partial current density, i_{ss} [Eq. (2)] and the cathodic partial current density, i_{cath} [Eq. (10)], from the negative total current density. By further inspection of these parameters originating from the opposite potential stepping directions, the kinetic nature of the observed corrosion irreversibility is expected to be elaborated.

Table 6-1 lists the parameters that are held constant during the optimization and their sources. They were either derived or assumed appropriately, based on literature sources and previous optimization work performed on carbon steel and iron in the similar experimental environments. Due to the limited access to the precise *in situ* characterization instruments, no characterization work was conducted in this project to probe the precise composition of the passive film on carbon steel. Note that it has been well demonstrated [3-7] that taking specimens out of the aqueous solution for *ex situ* characterization, during which the specimens are exposed to atmosphere or vacuum, changes more or less (often appreciably) the composition and structure of the passive film, and thus results obtained by *ex situ* techniques are not referred to in this work. However, numerous studies [8-11] have demonstrated that the barrier layer (oxide layer) of the passive film formed on iron and carbon steel in alkaline solutions are primarily composed of Fe^{3+} oxide (Fe_2O_3) with a finite amount of Fe^{2+} cations (existing in the form of Fe_3O_4 or oxides with stoichiometry close to Fe_3O_4) [10]. Although the ratio of Fe^{2+}/Fe^{3+} is found to increase as the film formation potential is lowered, the Fe^{3+} cation still dominates over Fe^{2+} within the applied potential range adopted here (-600 mV_{SHE} to 0 mV_{SHE}) [8]. Therefore, χ is accepted as being +3, due to the fact that Fe^{3+} is the dominant oxidation state of iron in the inner oxide layer. χ and δ are both selected as +3, by assuming that, within the potential range of -600 mV_{SHE} and 0 mV_{SHE} in the SCPS, the composition of the barrier layer as being Fe_2O_3 and that of the outer-layer as being

FeOOH or $Fe(OH)_3$ [8, 10-13]. The solution resistance was estimated from the real part of the impedance measured at 10000 Hz in the EIS.

Table 6-1: Values and sources of parameters that are held constant in optimization.

Parameters	**Values**	**Sources**
Polarizability of bl/ol interface (α)	0.15	Ref. [14] (also see Sec. 8.2.1)
Dependence of the potential drop across bl/s upon pH (β)	-0.01	Ref. [14] (also see Sec. 8.3)
Kinetic order of Reaction 7 (n)	0.5	Assumed
Electric field strength within bl (ε)	3×10^6 V cm^{-1}	Assumed
Dielectric constant of the film (ε_f)	30	Ref. [15]
Oxidation state of cation in bl (χ)	+3	Assumed [8, 10-13]
Oxidation state of cation in ol (δ)	+3	Assumed [8, 10-13]
Solution resistance (R_s)	7 Ω cm^2	From EIS results

6.2 Optimization Results of the Kinetic Parameters

The kinetic parameters of the point defect reactions extracted from the optimization for both the anodic and cathodic potential stepping directions are presented in Table 6-2 and Table 6-3. The relationship between the kinetic parameters and the film formation potential is illustrated in Figure 6-2. In Figure 6-2(a), the standard rate constants exhibit the expected independence of the potential, which complies with electrochemical fundamentals that these parameters are standard parameters and should be potential-invariant. By comparing k_i^o from the two potential stepping directions, one can discover that k_3^0, the standard rate constant related to the film growth, has slightly larger values during the reverse potential stepping, while the values of k_7^0, the rate constant related to film dissolution, at descending potentials, are about one order in magnitude smaller than those at rising potentials. The dependence of the standard rate constants on the potential stepping direction is probably associated with the different defect structures of the passive film at equivalent potentials upon opposite potential stepping, as observed in M-S analysis.

Note that it is k_i that directly controls how fast the reactions proceed, rather than k_i^0 (i.e. k_i^0 is the inherent pre-factor of k_i). Examination of k_3 and k_7 from the two potential stepping directions allows us to understand that the fundamental difference of the kinetics of the passive film between the opposite anodic and cathodic potential stepping directions is responsible for the corrosion irreversibility of carbon steel. It is noticed that, in Figure 6-2(b), both k_3 and k_7 from the reverse potential stepping direction are about one order of magnitude smaller than those from the forward potential stepping, which indicates a lower dissolution rate as well as a lower growth rate of the passive film when the film formation potential is displaced in cathodic direction. This indicates that the passive film behaves more inertly in terms of the kinetics of the fundamental point defect reactions occurring at the interfaces in response to the negative potential excursion. Again, k_i, rather than k_i^0, represents the actual growth and dissolution rate of the film, and hence, although k_3^0 has larger values during the reverse stepping, the film growth is actually slower compared to the forward stepping, due to the smaller values of k_3. Therefore, it is concluded that, upon the cathodic potential stepping, the kinetic processes of film growth and film dissolution become much slower compared to the rates during the anodic stepping, and this irreversibility in kinetics is the origin of the irreversible passivation that has been observed for carbon steel in the SCPS.

Table 6-2: Values of kinetic parameters obtained from the optimization of the MPM on the EIS data from the anodic potential stepping of carbon steel in the deaerated SCPS (pH=13.5, 25°C).

Potential (mV_{SHE})	-600	-500	-400	-300	-200	-100	Average
α_2	0.25	0.20	0.38	0.33	0.22	0.27	0.22
α_3	0.65	0.59	0.45	0.55	0.42	0.50	0.55
α_7	0.23	0.21	0.35	0.39	0.13	0.36	0.25
k_2^0 (mol cm^{-2} s^{-1})	6.66×10^{-13}	9.26×10^{-13}	4.64×10^{-13}	8.82×10^{-13}	5.59×10^{-13}	8.07×10^{-13}	5.43×10^{-13}
k_3^0 (mol cm^{-2} s^{-1})	2.30×10^{-17}	1.44×10^{-16}	4.42×10^{-17}	4.40×10^{-16}	1.21×10^{-16}	8.14×10^{-16}	3.11×10^{-16}
k_7^0 (mol cm^{-2} s^{-1})	9.34×10^{-10}	8.89×10^{-10}	8.85×10^{-10}	5.69×10^{-10}	7.53×10^{-10}	6.23×10^{-10}	5.85×10^{-10}
k_2 (mol cm^{-2} s^{-1})	1.02×10^{-13}	2.89×10^{-13}	1.39×10^{-13}	2.81×10^{-13}	3.69×10^{-13}	1.30×10^{-13}	2.92×10^{-13}
k_3 (mol cm^{-2} s^{-1})	2.11×10^{-17}	6.39×10^{-17}	1.59×10^{-17}	9.05×10^{-17}	1.21×10^{-16}	8.11×10^{-17}	3.37×10^{-17}
k_7 (mol cm^{-2} s^{-1})	5.85×10^{-10}	6.23×10^{-10}	7.53×10^{-10}	5.69×10^{-10}	8.85×10^{-10}	1.89×10^{-9}	4.56×10^{-10}
k_c (mol cm^{-2} s^{-1})	1.70×10^{-13}	2.10×10^{-13}	1.92×10^{-13}	9.15×10^{-13}	9.05×10^{-13}	-	4.79×10^{-13}
α_c	0.141	0.142	0.138	0.122	0.122	-	0.133
σ (Ω $s^{-1/2}$)	8.84×10^{5}	1.37×10^{6}	6.61×10^{5}	6.91×10^{5}	9.16×10^{5}	6.28×10^{5}	1.79×10^{6}

Table 6-3: Values of kinetic parameters obtained from the optimization of the MPM on the EIS data from the cathodic potential stepping of carbon steel in the deaerated SCPS (pH=13.5, 25°C).

Potential (mV_{SHE})	-600	-500	-400	-300	-200	-100	Average
α_2	0.21	0.26	0.24	0.33	0.24	0.37	0.29
α_3	0.55	0.57	0.60	0.60	0.47	0.56	0.56
α_7	0.49	0.63	0.54	0.38	0.05	0.69	0.46
k_2^0 (mol cm^{-2} s^{-1})	9.01×10^{-13}	9.14×10^{-13}	9.24×10^{-13}	7.48×10^{-13}	8.44×10^{-13}	1.16×10^{-13}	7.09×10^{-13}
k_3^0 (mol cm^{-2} s^{-1})	5.39×10^{-17}	3.36×10^{-16}	7.64×10^{-16}	8.58×10^{-16}	6.43×10^{-16}	2.10×10^{-15}	9.40×10^{-16}
k_7^0 (mol cm^{-2} s^{-1})	7.44×10^{-11}	6.51×10^{-11}	9.79×10^{-11}	6.88×10^{-11}	9.43×10^{-11}	9.38×10^{-11}	8.40×10^{-11}
k_2 (mol cm^{-2} s^{-1})	3.70×10^{-14}	1.28×10^{-13}	5.83×10^{-14}	2.02×10^{-13}	1.92×10^{-13}	4.87×10^{-14}	1.12×10^{-13}
k_3 (mol cm^{-2} s^{-1})	1.50×10^{-17}	1.49×10^{-17}	1.61×10^{-17}	1.72×10^{-17}	5.27×10^{-17}	4.10×10^{-17}	2.61×10^{-17}
k_7 (mol cm^{-2} s^{-1})	9.38×10^{-11}	9.43×10^{-11}	6.88×10^{-11}	9.79×10^{-11}	2.96×10^{-10}	2.30×10^{-10}	1.31×10^{-10}
k_c (mol cm^{-2} s^{-1})	7.95×10^{-13}	7.00×10^{-13}	2.13×10^{-13}	3.04×10^{-13}	7.31×10^{-13}	7.37×10^{-13}	3.98×10^{-13}
α_c	0.152	0.151	0.139	0.147	0.131	-	0.144
σ (Ω $s^{-1/2}$)	4.21×10^{5}	1.78×10^{5}	1.34×10^{5}	2.81×10^{5}	2.20×10^{5}	3.17×10^{5}	2.59×10^{5}

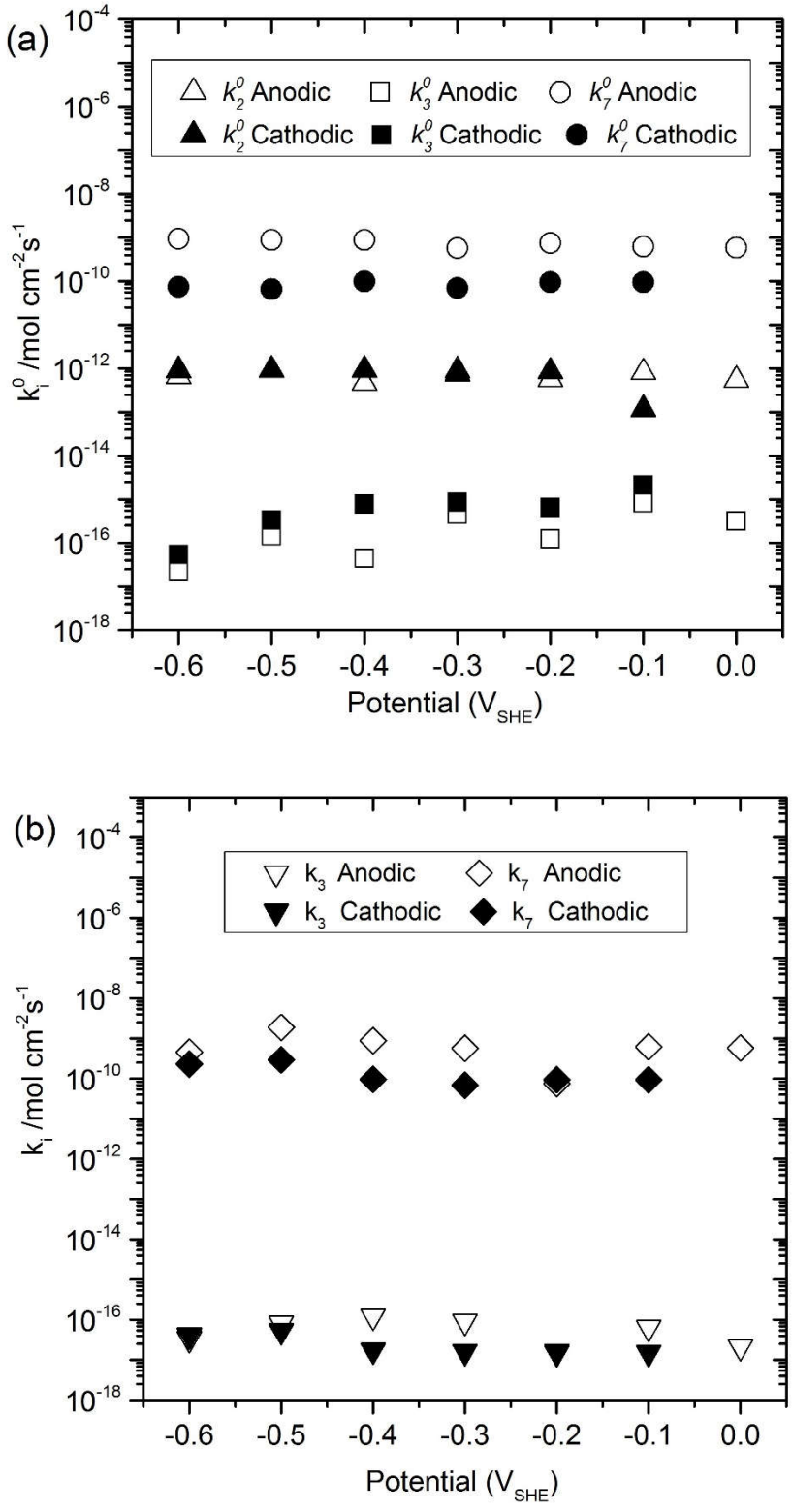

Figure 6-2: Optimization results for: (a**)** standard rate constants k_i^o; and (b) apparent rate constant k_i of the point defect reactions for both anodic and cathodic potential stepping directions.

6.3 Optimization Results of the Current Densities

In Figure 6-3, where the deconvolved i_{ss} is plotted as a function of the film formation potential in both potential stepping directions, i_{ss} appears to be independent of the potential regardless of the potential stepping direction, as predicted by the PDM for n-type films when $\delta = \chi$ holds, according to Eq. (5-2). Furthermore, i_{ss} at all potentials for the cathodic potential stepping are observed to be smaller than those for the anodic potential stepping, with the mean value of the former, 29.2 nA/cm^2, being smaller than one half of the mean value of the latter, 68.8nA/cm^2, which demonstrates directly the resistance of carbon steel to cathodic potential excursion. The corrosion rate of carbon steel can then be calculated readily from the partial anodic current density by applying Faraday's Law of mass-charge equivalence, which yields average values of 0.537 μm/year and 0.228 μm/year for the anodic and cathodic potential stepping, respectively, assuming the number of electron equivalents as being 3. The corrosion rate for the cathodic potential stepping (0.228 μm/year), which resembles the decreasing corrosion potential of carbon steel inside the Supercontainer, results in a 22.8 mm thickness loss for the over pack after 100,000 years, leaving only 7.2 mm wall-thickness there. However, it has to be recognized that this estimation is based on the presumption that the Supercontainer corrosion system will not change within the 100,000-year service horizon, which is very unlikely to be true. This uncertainty once again accentuates the imperativeness to possess the knowledge of the corrosion evolution path, so that a more accurate corrosion damage can be defined.

As for the deconvolved $i_{cath,}$ an expected linear Tafel relationship between it and the applied potential is observed in both potential stepping directions (Figure 6-4). The Tafel slopes (of the hydrogen evolution) are obtained by linear fitting the data as -450 mV/dec and -416 mV/dec respectively for the anodic and cathodic potential stepping. The closeness of these two values implies that the direction of the potential displacement exerts no pronounced influence on the kinetics of the cathodic reaction occurring on carbon steel, a finding also observed for the hydrogen evolution on Ti oxide film[16]. Furthermore, as predicted by the electron tunneling effect across the passive film incorporated in the MPM, the Tafel slopes obtained here are noticeably larger than those for the kinetically-controlled hydrogen evolution on bare iron electrode in alkaline solutions (-120 mV/dec [17, 18]). By inserting $\widehat{b_c}$ = -120 mV/dec and b_c = -433 mV/dec (the mean value of b_{anod} and b_{cath}) back into Eq. (5-16), the tunneling constant $\hat{\beta}$ for the passive film on carbon steel in the SCPS can be readily calculated as being equal to 0.87×10^8 cm^{-1}, which has the same order of magnitude of the tunneling constant previously obtained for the film on platinum surface, 0.58×10^8 cm^{-1} [19].

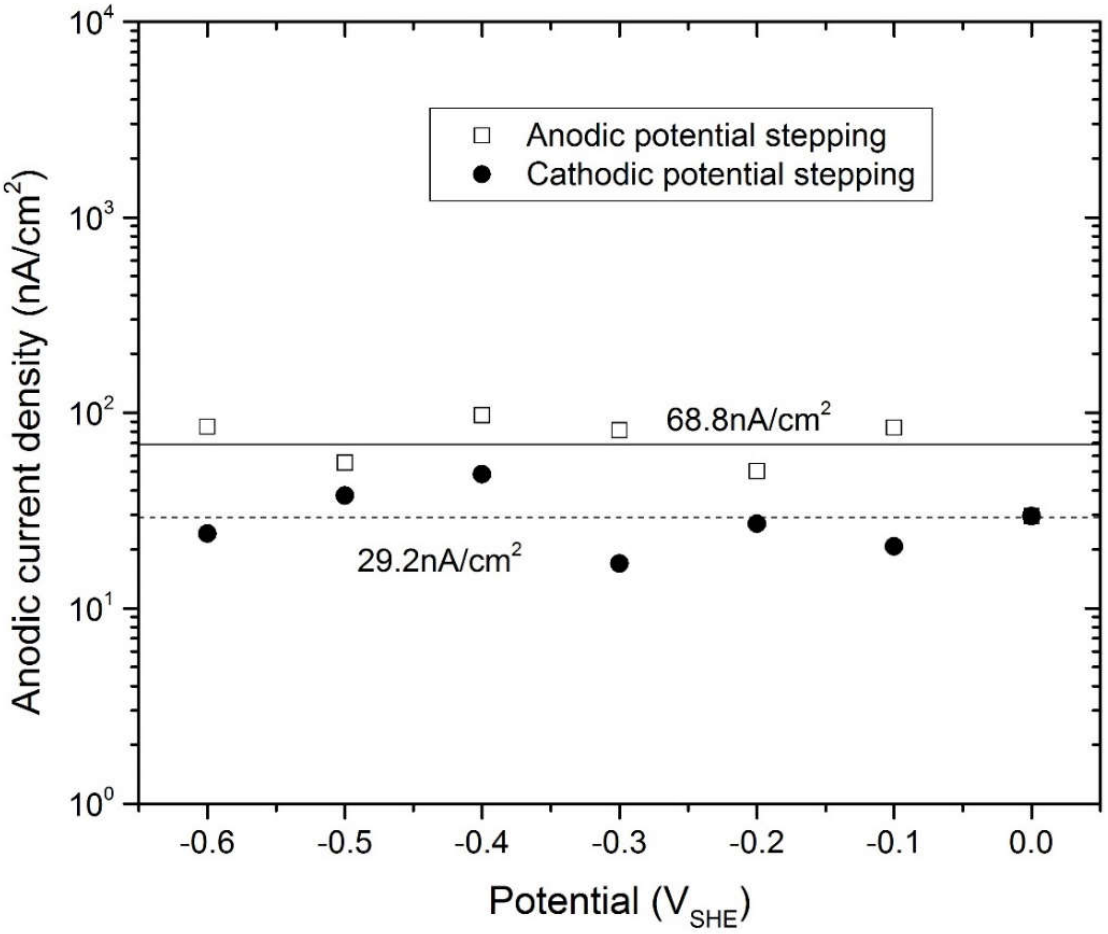

Figure 6-3: The **s**teady-state anodic current density of carbon steel deconvolved from the optimization of the MPM on the EIS in the deaerated SCPS as a function of the film formation potential for both the anodic cathodic potential stepping

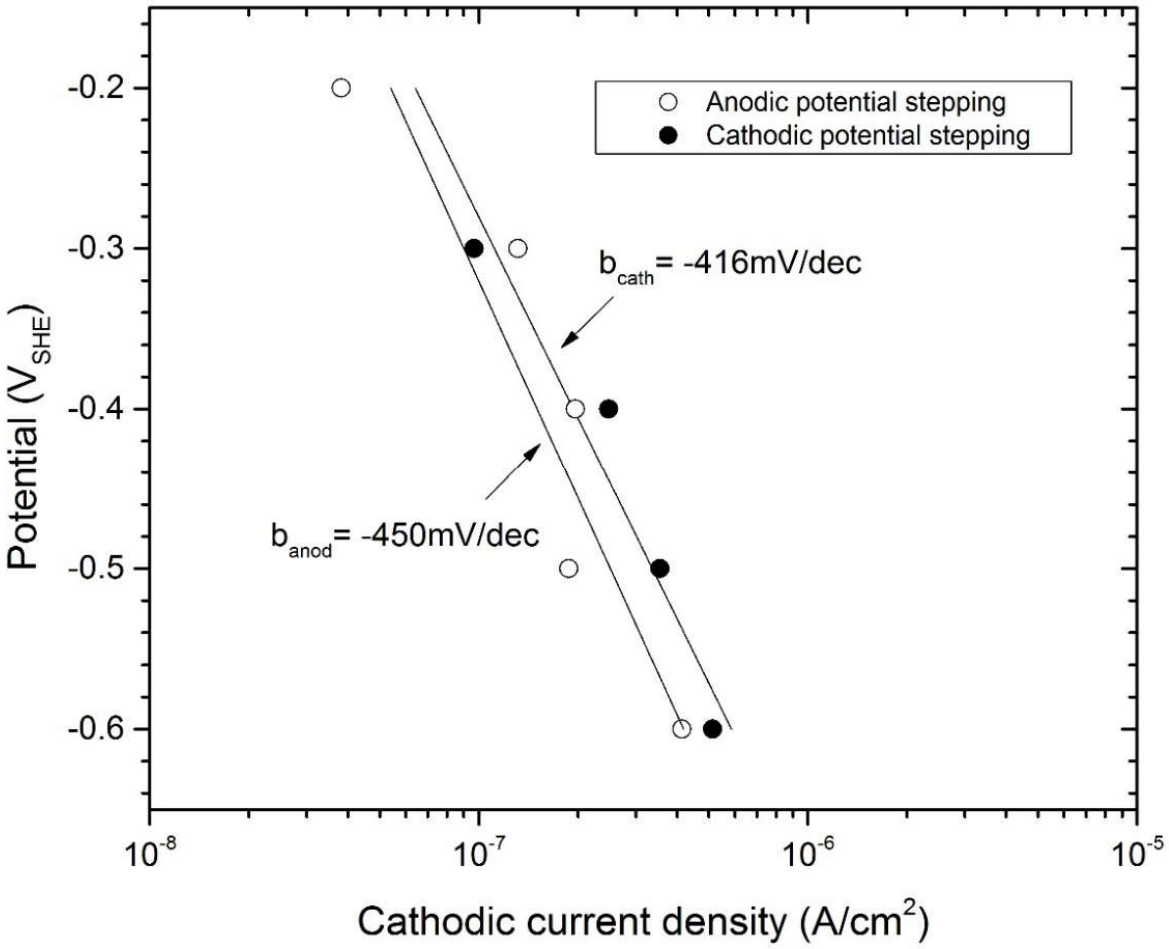

Figure 6-4: The partial cathodic current density obtained from the optimization of the MPM on the EIS data plotted as a function of applied potential. Results for both potential stepping directions are included.

6.4 Optimization Results of the Thickness of the Barrier Layer

The steady-state thickness of the barrier layer of the film calculated from Eq. (1) is plotted as a function of the applied voltage and included in Figure 6-5. The calculated thickness ranges from 0.7 nm to 1.7 nm, and, as same as the thickness values obtained from the capacitance measurement, it varies linearly with the applied potential. The coefficient $\partial L/\partial V$ is obtained to be 1.6 nm/V and 1.2 nm/V respectively for the anodic and cathodic stepping directions, showing a slower rate of film thinning upon cathodic potential stepping than film growing upon anodic potential stepping, a result of the kinetic irreversibility of the passive film as demonstrated above. Additional sets of passive film thickness data for iron acquired by various types of other techniques have been extracted from the literature [15, 20-24], with which the results of this work are compared and also shown in Figure 6-5. Note that, because of the paucity of film thickness data in the literature for conditions that are comparable to those applied in this study (i.e. highly alkaline solution and very negative potentials at the same time), all the data cited in Figure 6-5 were acquired in neutral or weakly alkaline solutions (e.g. borate buffer solutions) and at higher film formation potentials. Indeed, there is plenty of published work employing either high alkalinity or cathodic environment, but rarely those two conditions combined. Nevertheless, it has been demonstrated that, in neutral and alkaline solutions, the thickness of the barrier layer is almost independent on pH at constant film formation overpotentials [25], an observation related to the rather small value of β (-0.01, Table 6-1) which produces a weak dependence of passive film properties on pH. Therefore, it is argued here that the comparison between the film thickness results obtained at pH 13.5 in this study and those obtained at lower pH retains reasonable extent of validity. To make comparison, the film thickness calculated in this work need to be extrapolated linearly to more anodic potentials, and it is evident that the extrapolated part falls well within the range of the film thickness values reported in the literature. The anodizing constant, $\partial L/\partial V$, obtained here is also found coinciding well with those in the cited work (1.4 nm/V to 2.5 nm/V).

Figure 6-6 shows the comparison the barrier layer thickness obtained from optimization and the film thickness estimated from experimental capacitance measurement. The latter approach assumes the film is a simple parallel plate capacitor and the film thickness is calculated from $L = \varepsilon_0\varepsilon_f/C_f$, where C_f is the capacitance measured at a single high frequency of 5000 Hz at each film formation potential; $\varepsilon_f = 30$ as previously assumed. It is also noteworthy in Figure 6-6 that, for the case of anodic potential stepping, the experimental and simulated thickness data lines almost have the same starting point at -600 mV_{SHE}, however, the latter has a smaller slope (+1.6 nm/V) than the former (+2.2 nm/V), causing the simulated thickness being thinner than the measured thickness at higher potentials and the difference between them becomes larger as the potential rises. The divergence could be a result of the intrinsic difference between the two employed methods and the over-simplification of the film as being a parallel plate capacitor, but it can also be understood from another perspective by noticing that the film thickness calculated from the PDM only accounts for the inner barrier layer while the capacitance measurement collects the response across the entire bi-layer passive film (barrier layer plus outer-layer). Therefore, by this interpretation, the distance between the two thickness lines can be regarded as the reflection of the existing outer-layer and the increasing distance indicates that the outer-layer had been thickening during the experiment.

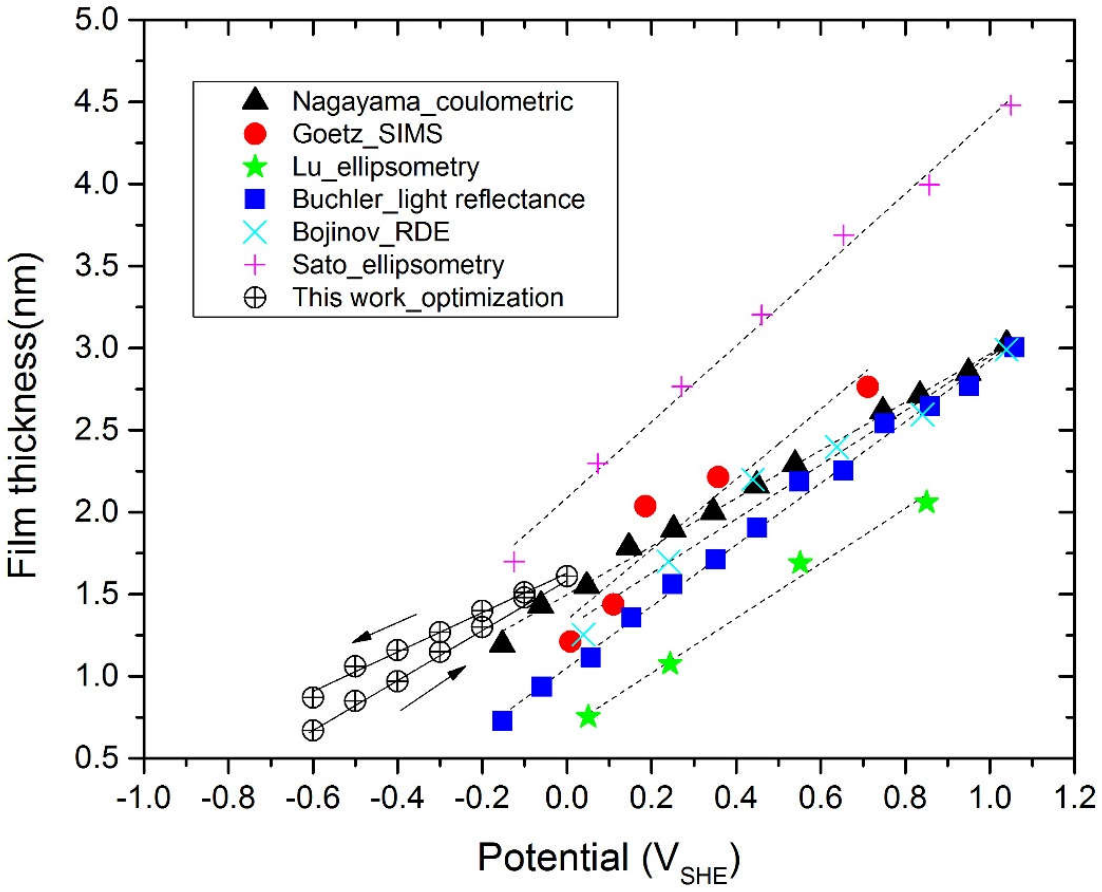

Figure 6-5: The thickness of the barrier layer on carbon steel in the deaerated SCPS (pH=13.5, 25°C) obtained from optimization of the MPM on EIS data and those obtained experimentally by various techniques [15, 20-24]. The arrows represent the direction of potential stepping.

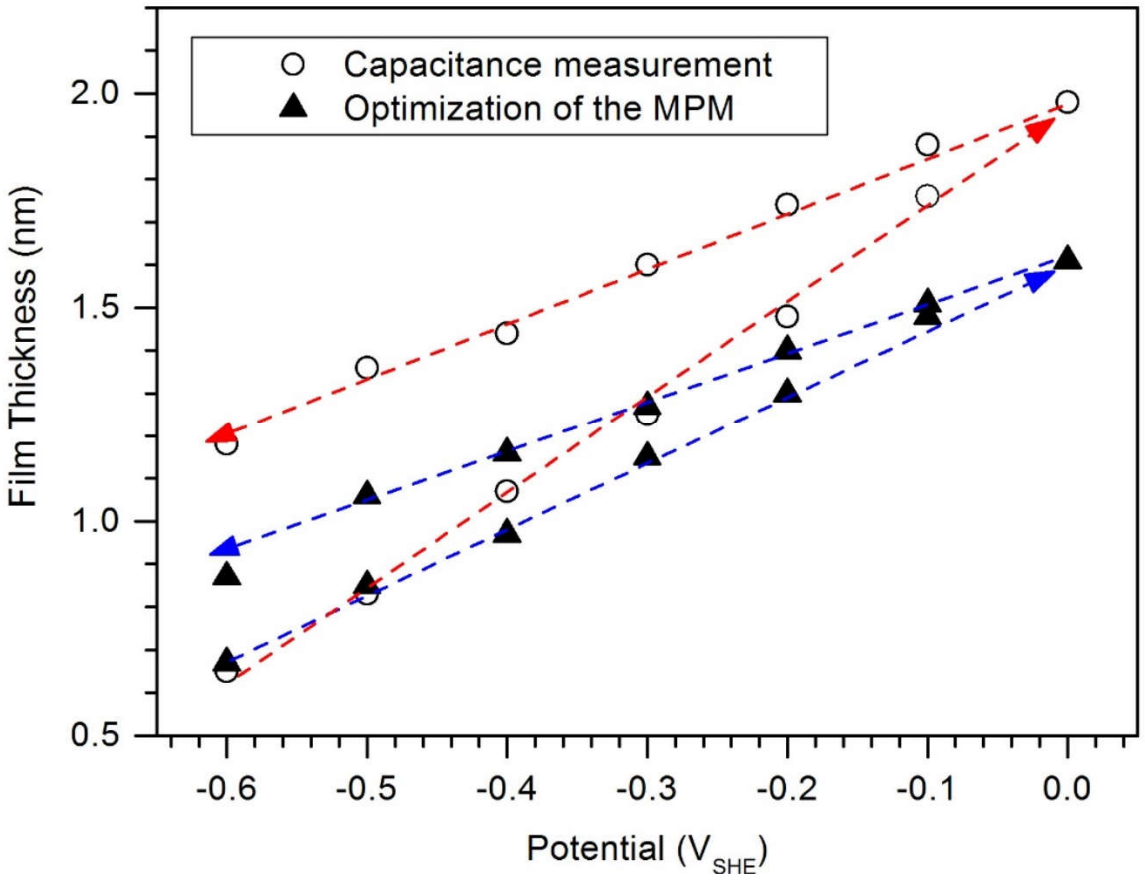

Figure 6-6: Comparison of the passive film thickness values estimated by capacitance measurement and calculated by optimization of the MPM.

6.5 Optimization Results of the Point Defect Diffusivity

The diffusivity of the point defects within the barrier layer can be evaluated via the PDM from the equation given below [26]:

$$\sigma = \frac{1}{I_{ss}} \times \sqrt{D_d/2} \times \frac{\varepsilon}{1-\alpha} \tag{6-4}$$

where σ is the Warburg coefficient, I_{ss} is the anodic current (not current density) in the steady-state, D_d is the diffusivity of point defects. It is instructive to note from Table 6-2 and Table 6-3 that the apparent rate constant for cation interstitial generation, k_2, is significantly greater (3~4 orders) than that for oxygen vacancy generation, k_3. This confirms that iron interstitials are the dominant point defects within the barrier layer on carbon steel, as previously concluded [2, 27, 28], which might be attributed to the lower energy of formation of cation interstitials than the formation of oxygen vacancies due to the larger radius of oxygen vacancy. Accordingly, the diffusivity of point defects obtained here is regarded exclusively as the diffusivity of iron interstitials (denoted as D_i). By referring to the data presented in Tables 6-1 to 6-3, D_i at different film formation potentials have been calculated from Eq. (6-4) and are plotted versus potential in Figure 6-7. A potential independence of potential as observed in kinetic parameters is also seen here in D_i. The mean value of D_i for the anodic potential stepping, 3.55×10^{-16} cm^2/s, is about five times greater than that for the cathodic potential stepping, 7.36×10^{-17} cm^2/s, which results from the irreversibility of film formation and dissolution upon different potential stepping directions, too. The diffusivity values obtained here are consistent to those reported in other work on iron or carbon steel (~10^{-16} cm^2/s) [20, 29-31].

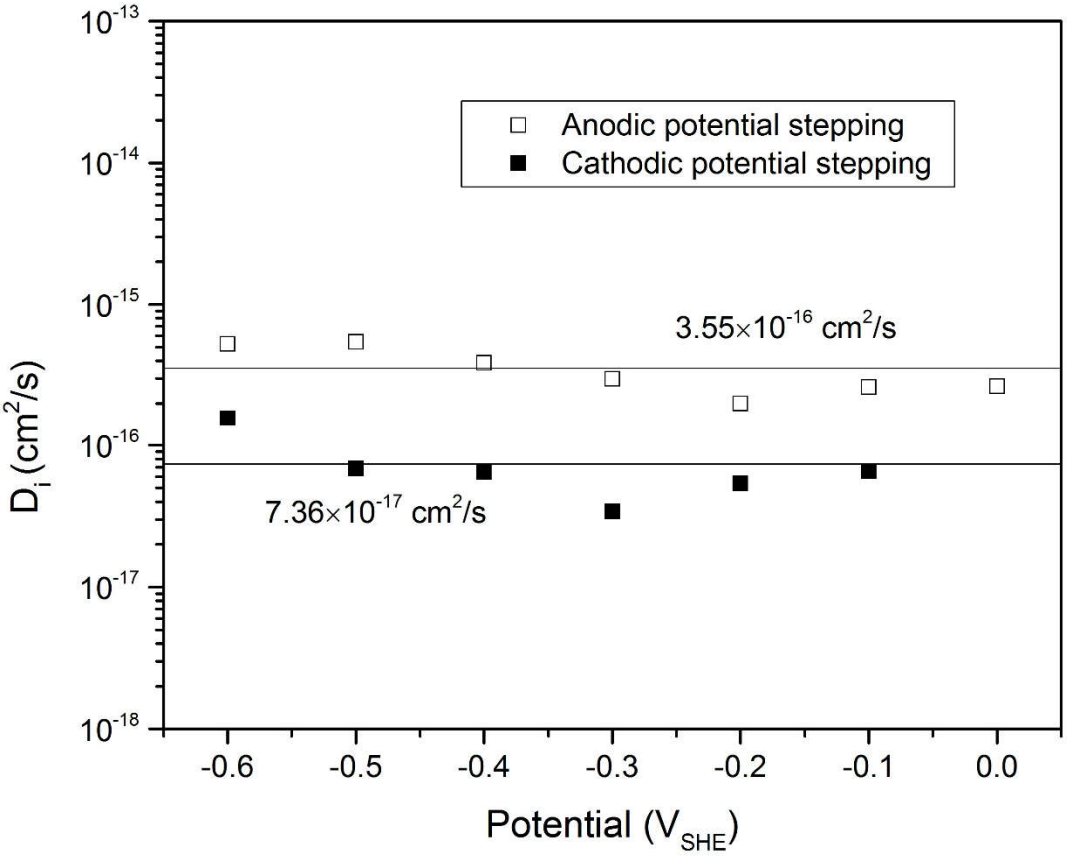

Figure 6-7: Diffusivity of cation interstitials within the barrier layer calculated from the Warburg coefficients for the anodic potential stepping and the cathodic potential stepping.

References

[1] S. Cattarin, N. Comisso, M. Musiani, B. Tribollet, Electrochemical and Solid-State Letters, 11 (2008) C27-C30.
[2] S. Sharifi-Asl, M.L. Taylor, Z. Lu, G.R. Engelhardt, R. Kursten, D.D. Macdonald, Electrochim Acta, 102 (2013) 161-173.
[3] J. Kruger, Corros Sci, 29 (1989) 149-162.
[4] J.A. Bardwell, G.I. Sproule, D.F. Mitchell, B. MacDougall, M.J. Graham, J. Chem. Soc., Faraday Trans., 87 (1991) 1011-1019.
[5] J. Gui, T. Devine, J Electrochem Soc, 138 (1991) 1376-1384.
[6] J. Gui, T. Devine, Corros Sci, 32 (1991) 1105-1124.
[7] M. Ryan, R. Newman, G. Thompson, J Electrochem Soc, 142 (1995) L177-L179.
[8] L. Freire, X.R. Novoa, M.F. Montemor, M.J. Carmezim, Mater Chem Phys, 114 (2009) 962-972.
[9] S. Joiret, M. Keddam, X.R. Novoa, M.C. Perez, C. Rangel, H. Takenouti, Cement Concrete Comp, 24 (2002) 7-15.
[10] M.F. Toney, A.J. Davenport, L.J. Oblonsky, M.P. Ryan, C.M. Vitus, Phys Rev Lett, 79 (1997) 4282-4285.
[11] E. Mccafferty, M.K. Bernett, J.S. Murday, Corros Sci, 28 (1988) 559-576.
[12] D. Thierry, D. Persson, C. Leygraf, N. Boucherit, A. Hugotlegoff, Corros Sci, 32 (1991) 273-284.
[13] P. Schmuki, S. Virtanen, A.J. Davenport, C.M. Vitus, J Electrochem Soc, 143 (1996) 574-582.
[14] S. Sharifi-Asl, F. Mao, P. Lu, B. Kursten, D.D. Macdonald, Corros Sci, (2015).
[15] Z. Lu, D.D. Macdonald, Electrochim Acta, 53 (2008) 7696-7702.
[16] R. Torresi, O. Camara, C. De Pauli, M. Giordano, Electrochim Acta, 32 (1987) 1291-1301.
[17] J.M. Bockris, J. McBreen, L. Nanis, J Electrochem Soc, 112 (1965) 1025-1031.
[18] N. Pentland, J.M. Bockris, E. Sheldon, J Electrochem Soc, 104 (1957) 182-194.
[19] J. Bao, D.D. Macdonald, J Electroanal Chem, 600 (2007) 205-216.
[20] M. Bojinov, T. Laitinen, K. Makela, T. Saario, J Electrochem Soc, 148 (2001) B243-B250.
[21] M. Büchler, P. Schmuki, H. Böhni, T. Stenberg, T. Mäntylä, J Electrochem Soc, 145 (1998) 378-385.
[22] R. Goetz, D. Mitchell, B. MacDougall, M. Graham, J Electrochem Soc, 134 (1987) 535-539.
[23] M. Nagayama, S. Kawamura, Electrochim Acta, 12 (1967) 1109-1119.
[24] N. Sato, K. Kudo, Electrochim Acta, 16 (1971) 447-462.
[25] N. Sato, T. Noda, K. Kudo, Electrochim Acta, 19 (1974) 471-475.
[26] C.Y. Chao, L.F. Lin, D.D. Macdonald, J Electrochem Soc, 129 (1982) 1874-1879.
[27] S. Sharifi-Asl, D.D. Macdonald, J Electrochem Soc, 160 (2013) H382-H391.
[28] Z.J. Lu, D.D. Macdonald, Electrochim Acta, 53 (2008) 7696-7702.
[29] Y.F. Cheng, C. Yang, J.L. Luo, Thin Solid Films, 416 (2002) 169-173.
[30] N. Hakiki, M.D.C. Belo, A. Simoes, M. Ferreira, J Electrochem Soc, 145 (1998) 3821-3829.
[31] I. Nicic, D.D. Macdonald, J Nucl Mater, 379 (2008) 54-58.

Chapter 7 The Kinetics of Nucleation of Metastable Pits on Metal Surfaces

7.1 The Kinetics of Metastable pits nucleation in terms of the PDM

This chapter aims to, for the first time, apply the theory of kinetics of nucleation of metastable pits in terms of the PDM to describing the evolution of the nucleation rate of metastable pits on metallic substrates. As reviewed in Chapter 2, the PDM proposes that the pit nucleation is due to excess vacancy condensating locally on the cation sub-lattice or on the substrate metal lattice at the m/bl interface. The detailed description of possible mechanisms for the generation of cation vacancies at the bl/s interface upon the absorption of the aggressive anion into a positively charged oxygen vacancy on the surface of the barrier layer can be found in Ref. [1]. Mathematically, the condition for the formation of a critical cation vacancy condensate (i.e., one that leads to metastable passivity breakdown) can be expressed as [2]

$$\left(J_{ca}-J_m\right)\left(t-\tau\right)\geq\xi \tag{7-1}$$

where J_{ca} is the flux of cation vacancies across the barrier layer at the breakdown site, J_m is the annihilation flux of cation vacancies, t is time, τ is the dissolution time of the cap over the vacancy condensate from the initial vacancy condensation to the point of rupture (see below; i.e., τ is the age of the blister), and ξ is the areal concentration (cm^{-2}) of condensed vacancies on the cation sublattice for the barrier layer or on the lattice of the metal substrate. Since the annihilation of cation vacancies occurs via the reaction $m+V_M^{\chi'}\rightarrow M_M+v_m+\chi e^-$ at m/bl interface, J_m depends on the self-diffusion coefficient of the metal in the substrate metal or alloy, the kinetics of the annihilation reaction, and the concentration of $V_M^{\chi'}$ at m/bl interface, which in turn depends upon the properties of the barrier layer. Accordingly, no simple correlation is expected between J_m and the self-diffusion coefficient for metal vacancies in the substrate. We further know that, for the case where no change occurs in the oxidation state of the cation that is ejected from the barrier layer at the bl/s interface, the rate constant for the annihilation reaction given above, k_1, is independent of the applied voltage, so that the annihilation flux, $J_m=k_1\left[V_{M,m/bl}^{\chi'}\right]$ is essentially constant, provided that the concentration of cation vacancies at the m/bl interface, $\left[V_{M,m/f}^{\chi'}\right]$, is not a strong function of voltage [3]. Noting that J_{ca} is potential-dependent [see later in Eqs. (7-8) and (7-9)], and that J_m is not strongly potential-dependent, the passivity breakdown potential corresponds to that at which passivity breakdown takes over infinite time to occur (i.e. when $J_{ca}=J_m$). This condition further leads to the expressions for the passivity breakdown potential , V_b, at a single site on the metal surface as [2]:

$$V_b = \frac{4.606RT}{\chi\alpha F}\log\left[\frac{\lambda}{D}\right] - \frac{2.303RT}{\alpha F}\log a_{X^-} \tag{7-2}$$

where

$$\lambda = \frac{RTJ_m\Omega}{F\chi\varepsilon N_A}\exp\left[\frac{\Delta G_S^o + (\chi/2)\Delta G_A^o - (\chi/2)\beta F\mathrm{pH} - (\chi/2)F\phi_{f/s}^0}{RT}\right] \tag{7-3}$$

In the above equations, α is the polarizability of the barrier layer/solution interface (i.e., the dependence of the potential drop across the bl/s interface on the applied potential). N_A is Avogadro's number, χ is the oxidation state of the host cation within the barrier layer, F is Faraday's constant, a_{X^-} is the activity of the aggressive anion X^- (e.g. Cl^-) in the aqueous solution, D is the cation vacancy diffusivity, ε is the electric field strength within the barrier layer, Ω is the molar volume of the barrier layer oxide per cation, ΔG_S^0 is the standard Gibbs free energy change for the Schottky-pair reaction (generation of cation vacancies and oxygen vacancies) or is the change in standard Gibbs free energy for cation extraction, ΔG_A^0 is the standard Gibbs free energy change for the chloride/oxygen vacancy absorption reaction, β is the dependence of the potential drop across the film/solution (f/s) interface on pH, and $\phi_{f/s}^0$ is a constant.

At this point, it is of great importance to clarify and stress that the kinetic model and all of its equations presented in this section strictly apply to passivity breakdown and, hence, to the nucleation of a metastable pit. In this and other analyses, V_b is taken to be the potential at which a stable pit nucleates, because in a typical potentiodynamic experiment, as the potential is swept in the positive direction, metastable transients are observed prior to the potential at which the current suddenly increases due to the nucleation of a stable pit. However, Eq. (7-1) and hence Eq. (7-2) strictly apply to passivity breakdown and, hence, to the nucleation of a metastable pit, so that the application of Eq. (2) to stable pitting potentials, as determined potentiodynamically, would be expected to yield differences in the values derived for parameters contained therein from their "true" values. We do not regard this to be a particularly serious issue, because, as shown below in Section 7.3, parameter values obtained by optimizing the PDM on unequivocally-demonstrated meta-stable pitting nucleation rate data predict V_b quite successfully. Furthermore, the functional form of Eq. (7-2) has been demonstrated almost without exception when the potential for stable pitting, as defined above for potentiodynamic conditions, has been determined as a function of $[Cl^-]$ and pH. Other members of the group is in progress developing a theory and model for calculating the "survival probability" of a passivity breakdown event that yields a stable pit, which intends to correlate the present model for metastable pits nucleation to formation of stable pits.

An energy term, w, is defined [Eq. (7-4)] to describe the energy related to the absorption of aggressive anions into oxygen vacancies [4]. A more negative value of w means a more energetically-favorable absorption process.

$$w = \frac{\chi}{2}\Delta G_A^o + \Delta G_S^o - \frac{\chi}{2}F\phi_{f/s}^0 \tag{7-4}$$

Moreover, τ, the dissolution time, which is the time taken for the cap over the vacancy condensate to become sufficiently thin to rupture from the point of initial cation vacancy condensation, can be defined as:

$$\tau \le L_{ss}/(\mathrm{d}L/\mathrm{d}t)_{\text{dissolution}} = L_{ss}/\Omega k_7 \left(C_H/C_H^o\right)^n \tag{7-5}$$

where L_{ss} is the steady-state thickness of the barrier layer at the voltage at which cation vacancy condensation just begins; k_7 and n are the rate constant and reaction order of the dissolution reaction of the barrier layer with respect to H^+, respectively, with the latter commonly being assumed to be 0.5; C_H and C_H^0 are, respectively, the concentration and standard state concentration of the hydrogen ions at bl/s interface. These parameters are derived within the PDM, as described in Ref. [5].

On any real metal surface, there is a large number density of potential breakdown sites with "weak points" being distributed, as described above. Thus, the distribution of the breakdown sites, as represented by the diffusivity of cation vacancies, is assumed in the PDM to follow a normal distribution function:

$$\frac{\mathrm{d}N(D)}{\mathrm{d}D} = -A\exp\left[-\frac{(D-\overline{D})^2}{2\sigma_{\mathrm{D}}^2}\right] \tag{7-6}$$

where $N(D)$ is the number of breakdown sites (cm^{-2}) that have diffusivities larger than D; $\overline{D}$ and $\boldsymbol{\sigma_D}$ are, respectively, the mean and standard deviation of the cation vacancy diffusivity for a single population of the breakdown sites on the metal surface; A is a parameter that does not depend on D and is defined below [see Eq. (7-14)]. The normalization of Eq. (7-6) using the condition $N(0) = N_0$ as $t \to \infty$, where N_0 is the total number density of potential breakdown sites (cm^{-2}), gives the number of breakdown sites for a given value of D [6]:

$$N(D) = N_0 \,\mathrm{erfc}\left(\frac{D-\overline{D}}{\sqrt{2}\sigma_D}\right) / \,\mathrm{erfc}\left(-\frac{\overline{D}}{\sqrt{2}\sigma_D}\right) \tag{7-7}$$

Because transportation of cation vacancies across the barrier layer from the bl/s interface to the m/bl interface mainly proceeds via electro-migration (because of the high electric field strength), the cation vacancy flux density, J_{ca}, should be proportional to D and the electric field:

$$J_{ca} = D\,B, \tag{7-8}$$

where B is a function depending on the electric field strength within the film, ε, and on the external conditions (e.g. applied voltage, V_{app}, temperature, T, aggressive anions activity, a_{X^-}, etc.):

$$B = \frac{\chi F \varepsilon N_A a_X^{\chi/2}}{\Omega RT} \exp\left[\frac{\chi F(\beta \mathrm{pH} + \alpha V_{app}) - 2w}{2RT}\right] \tag{7-9}$$

The criterion for metastable pit nucleation can then be obtained by substituting Eq. (8) into Eq. (7-1) to yield:

$$D \geq D_{\text{critical}} = \frac{\xi + J_m(t-\tau)}{B(t-\tau)} \tag{7-10}$$

Criterion (7-10) dictates that the nucleation of metastable pits on metal surfaces occurs within the observation time, *t,* on those and only on those sites that have vacancy diffusivity being equal to or greater than a critical diffusivity value, D_{critical}. Combining Eq. (7-7) and (7-10) we then can obtain the integral number of the metastable pitting events within time *t* as:

$$N(t) = N_0 \ \mathrm{erfc}\left(\frac{a}{t - \tau} + b\right) / \mathrm{erfc}(b) \tag{7-11}$$

where

$$a = \frac{\xi}{\sqrt{2}\sigma_D B} \tag{7-12}$$

$$b = \frac{J_m}{\sqrt{2}\sigma_D B} - \frac{\overline{D}}{\sqrt{2}\sigma_D} \tag{7-13}$$

The parameter A in Eq. (7-6) is defined as:

$$A = \frac{N_0}{\sqrt{\pi}\ \mathrm{erfc}(b)} \tag{7-14}$$

Finally, the rate of metastable pit nucleation is obtained by taking the derivative of $N(t)$ in Eq. (7-11) with respect to t:

$$n(t) = \frac{\mathrm{d}\,N}{\mathrm{d}\,t} = \frac{N_0\,2a}{\mathrm{erfc}(b)\sqrt{\pi}} \frac{\exp\left[-\left(\frac{a}{t-\tau} + b\right)^2\right]}{(t-\tau)^2} \tag{7-15}$$

It must be noted that, from Eq. (), the maximum nucleation rate of metastable pits should be observed at:

$$t_{max} = \tau + a(b + \sqrt{b^2 + 4})/2 \tag{7-16}$$

Accordingly, if t satisfies the condition

$$t >> t_{max} \tag{7-17}$$

then, practically, all of the metastable pits will nucleate within a very short period of time at the beginning of the observation time (i.e. the number of pits grows at a maximum rate shortly after the first pit appears). It has been found [7, 8] that, under some conditions (especially where concentrations of Cl^- or the potential is high), criterion (7-17) holds very well and the nucleation of metastable pits on a metal surface may be regarded as being an "instantaneous nucleation" phenomenon. Nevertheless, t_{max} increases dramatically as the chloride concentration decreases, as exemplified in Figure 7-1, giving rise to a "progressive nucleation and growth/death scenario" where new pits nucleate on the metal surface as existing pits grow and die. These two different patterns in observations of metastable pitting will be demonstrated by the selected data in the next section of the paper.

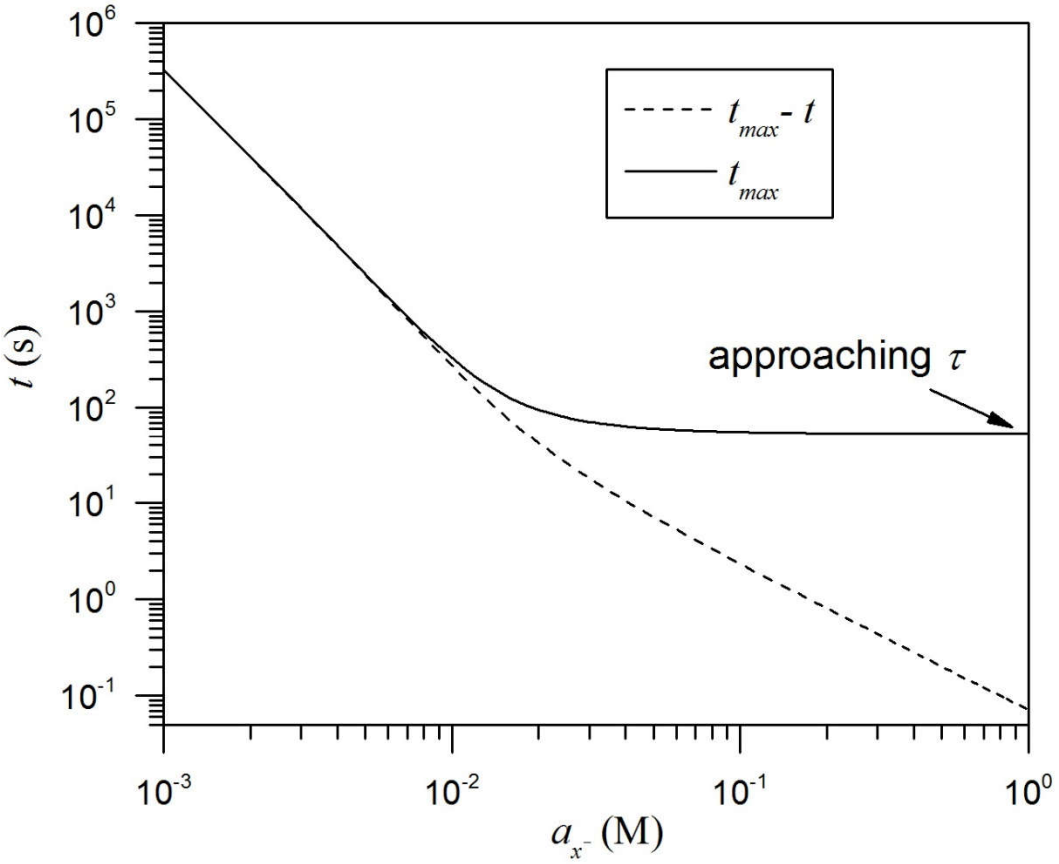

Figure 7-1: Example of the effect of activity of X^- on the time when the nucleation rate of metastable pits maximum. Based on the parameter values reported for Set III in Table 7-3.

7.2 Optimization On the Metastable Pit Nucleation Data

The PDM, for the nucleation of metastable pits described above, has been tested by the optimization of the model on experimentally-determined metastable pit nucleation rate vs. time by using Eq. (7-15) and on experimentally-determined data for the integral number of metastable pits vs. time by using Eq. (7-11). Software IGOR Pro was utilized to conduct the optimization via its feature of curve fitting by least squares. In order to demonstrate the validity of the model over a broad scope of micro-structural features, six sets of data (assigned as Set I-VI, with details listed in Table 7-1) collected on a variety of metallic materials, including stainless steel [9, 10], carbon steel [11], pure iron [12], pure aluminum [13], and Alloy-22 [14] have been extracted from the literature. Sets I-III are data of evolution of the nucleation rate of metastable pits, while Set IV-VI are data of evolution of cumulative number of metastable pitting events. All data sets were acquired at ambient temperature, except Set VI which was acquired at 80 °C. Parameters that were held constant during the optimization are listed in Table 7-2, which also includes the sources of the values [15, 16]. The oxidation state of host cation within the barrier layer, χ, is chosen as +3 for all cases, assuming the composition of the barrier layer on Type 304 SS (and Alloy-22), carbon steel (iron), and aluminum is primarily point-defective Cr_2O_3, Fe_2O_3, and Al_2O_3, respectively, and the mean diffusivity of all the three cation vacancy species ($V_{Cr}^{3\prime}$, $V_{Fe}^{3\prime}$, $V_{Al}^{3\prime}$) is assumed as being 5×10^{-19} cm^2 s^{-1} [17]. The standard deviation of the diffusivity was chosen from $0.25\overline{D}$, $0.5\overline{D}$ and $0.75\overline{D}$ based on which one of the three yields better fitting. The parameter values obtained from the optimization on all six data sets are compiled in Table 7-3.

Table 7-1: The details of the metastable pitting experiments from which the six sets of selected data were extracted.

	Materials (wt %)	**Test Solutions**	**Voltages**
Set I [10]	Type 304 SS (Cr 17.9, Ni 10.4, Mn 0.8, Si 0.4)	0.8 M NaCl + 0.2 M HCl, pH = 0.7	0.1 V_{SCE}
Set II [9]	Type 304 SS (Cr 18.3, Ni 8.5, Mn 0.8, Si 0.3)	0.1 M HCl, pH = 1	0.2 V_{SCE}
Set III [11]	A516-70 CS (C 0.31, Mn 1.0, P 0.035, S 0.04, Si 0.25)	0.5 M $NaHCO_3$ + 0.01 M NaCl, pH = 8.3	0.05 $V_{Ag/AgCl}$
Set IV [12]	Pure iron (Fe 99.98)	0.5 M borate buffer + 0.1 M Cl^-, pH = 7.5	0.1 V_{SCE}
Set V [13]	High purity aluminum (Al 99.999)	deionized water + 0.001 M NaCl; pH ≈ 7*	-0.5 V_{SCE}
Set VI [14]	Alloy-22 (Ni 57.28, Cr 21.55, Mo 13.05, Co 1.07, Fe, 3.83)	5 M LiCl + 0.26 M Na_2SO_4 + 0.24 M $NaNO_3$ + 0.2 mM HCl (pH = 2.75), 80 °C	-0.025 $V_{Ag/AgCl}$

*Actual pH not given in the original work, which could be less than 7 due to dissolved CO_2.

Table 7-2: The parameters that are held constant during the optimization of the PDM on the nucleation rate data acquired on Type 304SS [9, 10], carbon steel [11], iron [12], aluminum [13], and Alloy-22 [14].

Parameters	Values	Units	Sources
χ, the oxidation state of host cation within barrier layer (Cr_2O_3/Fe_2O_3/Al_2O_3)	+3		Assigned
n, reaction order of the dissolution of the barrier layer	0.5		Assumed
ε, the electric field strength within bl	3×10^{6}	V cm^{-1}	Assumed
α, the polarizability of the film/solution interface	0.15		[16]
β, dependence of the potential drop across film/solution interface on pH	-0.01	V	[15]
Ω, molar volume of oxide per cation	14.59 (Cr_2O_3) 15.27 (Fe_2O_3) 12.91 (Al_2O_3)	cm^3 mol^{-1}	From density
$\bar{D}$, the mean diffusivity of cation vacancy	5×10^{-19}	cm^2 s^{-1}	[16]
$\phi^0_{f/s}$, potential drop at the film/solution interface for V_{app}= 0, and pH=0	-0.1	V	Assumed

Table 7-3: The parameter values obtained from optimization of the PDM on metastable pits on all the six sets of data taken form the literature [9-14].

Parameters	Values					
	Set I-304SS	**Set II-304SS**	**Set III-CS**	**Set IV-Pure Fe**	**Set V-Pure Al**	**Set VI-Alloy-22**
N_0, the total number of breakdown sites per area, cm^{-2}	2.67×10^{6}	5.72×10^{5}	387	598	3.12×10^{4}	14.9
τ, the dissolution time, s	37.6	214.5	53.3	$4.82+t_{ind}$	57.8	29.7
ξ, the critical areal concentration of cation vacancies, cm^{-2}	4.61×10^{14}	4.60×10^{14}	3.10×10^{14}	2.97×10^{14}	4.27×10^{14}	4.23×10^{14}
w, the energy related to the absorption of X^- into a surface oxygen vacancy, J mol^{-1}	-790	-3,339	-14,324	-16,742	-44,575	-4,264
J_m, the annihilation flux of the cation vacancies at the breakdown site, $cm^{-2}\ s^{-1}$	2.97×10^{13}	2.36×10^{12}	8.34×10^{12}	3.47×10^{12}	4.91×10^{13}	4.02×10^{14}
J_{ca}, the flux of the cation vacancies across the barrier layer, $cm^{-2}\ s^{-1}$	3.36×10^{13}	3.00×10^{12}	8.57×10^{12}	4.59×10^{12}	6.05×10^{13}	5.37×10^{14}
$(J_{ca}-J_m)$, the condensation rate of cation vacancies at the break down site, $cm^{-2}\ s^{-1}$	3.90×10^{12}	6.40×10^{11}	2.30×10^{11}	1.12×10^{12}	1.14×10^{13}	1.35×10^{14}
t_{max}, the time at which the nucleation rate of metastable pits is maximum, s	101.5	365.9	327.8	-	-	-
σ_D, the standard deviation of cation vacancy diffusivity, $cm^2\ s^{-1}$	$0.25\overline{D}$	$0.50\overline{D}$	$0.75\overline{D}$	$0.25\overline{D}$	$0.75\overline{D}$	$0.25\overline{D}$

7.2.1 Metastable Pitting On Stainless Steel

Two sets of nucleation rate data on stainless steel were taken from the work of Burstein and colleagues [9, 10], both of which were acquired on Type 304SS, but with slight differences in experimental conditions (Table 7-1). Very good agreement was obtained for both sets between the experimental and fitted nucleation rate as a function of time.

For Set I, the total number of available breakdown sites per unit area, N_0, is obtained as being equal to 2.67×10^6 cm^{-2}, a value almost the same as that reported by Pistorius and Burstein [10] (approx. 2.65×10^6 cm^{-2}), which was calculated by employing a first-order kinetics method. The critical areal concentration of cation vacancies to initiate the metastable pit, ξ, is found from the optimization to be 4.61×10^{14} cm^{-2}. Alternatively, as has been performed in previous work [16, 18, 19], ξ can be calculated from the relationship between the $V_b(v)$ and $v^{1/2}$, where $V_b(v)$ is the critical pitting potential determined potentiodynamically and v is the potential sweep rate that is selected to determine $V_b(v)$ potentiodynamically (see later in Section 8.2). By employing this method, Zhang et al. [18] found that, for Type 403SS in chloride containing borate buffer solutions (pH = 8.1), ξ is less than or equal to 7×10^{14} cm^{-2}, a value that agrees well with that obtained in the present work. Furthermore, the unit cell dimensions of the barrier layer and/or the base metal can also be used to estimate the value of ξ. The barrier layer (Cr_2O_3) has a rhombohedral unit cell with $a = 0.4959$ nm and $c = 1.360$ nm [20], and thus the density of Cr atoms per unit area in a monolayer of the unit cell of the barrier layer is calculated to be $\sim10^{14}$ cm^{-2}, which matches closely with the result above. The approximation to an order of magnitude is used here because different crystal planes in a unit cell of polycrystalline material have different atom densities.

The energy term w can be obtained from the optimization and its value for Set I is the least negative among all data sets, indicating that it is more energetically difficult to generate Schottky vacancies and to absorb Cl^- into oxygen vacancies at the bl/s interface on SS than for a more negative value of w (i.e. carbon steel, Fe, Al and Alloy-22). Note that the values of w, along with ΔG_A^0 and ΔG_S^0, are not able to be verified unequivocally, at least at this time, due to the paucity of independent, relevant data in the literature (either experimentally measured or calculated by first principle theory). However, the values of w obtained in this work for all data sets lie between 0.79 kJ/mol and 44.58 kJ/mol, which is a physically reasonable range. The "cap" dissolution time, τ, is found to be quite short for Set I, 37.6 s, indicating that the vacancy condensation occurring between the stainless steel substrate and the film "cap" is a rather rapid process. Furthermore, Eq. (7-5) indicates a dissolution rate of about 0.1 nm/s, which appears to be reasonable for the stated conditions.

The fitted curve of Set I (Figure 7-2) shows that the maximum pit nucleation rate is reached at $t_{max} = 101.5$ s [Eq. (7-16)], a point subsequent to the initial observation time, 75 s, leading to a peak in the nucleation rate curve. In contrast, such peak is absent in the results for Set II (Figure 7-3), where an "instantaneous nucleation" pattern is observed, because the first observation time, $t = 370$ s, was after the time at which the nucleation rate of metastable pits maximized, $t_{max} = 365.9$ s (not shown in the figure). The larger t_{max} for Set II is possibly attributed to the lower concentration of Cl^- adopted than for Set I (0.1 M < 1 M), which gives rise to a lower flux of cation vacancies across the barrier layer, J_{ca}, and a lower vacancy condensation rate [The value of $(J_{ca} - J_m)$ for Set I is about six times larger than that for Set II]. Additionally, the cation vacancy diffusivity for Set I has a narrower distribution than that for Set II ($\sigma_D = 0.25\,\overline{D}$ and $0.50\overline{D}$, respectively), which is consistent with the previous finding [18] that increasing chloride activity

not only makes the mean breakdown potential more active (negative) but also narrows the distribution in the breakdown potential. Finally, the optimization results of ξ and w for Sets I and II are found to be very close, probably because these parameters are characteristics of the barrier layer formed on Type 304SS that was used in both studies.

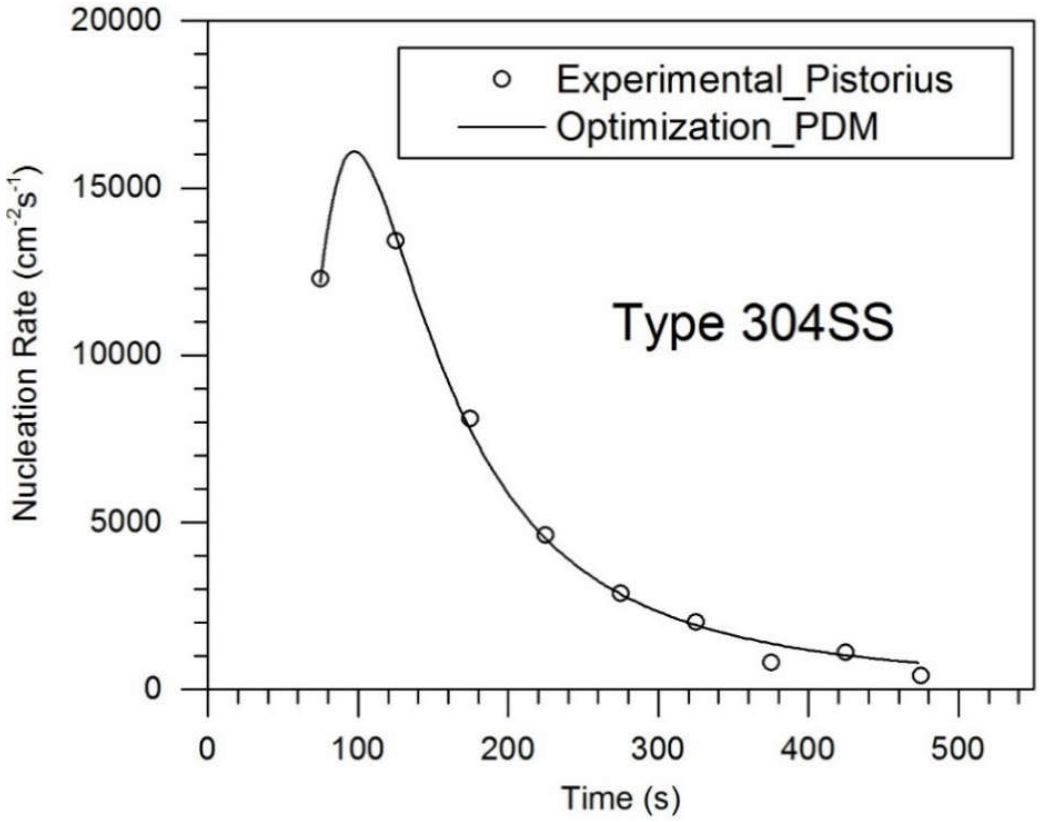

Figure 7-2: The experimentally measured nucleation rate of metastable pits as a function of time taken from Pistorius and Burstein [8] (Set I, Table 7-2) and the optimization results of the PDM on the data via Eq. (7-15).

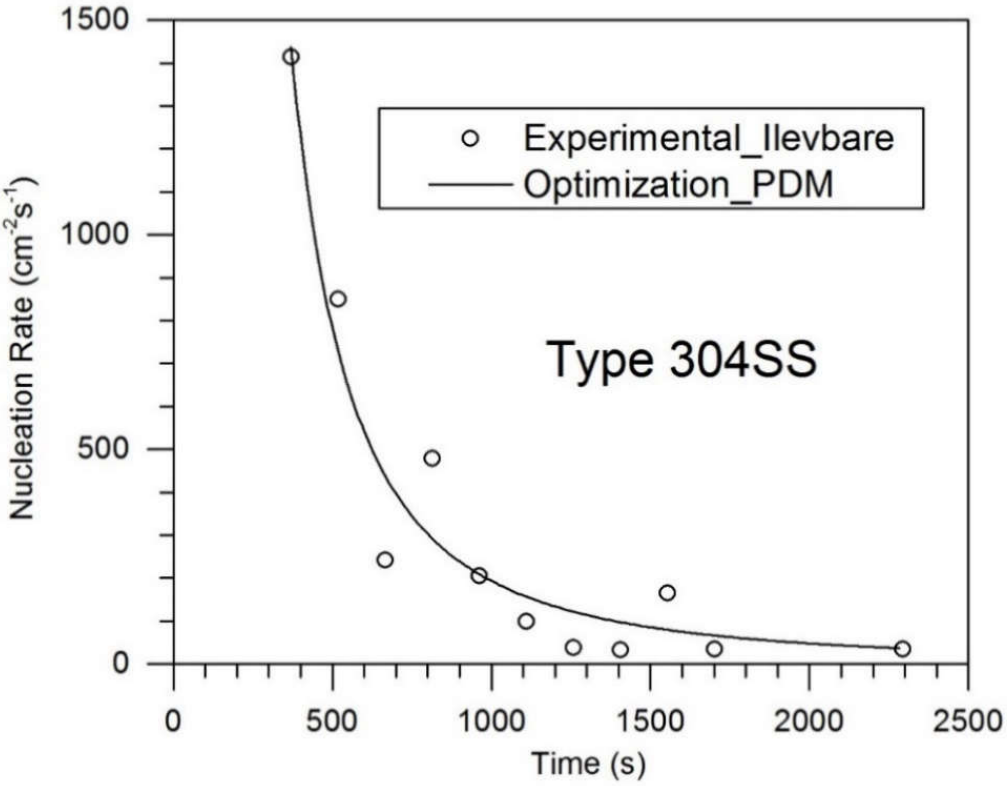

Figure 7-3: The experimentally measured nucleation rate of metastable pits as a function of time taken from Ilevbare and Burstein [9] (Set II, Table 7-2) and the optimization results of the PDM on the data via Eq. (7-15).

7.2.2 Metastable Pitting On Carbon Steel

Figure 7-4 displays the nucleation rate data of metastable pits on carbon steel (CS) in neutral solutions (Set III) taken from Cheng and Luo's work [11] and the curve fitted via the PDM. Again, Eq. (7-15) was used to conduct the optimization and a good match between the experimental and fitted data was obtained, where a nucleation rate peak (t_{max} = 327.8 s) similar to that in Set I is observed. The optimization result of N_0 (387 cm^{-2}) agrees well with that reported in the original work (~371 cm^{-2}). Note the value of N_0 for Set III is significantly smaller (by 3~4 orders) than those on Set I and II, a discrepancy that, presumably, is determined by differences in the microstructure that determines the surface concentration of potential breakdown sites. For the same reason, Set II has a smaller N_0 than Set I. However, Reuter and Heuler [12] found that N_0 decreases on a logarithmic scale with increasing pH and decreasing [Cl$^-$], but it is not clear that their experiments satisfied the infinite time condition for the determination of N_0 [see Eq. (7-7)]; that is, there may exist a large population of potential breakdown sites that did not activate, because they were characterized by cation vacancy diffusivities that were smaller than those corresponding to the maximum experimental time. Alternatively, the markedly smaller N_0 for CS may result

from a metallurgical aspect that the matrix of CS, a low-alloy steel, usually has more uniform phase distribution and less inhomogeneous defects (e.g. second phase particles, inclusions, and precipitations) that function as preferential pitting initiation sites than do the more-highly alloyed stainless steels. Raising (more positive) applied voltage also has the effect of increasing J_{ca} (via increasing B) and activating more potential breakdown sites, but since Set I-IV have more-or-less the same V_{app} (Table 7-2), the voltage cannot be the source of the notable difference in N_0 observed in this case. The surface finish of the specimens used for Set I-III is also similar (1200-grit for Set I, II; 1000-grit for Set III), thus the influence of the surface roughness on N_0 can be excluded, as well. The energy term w for Set III is found to be about one order of magnitude more negative than those for Sets I and II, implying that the vacancies generation and the ensuing Cl^- absorption into oxygen vacancies at the bl/s interface on CS occur more readily than on SS, which is closely related to the observed more active breakdown potential of CS than that of SS. Lastly, the value of ξ for Set III is somewhat smaller than those for Sets I and II, which is possibly due to the larger lattice parameter of Fe_2O_3 (the composition of barrier layer on CS) than that of Cr_2O_3 (the composition of barrier layer on SS).

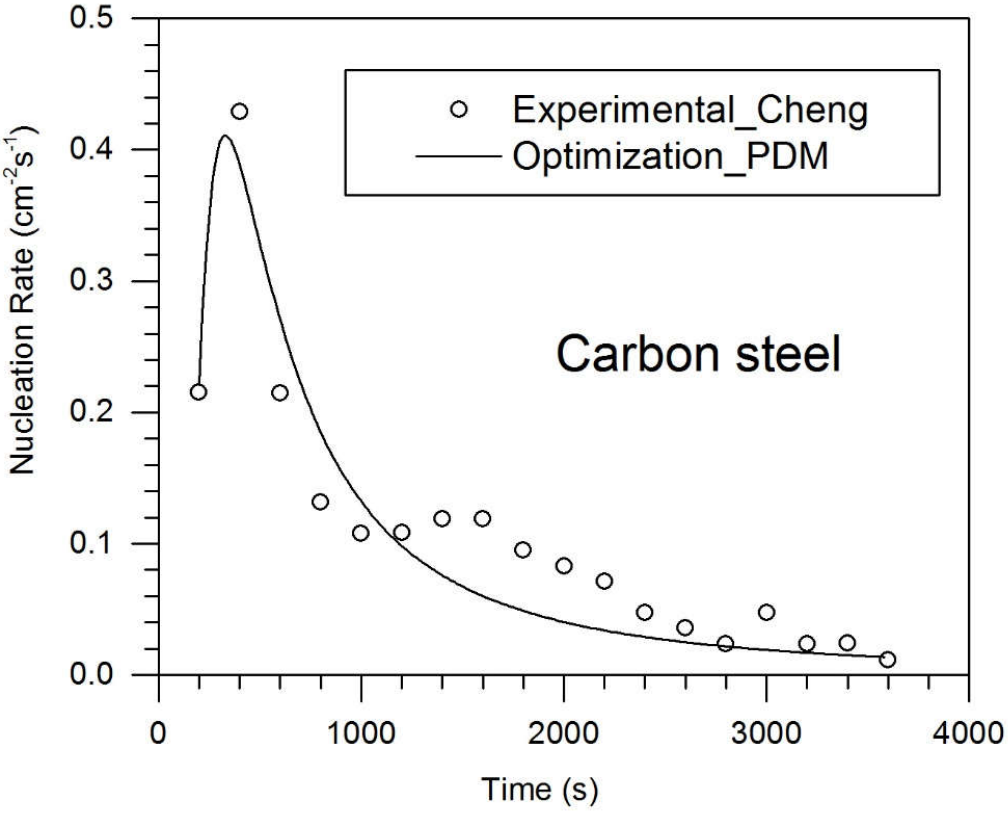

Figure 7-4: The experimentally measured nucleation rate of metastable pits as a function of time taken from Cheng and Luo [11] (Set III, Table 7-2) and the optimization results of the PDM on the data via Eq. (7-15).

7.2.3 Metastable Pitting On Passive Iron

Reuter and Heusler's work [12] on pitting of passive iron was selected for the optimization. Figure 7-5 shows their data of cumulative surface concentration of pits as a function of time (Set IV) and the fitted curve via Eq. (7-11). Note that the stable and metastable pits were not differentiated in the original study, but, as demonstrated by Williams et al. [21], the number of metastable pits is proportional to the number of stable pits, and thus by using the total surface concentration of pits as the areal number of metastable pitting events does not affect the optimization results (but would shift the scale). It is evident from Figure 7-5 that $N(t)$, after a characteristic time, reaches a constant value that corresponds to the total available sites for metastable pitting, N_0. Because CS is predominantly composed of iron, CS and pure iron have comparable chemical properties and corrosion behaviors and hence Set III and IV have fairly close values of ξ and w, which are material characteristics. The higher [Cl^-] and lower pH employed in Set IV than in Set III renders the former with a higher $(J_{ca} - J_m)$ and a smaller σ_D than in Set III, as demonstrated above. Note that the absolute value of dissolution time τ is not able to be acquired by optimization in this case, because the time scale of the data reported in the original work starts from the moment when the first pit appears rather than from the beginning of the experiment. Thus, with the induction time t_{ind} being unknown, τ can only be obtained relatively as a time subsequent to t_{ind}, which equals to 4.28 s + t_{ind}.

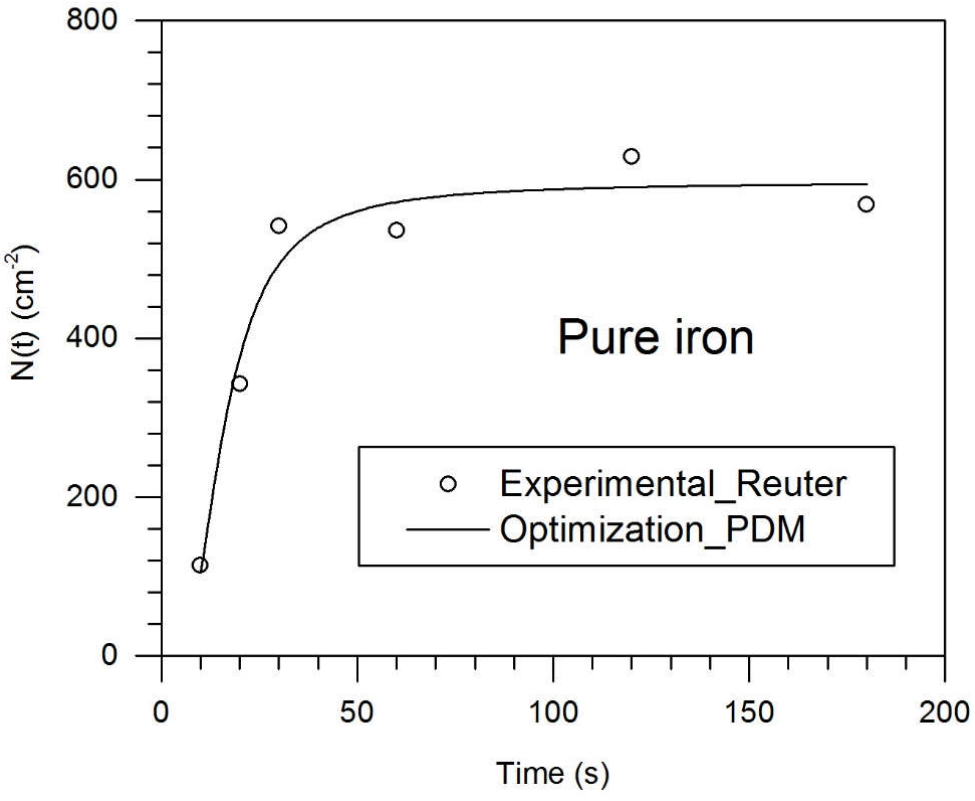

Figure 7-5: The experimentally measured total metastable pitting events on passive iron as a function of time taken from Reuter and Heusler [12] (Set IV, Table 7-2) and the optimization results of the PDM on the data via Eq. (7-11).

7.2.4 Metastable Pitting On Aluminum

Pride et al.'s data of metastable pitting on pure aluminum [13] were extracted. Eq. (7-11) was again employed successfully to fit the experimentally-obtained data of $N(t)$, versus time as shown in Figure 7-6. It is to be noted that fitting of the model to the data at small t values (shorter times) is not as good as that at larger t values (longer times), which is possibly due to issues with the original data set, which are beyond our control. On the other hand, the problem might be attributable to the fact that, when optimizing the theory on the data using least-square method, in order to obtain the smallest global chi-square (sum of the squares of the errors), the fitting program puts higher priority on matching the points with large values (i.e. data at longer times), which tend to generate large errors in magnitude, compared with data at shorter times with much smaller values. The optimization results presented in Figure 7-6 correspond to the minimum chi-square that can be obtained given by all of the available data.

The very negative value of the energy term w obtained for aluminum is noteworthy, and in spite of the relatively benign condition with a modest [Cl^-] of 0.001 M and a neutral pH, the condensation rate of vacancy on aluminum/barrier layer interface is found to be considerable (about one order larger than those of the other five sets). The value of N_0 is also large, considering that the aluminum specimen was of high purity (99.999 %). Nevertheless, both the values of $(J_{ca} - J_m)$ and N_0 could be ascribed to the substantial anodic overpotential applied to aluminum in the experiment (~0.8 V). All of the results discussed above on Al are associated with the very active open circuit potential and active critical breakdown potential observed on pure Al compared with those of CS and SS in neutral solutions with similar [Cl^-].

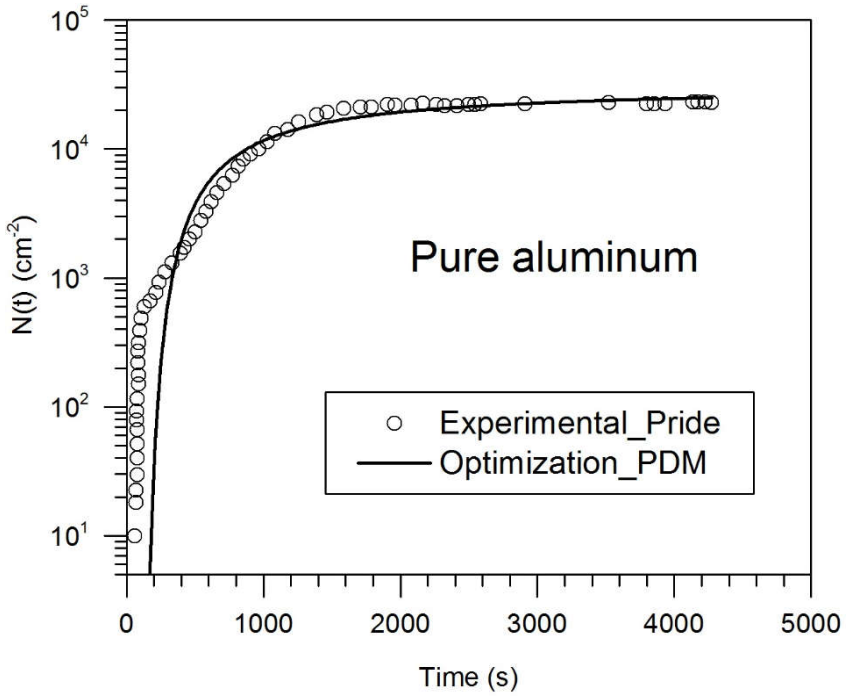

Figure 7-6: The experimentally measured total metastable pitting events on pure aluminum as a function of time taken from Pride et al. [13] (Set V, Table 7-2) and the optimization results of the PDM on the data via Eq. (7-11).

7.2.5 Metastable Pitting in Crevices on Alloy-22

Metastable pitting data obtained by Kehler and Scully [14] in crevices on Alloy-22 have been extracted to examine the effectiveness of the PDM to account for observations of metastable pitting made on higher-alloyed materials. It has been demonstrated previously [22-24] that the PDM can readily interpret passivity observations on Alloy-22. Characterization work [22, 25-27] has demonstrated that the passive film on Alloy-22 has a distinct layered structure with the inner layer primarily comprising Cr(III) oxide, so it is assumed in the optimization that Cr_2O_3 is the principal composition of the barrier layer. Figure 7-7 shows that the experimental data of $N(t)$ on Alloy-22 can be successfully reproduced by optimization using Eq. (7-11). It can be found from the optimization results that Alloy-22 has the largest value of J_m among the selected materials, indicating that the m/bl interface on Alloy-22 possesses a strong capability of annihilating cation vacancies to deter vacancy condensation. This finding, together with the remarkably small value of N_0, is tightly related to the excellent localized-corrosion resistance of Alloy-22 [28, 29]. It needs to be noted that the value of J_{ca} for Alloy-22 is also the largest among all of the data sets, which, recalling Eq. (7-18), is a result primarily resulting from the much more aggressive experimental conditions employed in Set VI (5 M [Cl^-], low pH, and high temperature).

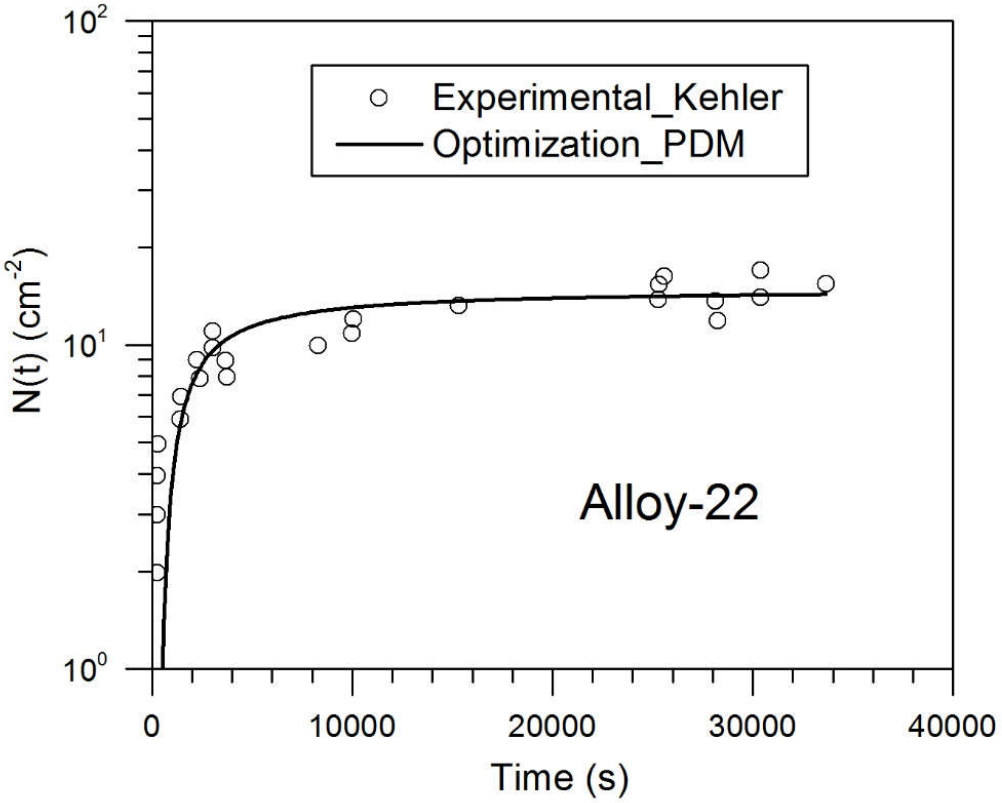

Figure 7-7: The experimentally measured total metastable pitting events on Alloy-22 as a function of time taken from Kehler and Scully [14] (Set VI, Table 7-2) and the optimization results of the PDM on the data via Eq. (7-11).

7.3 Sensitivity Analysis

One of the ultimate goals of the project supporting the current work is to predict the values of the parameters reported above in a completely *ab initio* approach. In order to achieve this in an orderly manner, sensitivity analysis has been conducted to prioritize the parameters with regard to their impact on metastable pit nucleation. In general, the sensitivity analysis was done by inputting parameter values different to those reported in Table 7-3 (the "true" values) into the model and then observing how significantly a certain deviation of one parameter from its "true" value affects the final metastable pit nucleation results. More pronounced the influence is, more sensitive the metastable pit nucleation is to this parameter, and vice versa. The experimental data employed here are the integral number of metastable pit nucleation events, $N(t)$, on pure aluminum (Set IV, Table 7-1) [13]. Several parameters in Table 7-3 were picked out for the sensitivity analysis, namely, w, σ_D, $\overline{D}$, J_m, and τ. Since $J_m = k_1\left[V_{M,m/bl}^{\chi'}\right]$, and k_1 is further dependent on α, β, k_1^0, and α_1, as defined in Table 2-3, a total of eight parameters are eventually included in the analysis (i.e. α, β, k_1^0, α_1, w, σ_D, $\overline{D}$, and τ).

The results of the sensitivity analysis are presented in Figure 7-8 to Figure 7-15. These figures demonstrate that a mere 10% change in w can lead to a noticeable shift in $N(t)$ result, however, in order to yield a similar amount of displacement, it takes changes of approximately 40% for β, 60% for α, 500% for σ_D, 1000% for $\overline{D}$, and 2000% for k_1^0, respectively. No obvious variation in $N(t)$ result was observed by adjusting the values of α_1 and τ. Based on the change that is required for each parameter to induce a certain change in $N(t)$, the fraction of contribution of those parameters to the final value of $N(t)$ was calculated and is ranked in Table 7-4. The result shows that the sensitivity of $N(t)$ to the parameters follows the decreasing order of $w > \beta > \alpha > \sigma_D > \overline{D} > k_1^0 > \alpha_1 > \tau$. From this we can conclude that the greatest need for achieving an *ab initio* prediction of passivity breakdown lies in calculating the parameters in the above order.

Table 7-4: Fraction of contribution of prominent independent parameters in the PDM to $N(t)$, listed in the order of decreasing contribution.

Parameters	Fraction of contribution to $N(t)$
w	63.21 %
β	14.53 %
α	7.97 %
$\overline{D}$	7.07 %
σ_D	6.98 %
k_1^0	0.24 %
α_1	<0.01 %
τ	<0.01 %

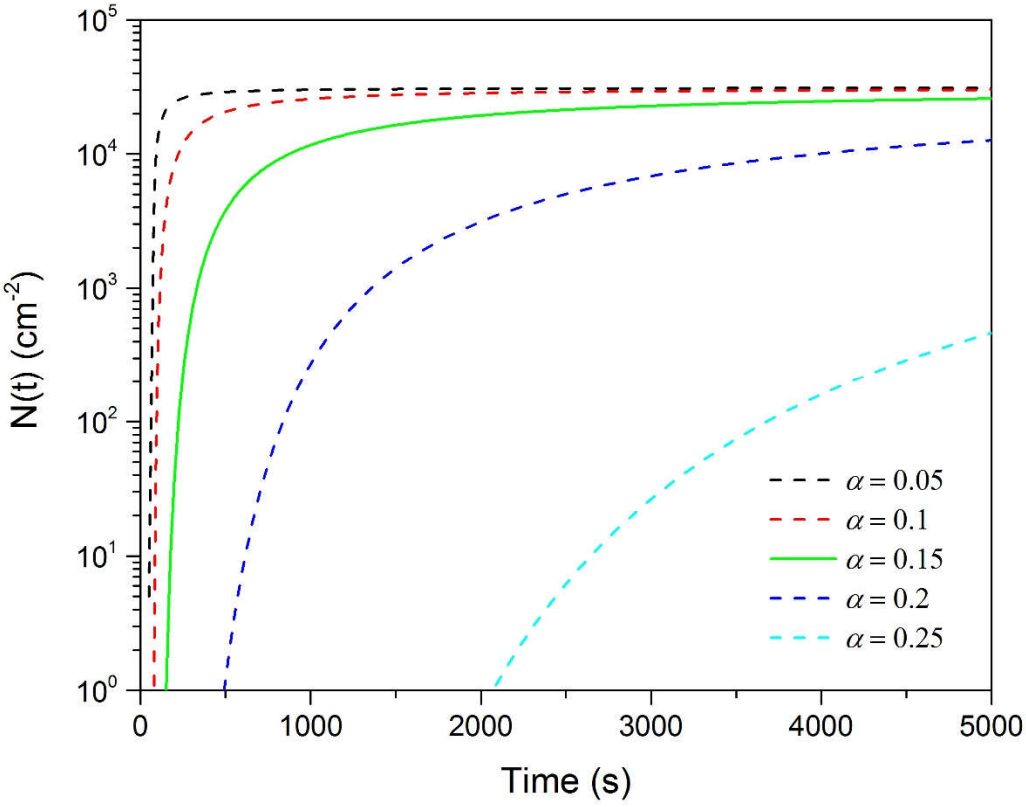

Figure 7-8: Different calculated $N(t)$ results from changing the value of the polarizability of the barrier layer/solution interface, α. The solid line represents the result obtained by optimization on the actual experimental $N(t)$ data, whereas the dash lines represent the results by manipulating α for sensitivity analysis.

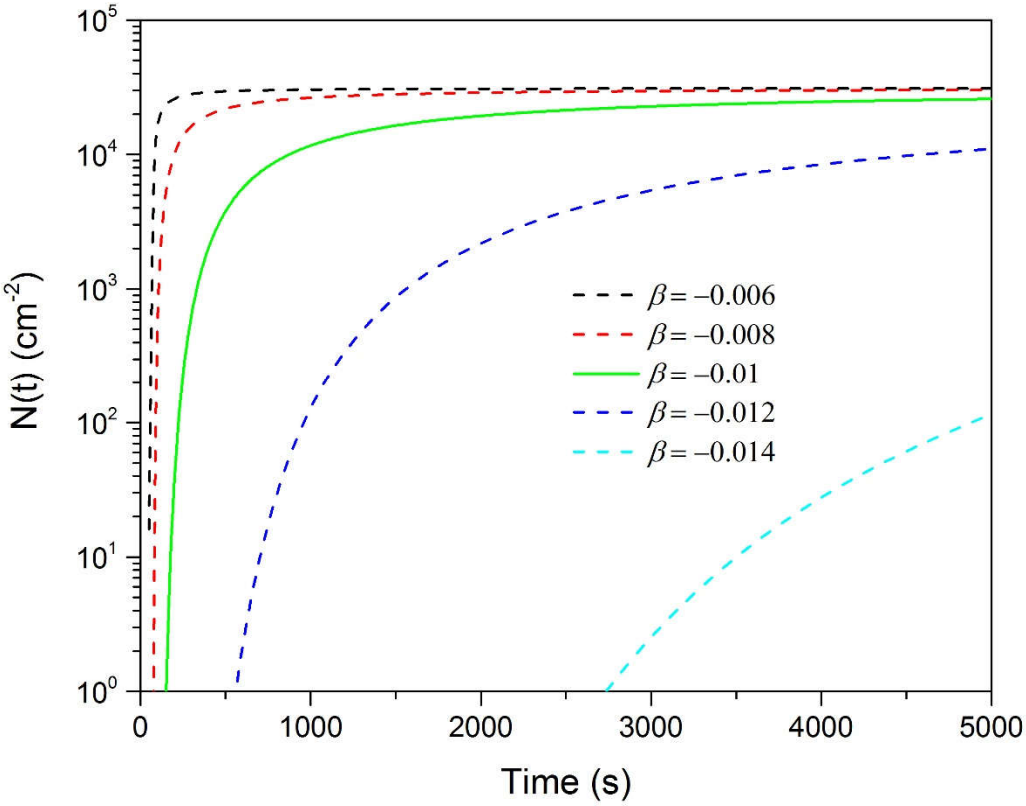

Figure 7-9: Different calculated $N(t)$ results from changing the value of dependence of the potential drop across barrier layer/solution interface on pH, β. The solid line represents the result obtained by optimization on the actual experimental $N(t)$ data, whereas the dash lines represent the results by manipulating β for sensitivity analysis.

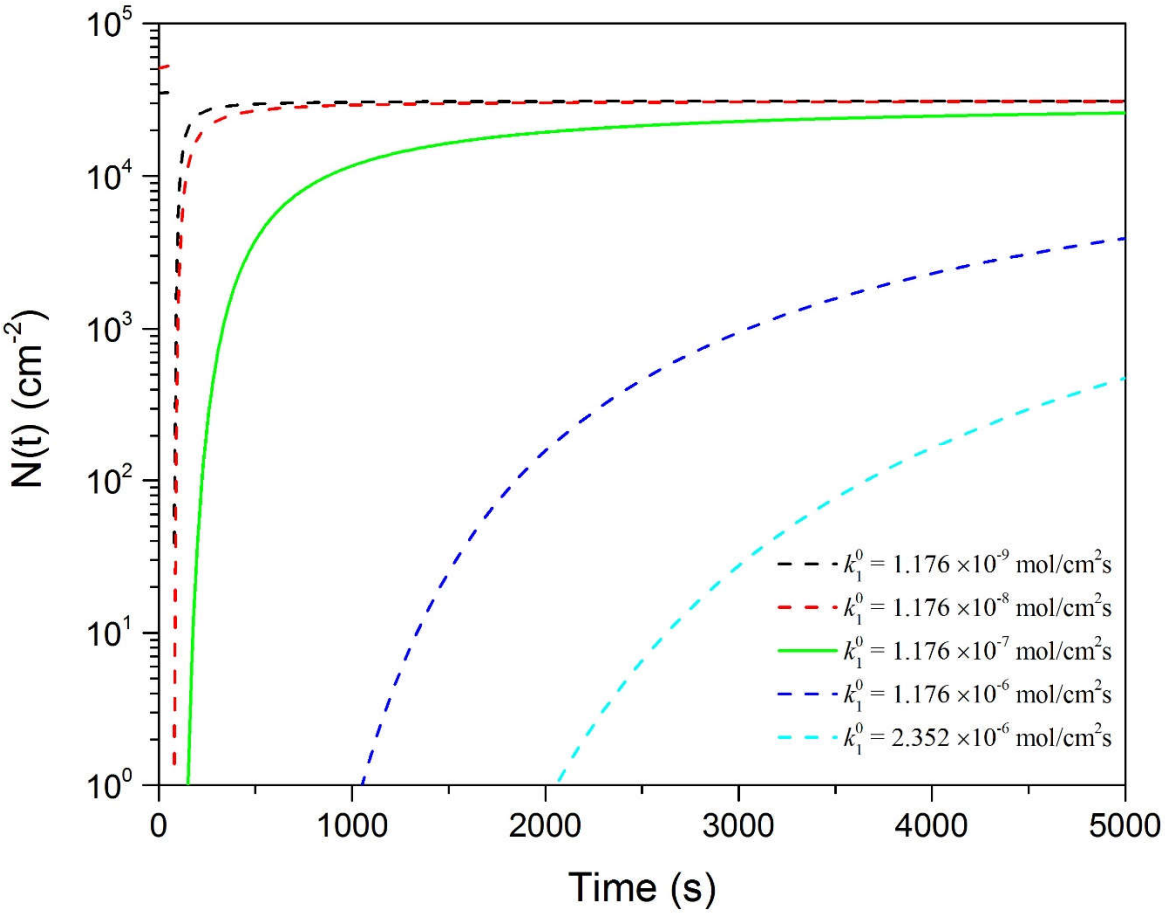

Figure 7-10: Different calculated $N(t)$ results from changing the value of standard rate constant of cation vacancy annihilation, k_1^0. The solid line represents the result obtained by optimization on the actual experimental $N(t)$ data, whereas the dash lines represent the results by manipulating k_1^0 for sensitivity analysis.

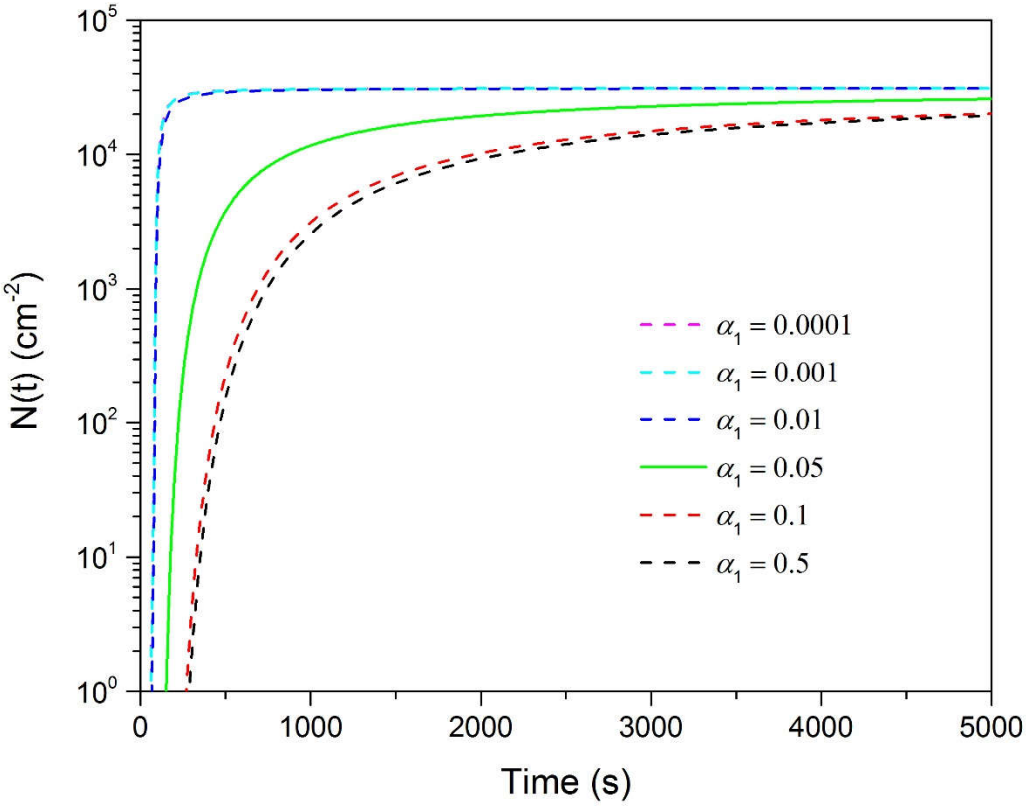

Figure 7-11: Different calculated $N(t)$ results from changing the value of the transfer coefficient of cation vacancy annihilation, α_1. The solid line represents the result obtained by optimization on the actual experimental $N(t)$ data, whereas the dash lines represent the results by manipulating α_1 for sensitivity analysis.

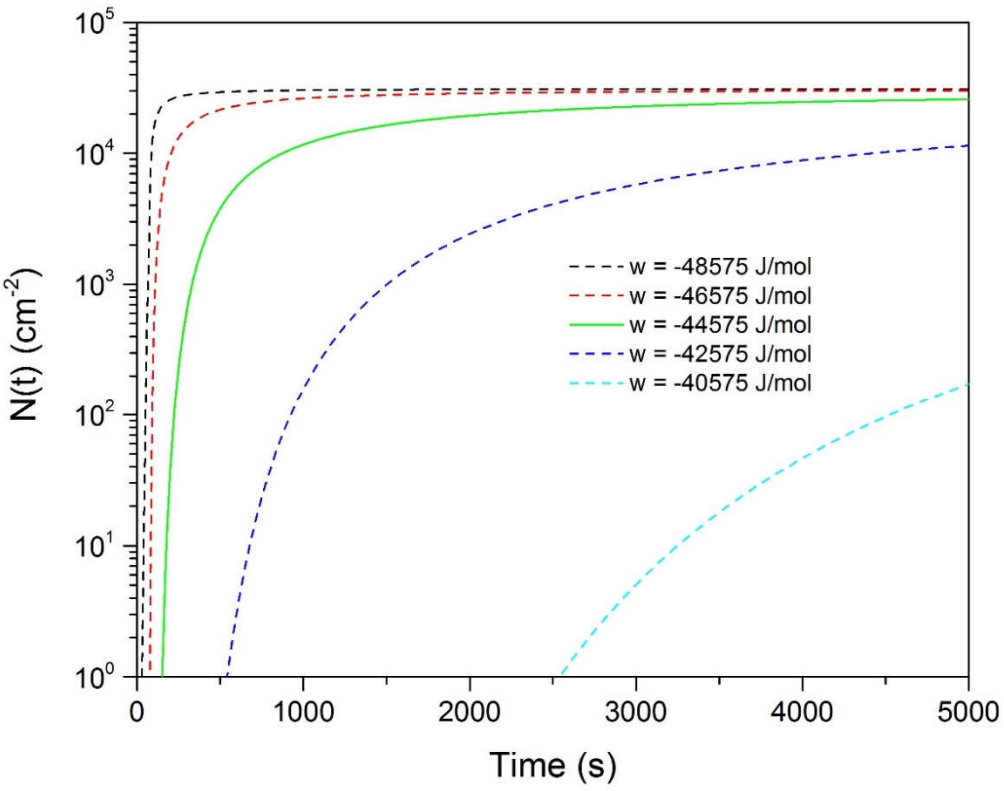

Figure 7-12: Different calculated $N(t)$ results from changing the value of the energy term, w. The solid line represents the result obtained by optimization on the actual experimental $N(t)$ data, whereas the dash lines represent the results by manipulating w for sensitivity analysis.

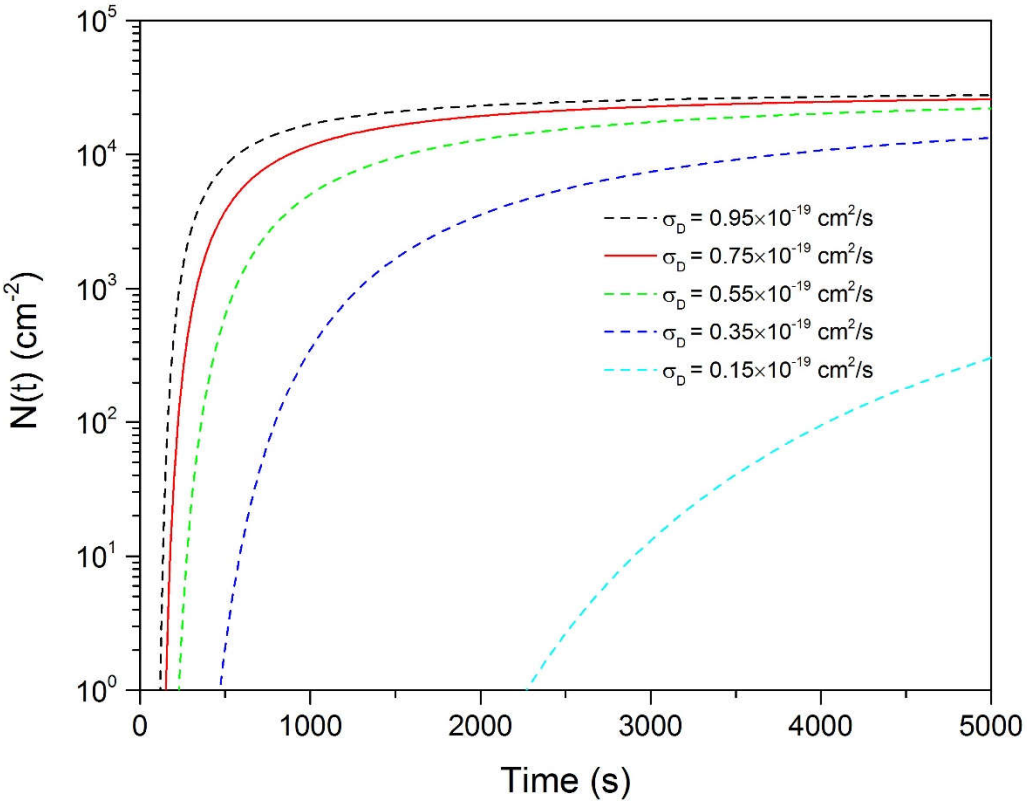

Figure 7-13: Different calculated $N(t)$ results from changing the value of the standard deviation of vacancy diffusivity, σ_D. The solid line represents the result obtained by optimization on the actual experimental $N(t)$ data, whereas the dash lines represent the results by manipulating σ_D for sensitivity analysis.

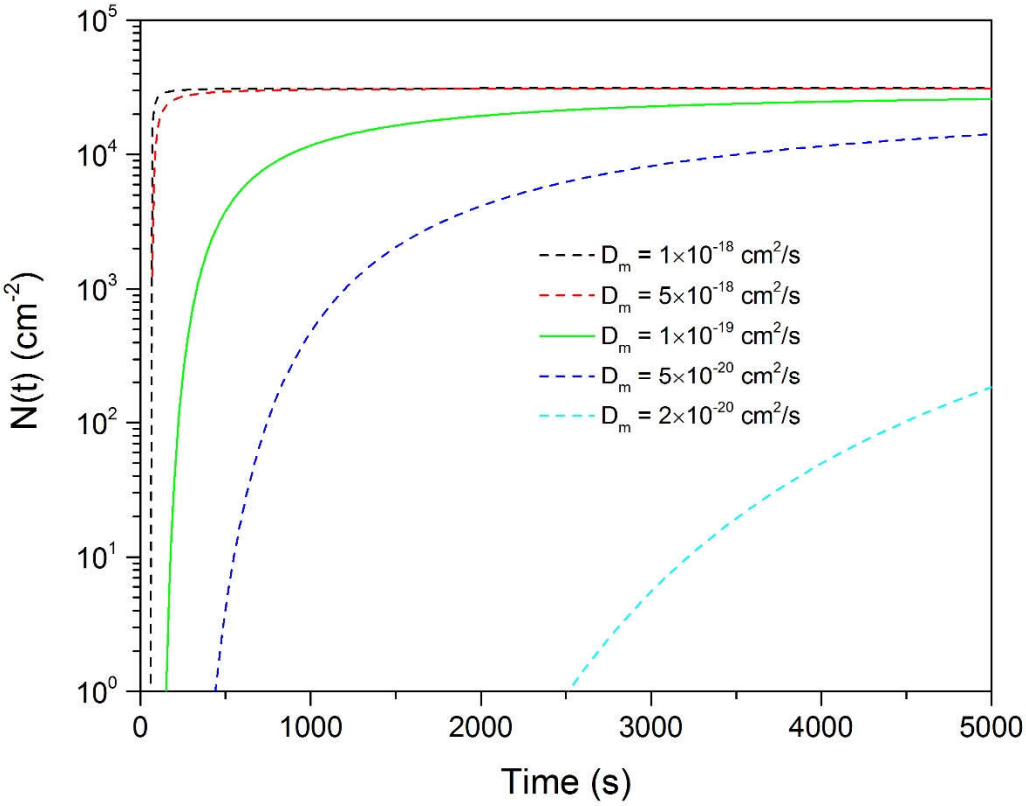

Figure 7-14: Different calculated $N(t)$ results from changing the value of the mean vacancy diffusivity, $\overline{D}$. The solid line represents the result obtained by optimization on the actual experimental $N(t)$ data, whereas the dash lines represent the results by manipulating $\overline{D}$ for sensitivity analysis.

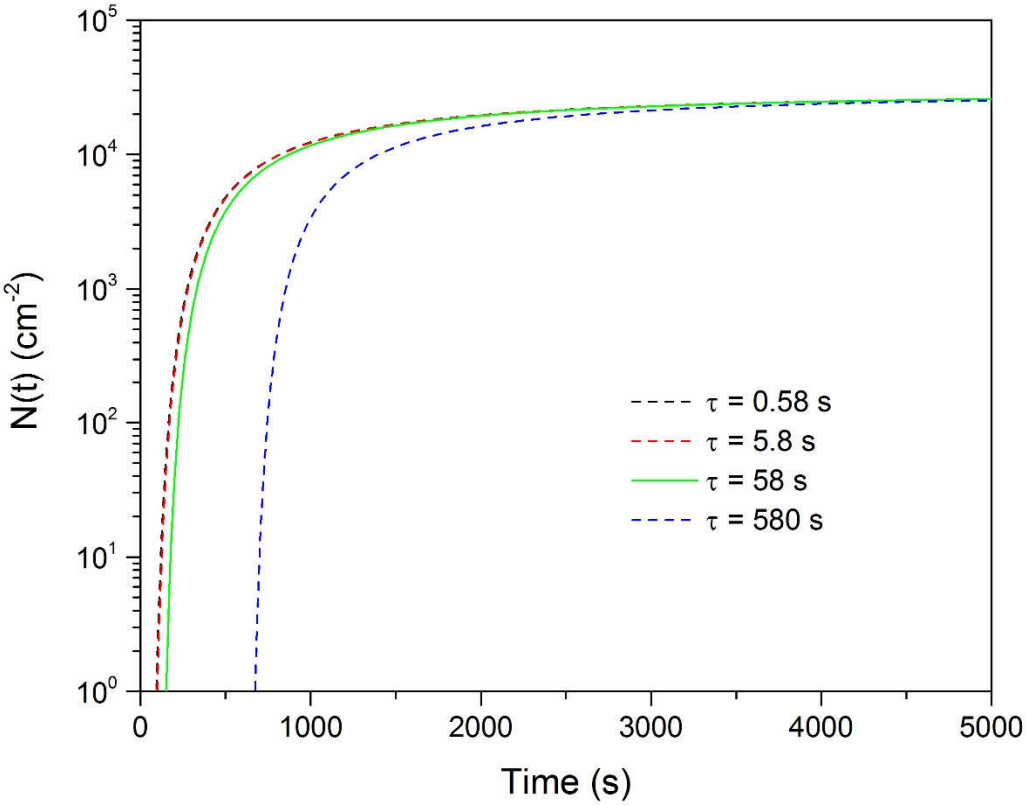

Figure 7-15: Different calculated $N(t)$ results from changing the value of the dissolution time of the cap, τ. The solid line represents the result obtained by optimization on the actual experimental $N(t)$ data, whereas the dash lines represent the results by manipulating τ for sensitivity analysis.

7.4 The Prediction of the Passivity Breakdown Potential

The critical pitting potential of the substrate, V_b, can be readily predicted by inserting the parameters values obtained from the optimization on the metastable pitting data (Table 7-3) into Eq. (7-2). The results are presented and compared with experimentally determined values in

Table **7-5** (note that the potential values are in SHE scale). For Sets I and II, the calculated V_b has a value of 0.355 V_{SHE} and 0.363 V_{SHE}, respectively, which matches very well with the data reported by Leckie and Uhlig [30] for 18-8 stainless steel in 0.1 M NaCl solutions with low pH (~0.35 V_{SHE}). The predicted values of V_b for Sets III and IV (0.426 V_{SHE} and 0.228 V_{SHE}, respectively) are also in good agreement with the pitting potential data obtained by Janik-Czachor [31] on ultra-pure iron in borate buffer solutions. Böhni and Uhlig [32] reported that the critical pitting potential for 99.99% Al in saline solutions at 25 °C follows the relationship: $V_b(V_{SHE}) = -0.124 \log a_{Cl^-} - 0.504$**,** producing a value of -0.132 V_{SHE} for a_{Cl^-} = 0.001 M, which is reasonably close to the predicted V_b for Set V, -0.0158 V_{SHE}. The pitting potential of Alloy-22, predicted from the optimization results of Set VI, also agrees well with that reported by Evans and Rebak [33] on Alloy-22 in 5 M $CaCl_2$ at 80 °C.

The comparison made above shows that the predicted- and the experimentally-obtained critical pitting potentials generally agree well, with the differences being as small as 5 mV and as large as about 77 mV, which could be regarded as being insignificant considering that several parameters involved in the optimization are assumed, due to the limited existing data. The fact that the experimental metastable pitting data, on which the prediction is based on, and the experimental V_b data originated from different independent sources, also likely contributes to the observed differences. The capability of predicting breakdown potential of various materials, as presented above, strongly demonstrates that the kinetic theory of metastable pitting in terms of the PDM developed in this paper is a powerful model for accounting for and predicting observations and phenomena related to pitting corrosion.

Table 7-5: Comparison of the predicted and experimentally-obtained pitting potential. The predicted pitting potentials are based on the optimization results reported in Table 7-3.

V_b (V_{SHE})	Set I	Set II	Set III	Set IV	Set V	Set VI
Experimental	0.350 [30]	0.350 [30]	0.402 [31]	0.151 [31]	-0.132 [32]	0.753 [33]
Predicted	0.355	0.363	0.426	0.228	-0.158	0.720

7.5 Summary

The theory for nucleation of metastable pits in terms of the PDM has been applied to the interpretation and analysis of pit nucleation data derived for six different systems. Equations describing the evolution of the nucleation rate of metastable pits and the total number of metastable pitting incidents have been tested by conducting optimization of the PDM on experimental data reported in the literature that were acquired on a variety of metallic materials, including stainless steel, carbon steel, pure iron, pure aluminum and Alloy-22. Satisfactory agreement was obtained between the fitted and experimental data for all of the selected materials, and useful fundamental parameters with reasonable values for each of those materials were extracted from the optimizations. Furthermore, predicted critical pitting potentials that are fairly close to the experimentally-measured values can be readily reproduced based on the optimization results that were obtained from independent nucleation rate data, which provides very convincing support for the validity of the optimization procedure and the PDM. The successful accounting of the independent data from multiple sources for various metallic materials strongly demonstrates that the PDM can be applied as a powerful and versatile tool for studying and understanding metastable pitting on metal surfaces.

References

[1] D.D. Macdonald, J Electrochem Soc, 139 (1992) 3434-3449.
[2] L. Lin, C. Chao, D. Macdonald, J Electrochem Soc, 128 (1981) 1194-1198.
[3] D.D. Macdonald, Electrochim Acta, 56 (2011) 1761-1772.
[4] G. Engelhardt, D. Macdonald, Corrosion, 54 (1998) 469-479.
[5] D.D. Macdonald, M. Urquidi‐Macdonald, J Electrochem Soc, 137 (1990) 2395-2402.
[6] G. Engelhardt, D.D. Macdonald, Corros Sci, 46 (2004) 2755-2780.
[7] D.D. Macdonald, Pure and Applied Chemistry, 71 (1999) 951-978.
[8] D.D. Macdonald, J Electrochem Soc, 153 (2006) B213-B224.
[9] G. Ilevbare, G. Burstein, Corros Sci, 43 (2001) 485-513.
[10] P.C. Pistorius, G.T. Burstein, Philos T Roy Soc A, 341 (1992) 531-559.
[11] Y. Cheng, J. Luo, J Electrochem Soc, 146 (1999) 970-976.
[12] M. Reuter, K.E. Heusler, Electrochim Acta, 35 (1990) 1809-1814.
[13] S. Pride, J. Scully, J. Hudson, J Electrochem Soc, 141 (1994) 3028-3040.
[14] B. Kehler, J. Scully, Corrosion, 61 (2005) 665-684.
[15] S.S. Pin Lu, Archana Mallik, Digby D. Macdonald.
[16] S. Sharifi-Asl, F. Mao, P. Lu, B. Kursten, D.D. Macdonald, Corros Sci, (2015).
[17] D.D. Macdonald, M. Urquidi-Macdonald, Electrochim Acta, 31 (1986) 1079-1086.
[18] Y. Zhang, M. Urquidi-Macdonald, G.R. Engelhardt, D.D. Macdonald, Electrochim Acta, 69 (2012) 12-18.
[19] F. Mao, C. Dong, S. Sharifi-Asl, P. Lu, D.D. Macdonald, Electrochim Acta, 144 (2014) 391-399.

[20] R. Cerbo, A. Seybolt, Journal of the American Ceramic Society, 42 (1959) 430-431.
[21] D.E. Williams, J. Stewart, P.H. Balkwill, Corros Sci, 36 (1994) 1213-1235.
[22] A. Lloyd, D. Shoesmith, N. McIntyre, J. Noel, J Electrochem Soc, 150 (2003) B120-B130.
[23] D.D. Macdonald, A. Sun, N. Priyantha, P. Jayaweera, J Electroanal Chem, 572 (2004) 421-431.
[24] N. Priyantha, P. Jayaweera, D.D. Macdonald, A. Sun, J Electroanal Chem, 572 (2004) 409-419.
[25] D. Zagidulin, X. Zhang, J. Zhou, J.J. Noël, D.W. Shoesmith, Surface and Interface Analysis, 45 (2013) 1014-1019.
[26] A.C. Lloyd, J.J. Noël, S. McIntyre, D.W. Shoesmith, Electrochim Acta, 49 (2004) 3015-3027.
[27] X. Zhang, D. Zagidulin, D.W. Shoesmith, Electrochim Acta, 89 (2013) 814-822.
[28] D. Dunn, Y. Pan, L. Yang, G. Cragnolino, Corrosion, 62 (2006) 3-12.
[29] D. Dunn, Y. Pan, L. Yang, G. Cragnolino, Corrosion, 61 (2005) 1078-1085.
[30] H. Leckie, H. Uhlig, J Electrochem Soc, 113 (1966) 1262-1267.
[31] M. Janik-Czachor, British Corrosion Journal, 6 (1971) 57-60.
[32] H. Bohni, H.H. Uhlig, J Electrochem Soc, 116 (1969) 906-910.
[33] K.J. Evans, R.B. Rebak, PV2002-13, (2002) 344-354.

Chapter 8 The Pitting Corrosion of Carbon Steel in Alkaline Solutions

8.1 Introduction

Carbon steel usually forms a protective surface oxide film when in contact with concrete, due to the alkaline nature of the concrete pore solution (pH ≈ 13.5 at room temperature) [1, 2]. However, the breakdown of the protective layer may occur leading to an active, localized corrosion of the metal. The presence of aggressive anions, such as chloride ion, is the most common reason for passivity breakdown and localized attack. It is known that the concentration of aggressive and nonaggressive anions in the solution, pH of the solution, and temperature all play important roles in determining the pitting susceptibility of metals and alloys [3]. Passivity breakdown and pit nucleation are considered to be the initial events in the accumulation of localized corrosion damage on a metal surface [4]. In many instances, stress corrosion and corrosion fatigue cracks nucleate at pits, so that passivity breakdown and the development of a critical pit may be considered as describing the initiation process or the development of stress corrosion cracks and corrosion fatigue cracks [4]. Over the past several decades, researchers have studied the corrosion of steel reinforcement in concrete. The reinforcement ("rebar") is made from different materials, but most commonly from carbon steel [5-15]. However, the results reported in the literature are scattered over large ranges, and the majority of them, if not all, have been limited to typical climatic temperatures and the author is not aware of any previous work that has focused on systems at the higher temperatures and that are relevant to the disposal of HLNW in Belgium. It should be noted that the structure of concrete is very complex, and it has been shown that its characteristics have a dominant effect on the corrosion processes. It is believed, however, that the present investigation of the corrosion behavior of carbon steel in simple alkaline solutions, similar to many respects to the concrete pore solution, will contribute to a better understanding of the behavior of embedded carbon steel container.

It has been experimentally observed in the laboratory of this group that pitting corrosion rarely occurs on the carbon steel specimen surface by potentiodynamic polarization at pH of 13.5 (SCPS). This finding is inconsistent with some other work where pitting attack on carbon steel in alkaline chloride-containing solutions was reported [5, 11, 12, 16], which may be attributed to the specific properties of CarElso 70 SOHIC, e.g., the very low content of impurities such as S and P, and the relatively more uniform phase distribution due to optimized heat treatment. In light of the difficulty in obtaining passivity breakdown data effectively at pH of 13.5, a series of experiments were carried out at lower pH values (pH = 8.3, 9.0, 10.0, 11.5, and 12.4 at 25 °C). The work at pH of 12.4 was conducted in saturated $Ca(OH)_2$ and is presented in detail in this chapter. The results for the rest of the pH values were mainly obtained by other group members and are summarized here to examine the effect of pH on passivity breakdown. The goals of this chapter are to: (1) study the localized corrosion behavior of carbon steel in sat. $Ca(OH)_2$ as a function of temperature, chloride ion concentration, and potential scan rate; (2) statistically analyze the relationship between the passivity breakdown potential versus chloride ion concentration and temperature in terms of the PDM [4, 17-21], in order to extract the model parameters, and (3) demonstrate that the PDM incorporating a normal distribution of the potential breakdown sites on the surface with respect to the diffusivity of cation vacancies in the barrier layer, adequately accounts for the experimentally observed distribution in the critical breakdown voltage.

8.2 Results in Saturated $Ca(OH)_2$ Solution (pH ≈ 12.4 at 25 °C)

Figure 8-1 shows some microscopic pictures of the sample surface after the current density increased sharply in the potentiodynamic polarization of carbon steel in the sat. $Ca(OH)_2$ solution at 85 °C, demonstrating that the current increase was indeed due to pitting attack instead of crevice corrosion. The results from potentiodynamic polarization experiments conducted at different chloride concentrations and different temperatures are presented in Figure 8-2 to Figure 8-4. A decrease in the breakdown potential (V_b) associated with the passivity breakdown for carbon steel is seen as the chloride concentration increases for all temperatures. The fact that the corrosion potential also shifts toward lower values with increasing chloride concentration has been previously observed [11]. As seen in the data, when the potential is swept in the positive direction, the polarization curve exhibits a wide passive range, followed by a sharp increase in the polarization current density signifying passivity breakdown at a critical pitting potential. In some cases, namely, for 0.1 M chloride concentration at 25 °C and for 0.01 M chloride concentration at 55 °C, at potentials higher than 0.7 V_{SCE} an increase in the current density was observed, which is due to the onset of oxygen evolution reaction, although passivity breakdown may occur simultaneously. Another feature to be noted in these plots is the presence of a number of short-period current spikes below the critical breakdown potential. These current spikes are due to breakdown of passive film followed immediately by repassivation (i.e., due to metastable pitting). Metastable pitting has been observed on many metals and alloys including iron-chromium alloys, titanium, stainless steel and aluminum [22-25]. The kinetics of metastable pit nucleation has been addressed at some length using the PDM in Chapter 7.

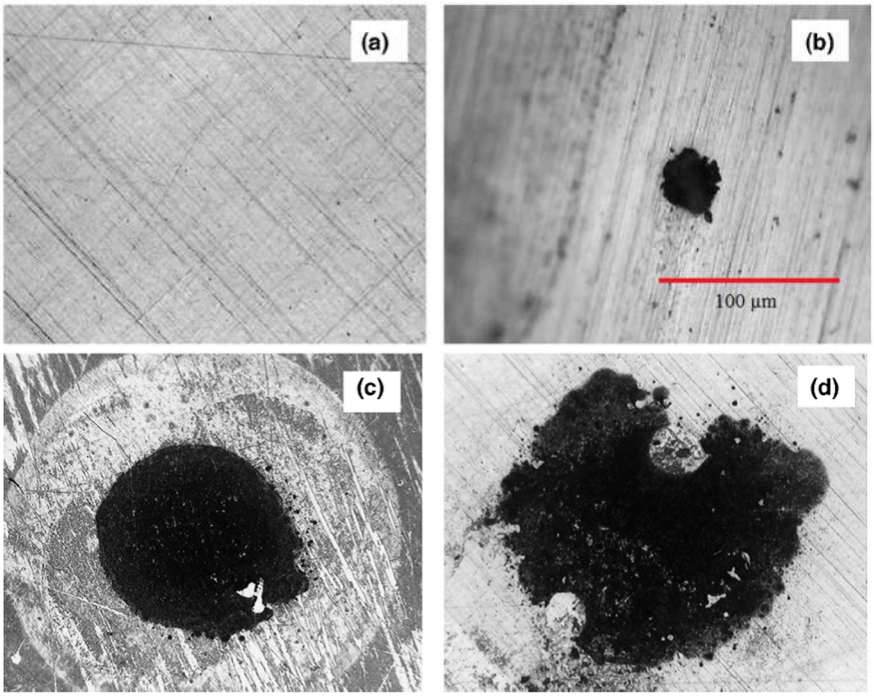

Figure 8-1: Microscopic observation of carbon steel at 85 °C in (a) prior to the experiment, (b) after exposure to 0.1 M NaCl, (c) 0.5 M NaCl and (d) 1 M NaCl, after breakdown (i_{max} = 100 µA cm^{-2}). Magnification 100×. Place a scale marker (e.g., a line of length equivalent to 100 µm) on one of the photos.

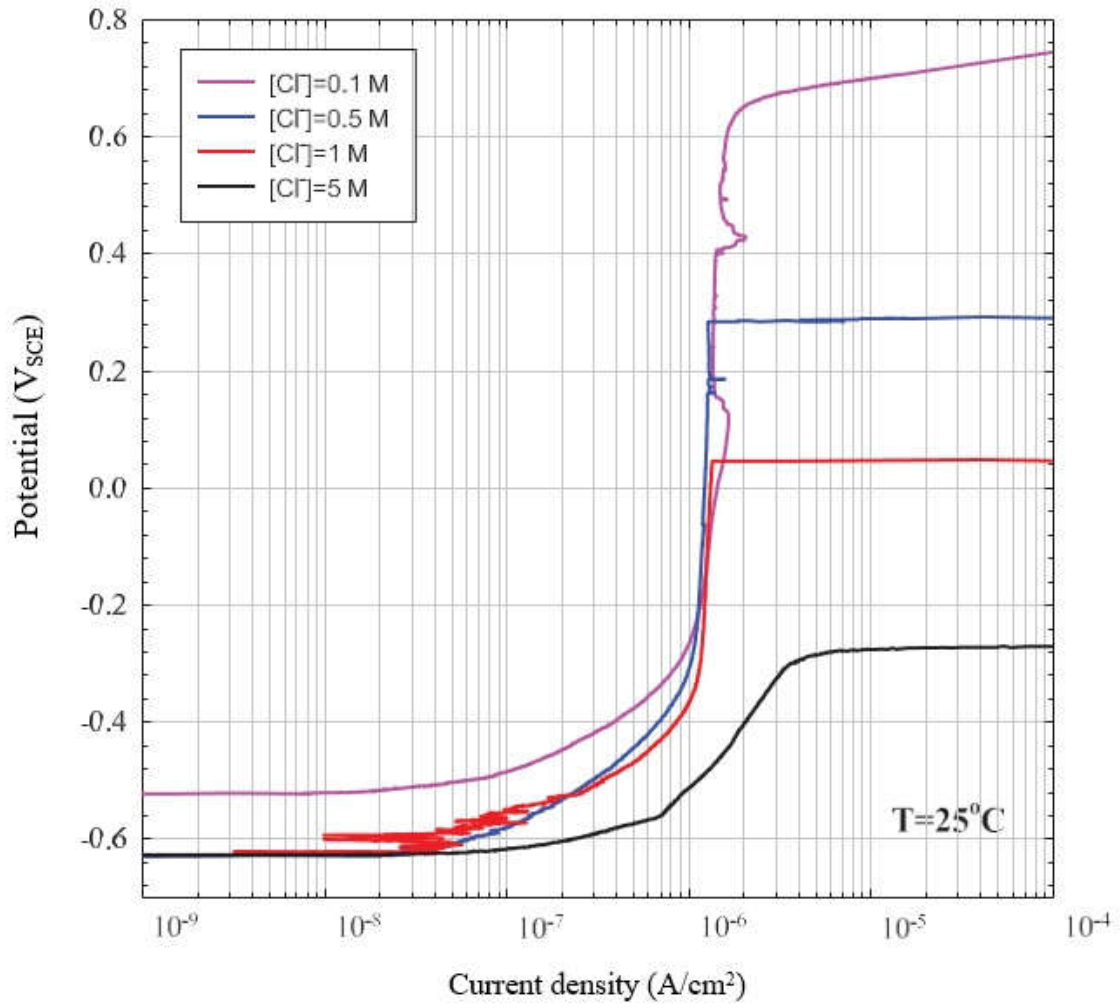

Figure 8-2: Potentiodynamic scans performed on carbon steel in saturated $Ca(OH)_2$ with various amounts of NaCl added at 25 °C (scan rate of 0.1667 mV s^{-1}).

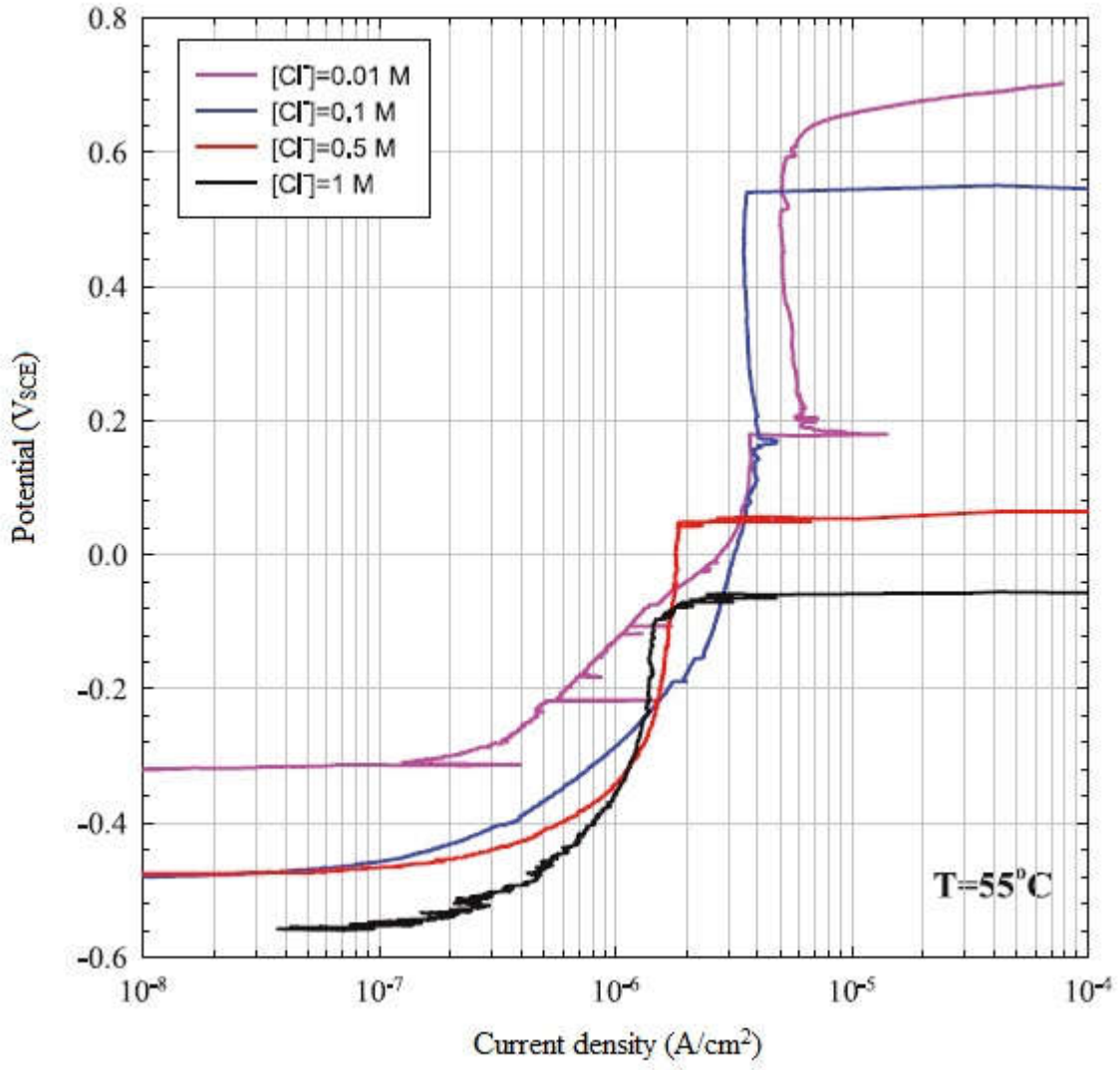

Figure 8-3: Potentiodynamic scans performed on carbon steel in saturated $Ca(OH)_2$ with various amounts of NaCl added at 55 °C (scan rate of 0.1667 mV s^{-1}).

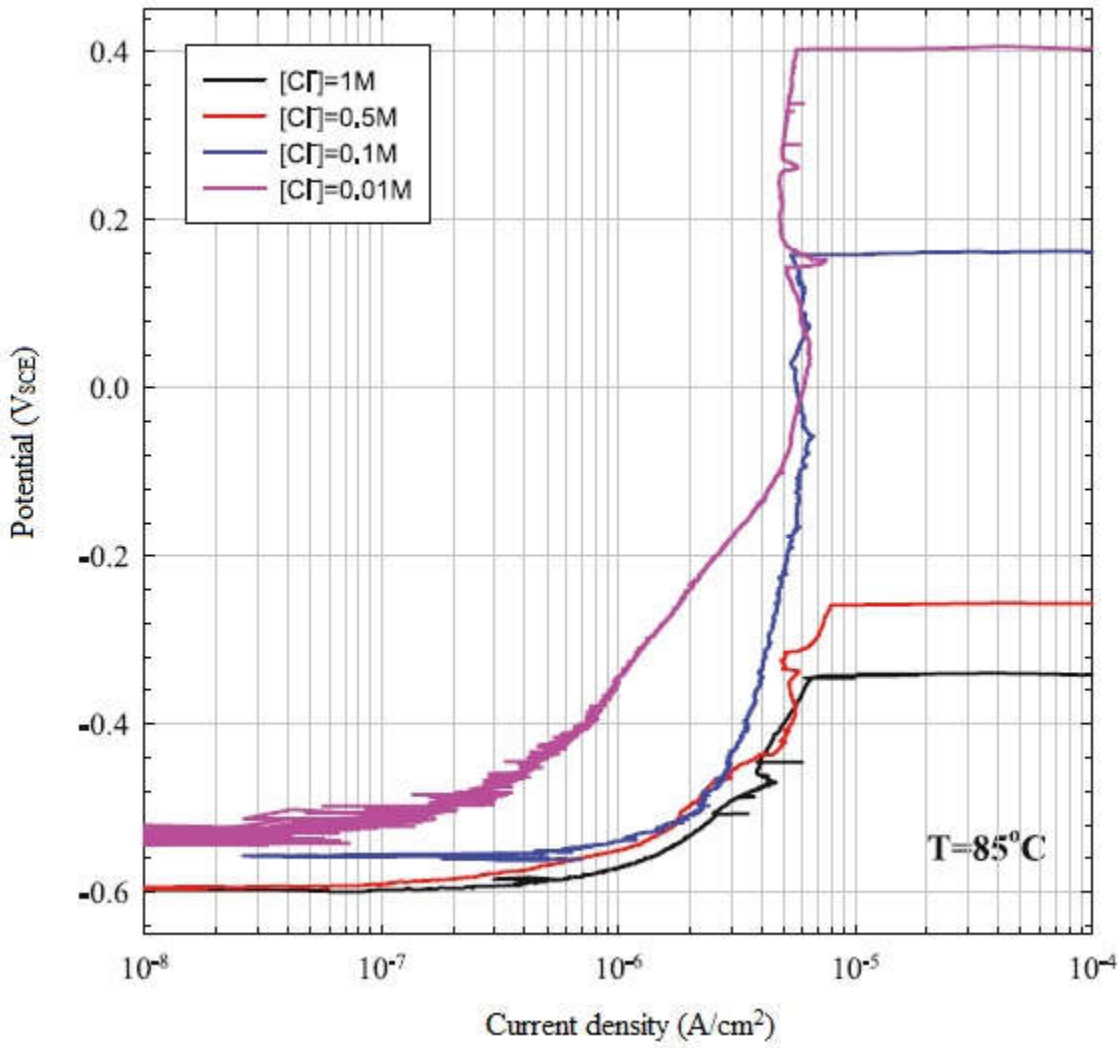

Figure 8-4: Potentiodynamic scans performed on carbon steel in saturated $Ca(OH)_2$ with various amounts of NaCl added at 85 °C (scan rate of 0.1667 mV s^{-1}).

8.2.1 Effect of Activity of Chloride Ions

A simple logarithmic relationship between the breakdown potential and concentration of the aggressive anion has been proposed previously by many researchers [3, 4, 26, 27]. The PDM provides a similar relationship between V_b and a_{X^-} as shown in Eqs. (7-2) and (7-3), which are repeated below for reference convenience.

$$V_b = \frac{4.606RT}{\chi\alpha F}\log\left[\frac{\lambda}{D}\right] - \frac{2.303RT}{\alpha F}\log a_{X^-} \tag{7-2}$$

where

$$\lambda = \frac{RTJ_m\Omega}{F\chi\varepsilon N_A}\exp\left[\frac{\Delta G_S^o + (\chi/2)\Delta G_A^o - (\chi/2)\beta F\mathrm{pH} - (\chi/2)F\phi_{f/s}^0}{RT}\right] \tag{7-3}$$

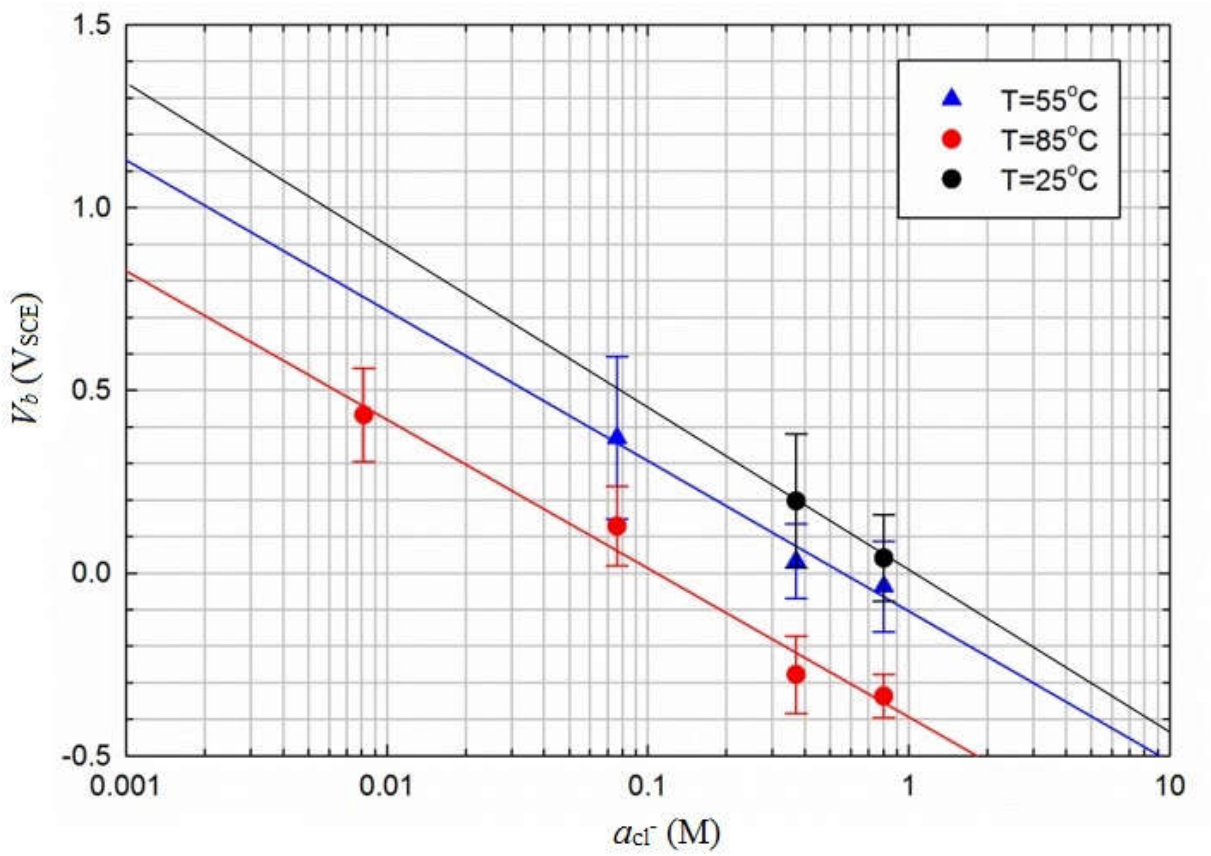

Figure 8-5 illustrates the relationship between the passivity breakdown potential for carbon steel and the activity of chloride ions in deaerated sat. $Ca(OH)_2$ solution for different temperatures. As can be seen from this figure, the breakdown potential decreases linearly with the logarithm of the chloride ion activity at all three temperatures. From the slope of the linear relationship, $-2.303RT/\alpha F$, the value of α (the polarizability of the bl/s interface) can be determined. The obtained results for α are 0.15, 0.15, and 0.16 at 25 °C, 55 °C, and 85 °C, respectively, showing that the polarizability of the barrier layer/solution interface is fairly insensitive to the temperature. These results are also in close agreement with the recently reported value of Tan et al. [28] (α = 0.16) at 23 °C. The energy term, w, associated with the absorption of Cl^- as defined in Eq. (7-4), which is contained within λ, can also be obtained from the intersection of the V_b vs. $\log a_{Cl^-}$ with the V_b axis, and the results are shown later in Table 8-1. The mean molar activity coefficients $\gamma_{\pm}$ for Cl^- in NaCl + $Ca(OH)_2$ solutions of different concentrations were taken from Ref. [29] and were used to calculate the activity of the chloride ion. Another point to note is that the standard deviation for the distribution in the breakdown potential was generally smaller at higher chloride concentrations for all temperatures.

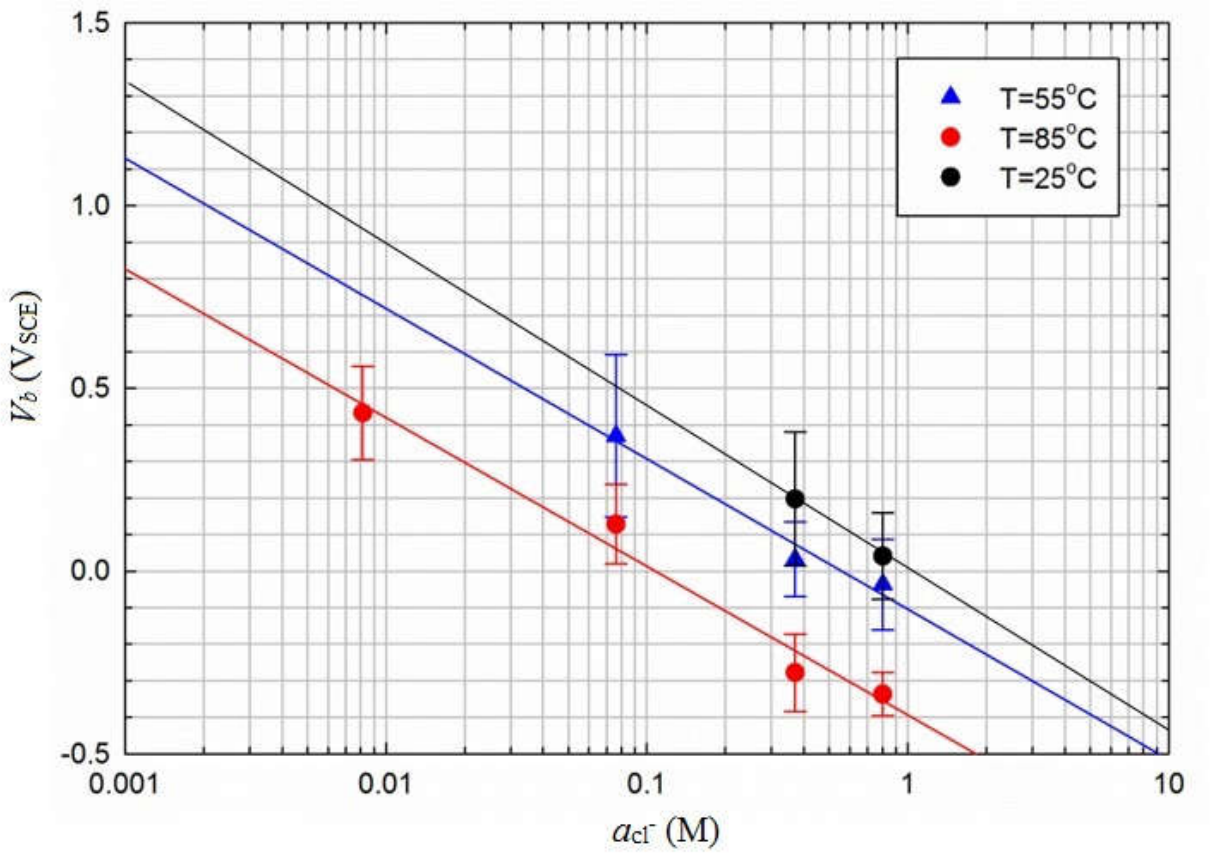

Figure 8-5: Mean value of the passivity breakdown potentials (V_b) for carbon steel in deaerated sat. $Ca(OH)_2$ solution as a function of the logarithm of the chloride activity at different temperatures.

8.2.2 Effect of Temperature

It is generally accepted that temperature is one of the most important factors affecting pitting corrosion. As can be seen from

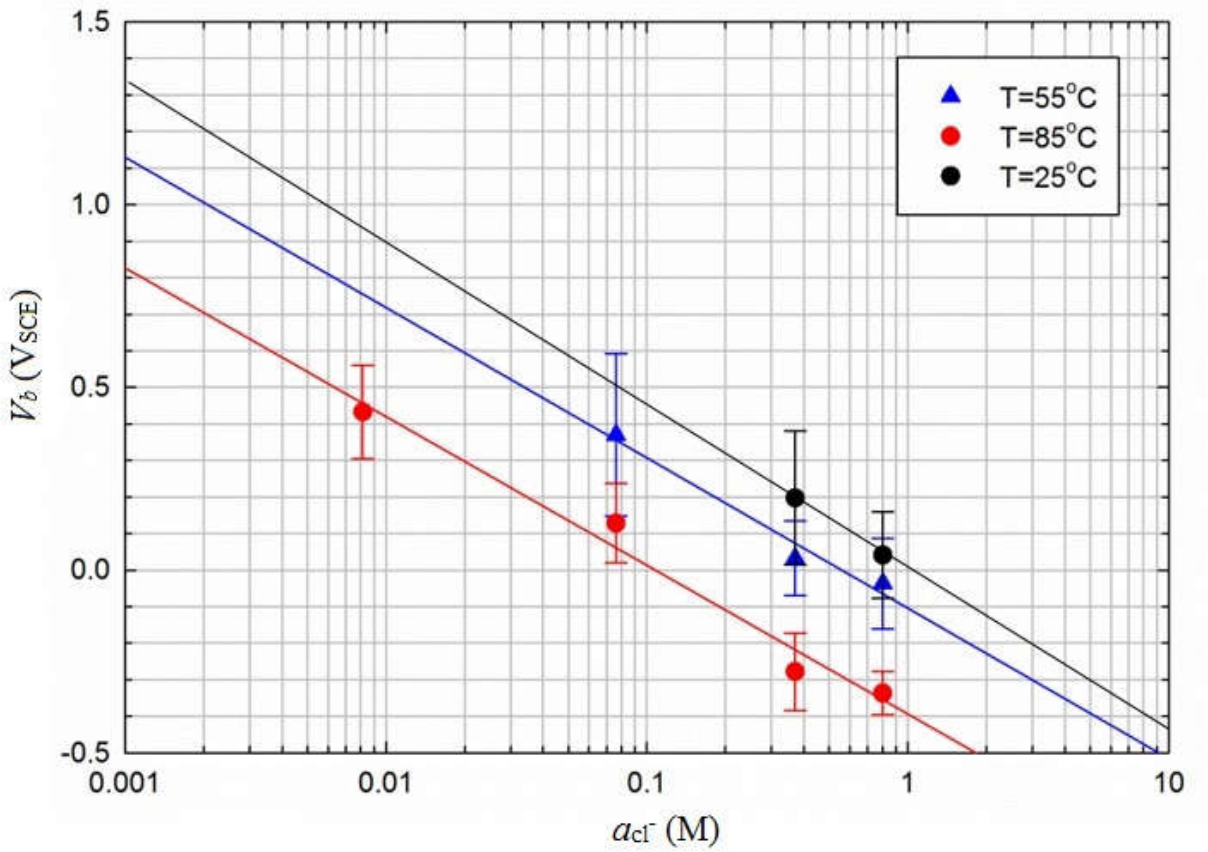

Figure 8-2 to Figure 8-4, an increase in temperature leads to a shift of the passivity breakdown potential toward more active (negative) values. This indicates that the resistance to pitting corrosion of carbon steel under the conditions of interest decreases with increasing temperature, which is in agreement with previously reported data [30]. Figure 8-6 shows that the mean passivity breakdown potential decreases linearly with increasing temperature for different chloride concentrations. For [Cl^-] = 0.01 M, passivity breakdown was only observed at 85 °C, so linear fitting at this chloride concentration was not performed. Similar linear behavior has been reported previously by Soltis et al. [31] on the temperature dependence of the pitting potential of high purity aluminum alloys in chloride containing solutions. It is known that the rate of the chemical and electrochemical reactions becomes faster as temperature increases. Therefore, it was anticipated that susceptibility to the pitting corrosion would increase with increasing temperature, and the pitting potential is found to vary inversely with temperature, which is exactly as observed in Figure 8-6. The temperature coefficient for the breakdown potential can be obtained from the slopes, which equal to 6.3 mV/°C, 7.9 mV/°C, and 10.4 mV/°C, for 1 M, 0.1 M and 0.01 M [Cl^-], respectively. This trend indicates that the passive system is more sensitive to increasing temperature at lower levels of [Cl^-].

Another point to be noted here is the effect of temperature on pH of the solution. As we can see from Table 3-2, an increase of solution temperature will cause a decrease in its pH due to an increase in the number of ions in solution as a result of dissociation of molecules (e.g., an enhanced dissociation of H_2O increases $[H^+]$ and decreases pH). Generally, for iron and steels, an increase in pH at constant temperature causes the value of V_b to become more positive, because of the inhibitory effect of OH^- to passivity breakdown [3, 32, 33]. In the case of varying temperature, the impact of temperature on V_b outweighs the impact of temperature on pH, with the net result that V_b shifts strongly in the negative direction.

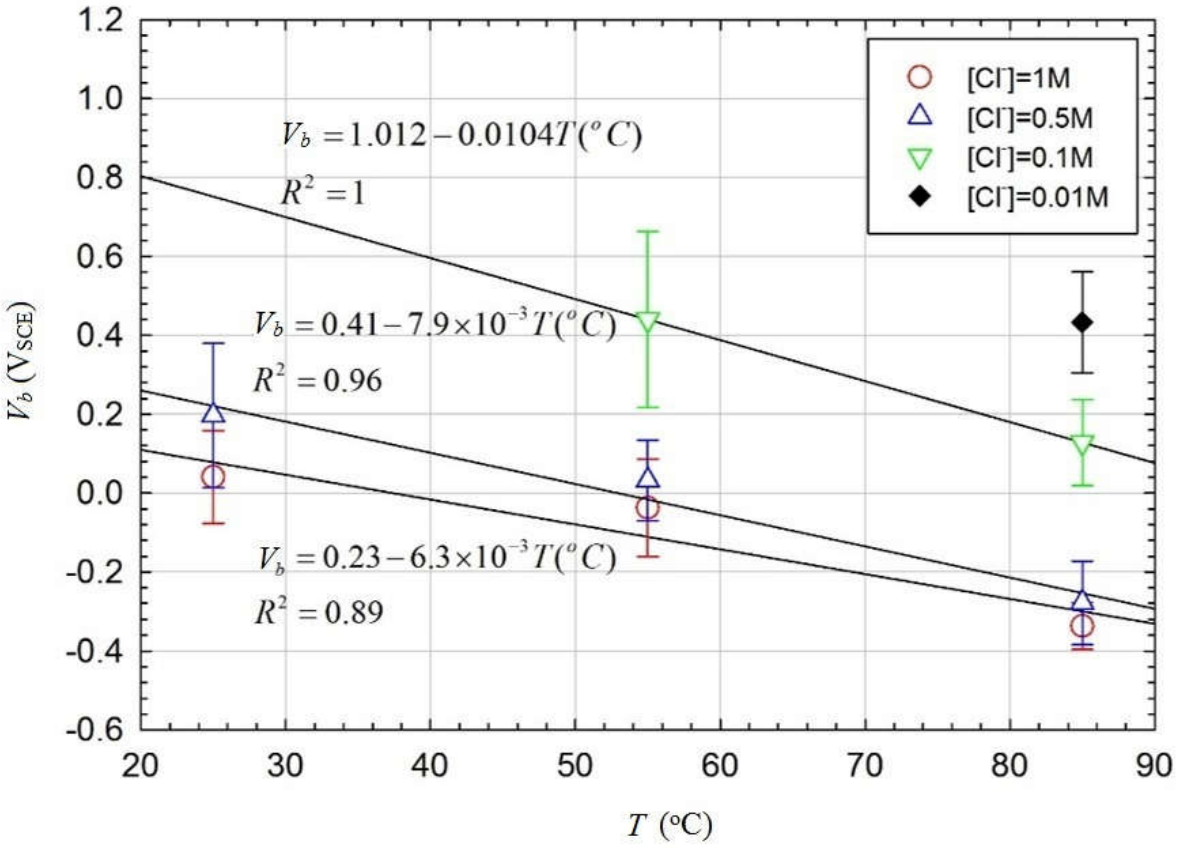

Figure 8-6: Mean values of the passivity breakdown potentials (V_b) for carbon steel in deaerated sat. $Ca(OH)_2$ solution as a function of temperature at different chloride concentrations.

8.2.3 Effect of Scan Rate of Potential

It is well-understood that the passivity breakdown potential often depends on the method of its determination and, in particular, on the potential scan rate [8] when determined potentiodynamically. Also, several researchers [3, 34-37] have found that the more noble the potential is held, the shorter is the time required for pit initiation. Accordingly, when the potential scan rate is high, a rapid increase in current density can only be observed at more positive (noble) potentials, in compensation for the shorter time that is available for breakdown. In other words, the passivity breakdown potential is expected to become more positive at higher potential scan rates.

As noted above, when potentiodynamic polarization is used to determine the passivity breakdown potential (V_b), the potential sweep rate (v) influences the value of the breakdown potential obtained [4]. The PDM provides an analytical relationship between the passivity breakdown potential (V_b) and scan rate (v) in the form of Eq. (8-1) [4], which can be used to determine the ratio of ξ/J_m:

$$V_b(v) = \left(\frac{2\xi RT}{J_m \chi \alpha F} \right)^{1/2} v^{\frac{1}{2}} + V_b(v=0) \tag{8-1}$$

where $V_b(v = 0)$ is defined as the breakdown potential at zero potential scan rate and all the other parameters have been defined previously in Section 7.1.

Potentiodynamic polarization at different potential scan rates (from 0.1667 to 10 mV s^{-1}) was used to determine the passivity breakdown potential on carbon steel in deaerated sat. $Ca(OH)_2$ solution containing 1 M chloride concentrations at 25 °C. Three measurements were done for each scan rate that is not 0.1667 mV s^{-1}. The measured breakdown potentials (V_b), change linearly with the square root of potential scan rate ($v^{1/2}$), within experimental error, as shown in Figure 8-7 and is in agreement with the prediction of the PDM [Eq. (8-1)], the average slope was found to be equal to 1.84 (V s^{-1})$^{1/2}$ and hence, the value of ξ/J_m was calculated to be equal to 15.89 s, 14.12 s and 15.13 s at 25 °C, 55 °C and 85 °C, respectively.

The rate of annihilation of cation vacancies at the metal/barrier layer interface under the steady-state condition, J_m, can be obtained by conducting optimization of the PDM on the metastable pit nucleation data, as addressed in Chapter 7. J_m may be also estimated experimentally from the passive current density immediately before the passivity breakdown, i_{ss}^{bd} (v = 0.1667 mV s^{-1}):

$$J_m \leq \frac{i_{ss}^{bd} N_A}{\chi F} \tag{8-2}$$

where $N_A = 6.023 \times 10^{23}$ is Avogadro's number, $\chi = 3$ (the barrier layer is assumed to be Fe_2O_3), and i_{ss}^{bd} is estimated to be equal to 1.65×10^{-6} A cm^{-2}, 3.25×10^{-6} A cm^{-2} and 1.65×10^{-5} A cm^{-2} at 25 °C, 55 °C and 85 °C, respectively, from the potentiodynamic polarization experiments. As a result, we can calculate J_m based upon Eq. (8-2), as $J_m \leq 3.43 \times 10^{12}$ cm^{-2} at 25 °C, $J_m \leq 6.76 \times 10^{12}$ cm^{-2} at 55 °C, and $J_m \leq 3.43 \times 10^{13}$ cm^{-2} at 85 °C. Finally, the critical areal concentration of cation vacancies (ξ) is readily calculated as being $\leq 5.45 \times 10^{13}$ cm^{-2} (at 25 °C), $\leq 9.55 \times 10^{13}$ cm^{-2} (at 55 °C) and $\leq 5.19 \times 10^{14}$ cm^{-2} (at 85 °C). Note that the inequality in Eq. (8-2) arises from the fact that the majority of the passive current, in the case of carbon steel, is carried by metal interstitials as demonstrated in Section 6.5, thereby rendering the barrier layer n-type in electronic character, and not by the cation vacancies that are postulated to lead to passivity breakdown and which dope the barrier layer p-type. As discussed in Section 7.2, ξ can also be estimated from the unit cell dimensions of the barrier layer and/or the base metal. The unit cell for the barrier layer (Fe_2O_3) is rhombohedral with $a_{rh} = 5.427$ Å and $\alpha_{rh} = 55.271°$ [38] whereas that for the base metal is either Body Centered Cubic (BCC) (in case of α-iron) with the lattice parameter $a = 2.863$ Å [39] or Face Centered Cubic (FCC) (in case of γ-iron) with $a = 3.595$ Å. Therefore, the density of iron atoms per unit area in a monolayer of the unit cell of the barrier layer and the base metal calculated to be equal to 4.13×10^{14} cm^{-2} and $\sim 10^{15}$ cm^{-2}, which are in reasonable agreement with the values obtained previously from the experimental relationship between V_b and v.

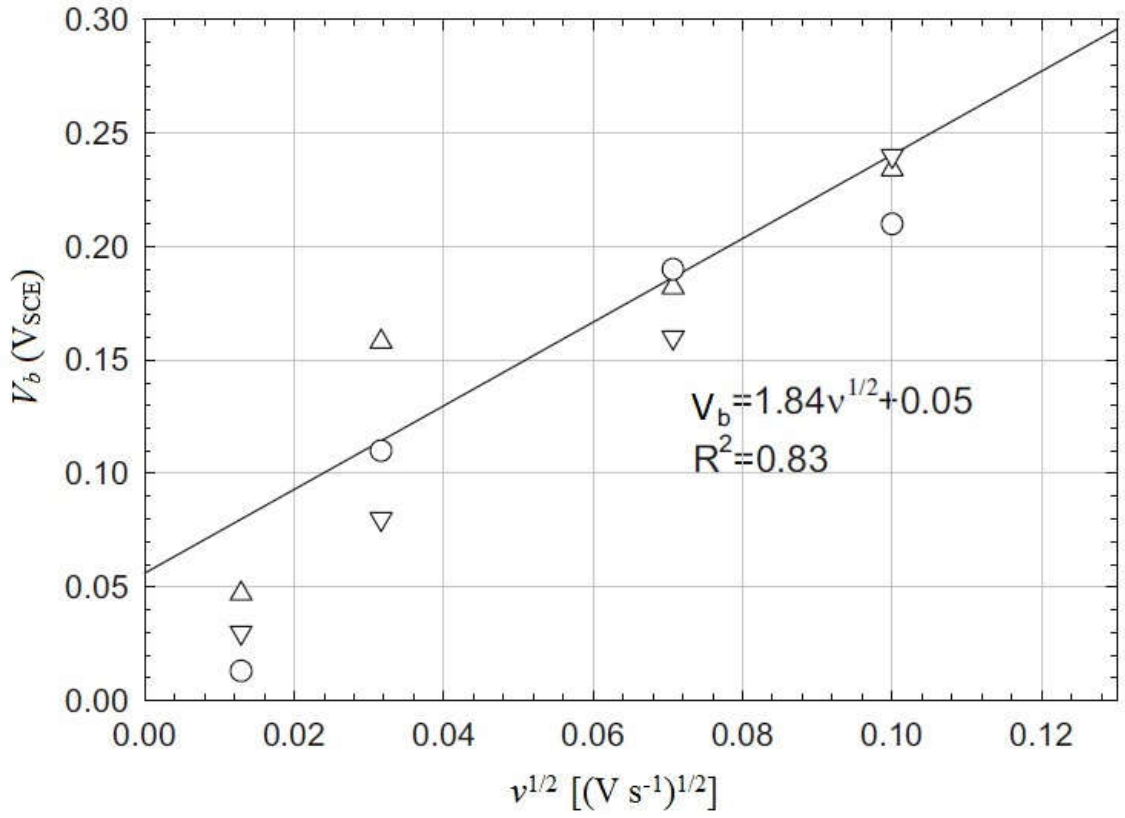

Figure 8-7: Measured breakdown potentials (V_b) at different potential scan rates (v) for carbon steel in deaerated sat. $Ca(OH)_2$ +1 M NaCl solution at 25 °C. Experiments at each v were repeated three times as represented by the open symbols in the figure.

8.2.4 Numerical Analysis of Probability Distribution in Breakdown Potential

The near-normal distribution in breakdown potential is attributed to a normal distribution of potential breakdown sites with respect to the cation vacancy diffusivity, D (the distribution is characterized by a mean value, $\overline{V_b}$, and a standard deviation,σ_D), noting that a large number of breakdown sites exist upon a barrier film per unit area [40]. The breakdown sites represent structural defects in the passive film that are assumed to have high, but normally distributed, cation vacancy diffusivity. The width of this distribution is reflected in the standard deviation, σ_D, in the cation vacancy diffusivity; a larger value of σ_D implies a wider distribution in the cation vacancy diffusivity characterizing the population of breakdown sites. In order to compare the prediction of the PDM with experimental data, the cumulative probability in breakdown potential is defined as [41, 42]:

$$P(V_b) = \frac{\int_{V_b}^{-\infty} (\mathrm{d}N/\mathrm{d}V_b)\mathrm{d}V_b}{\int_{+\infty}^{-\infty} (\mathrm{d}N/\mathrm{d}V_b)\mathrm{d}V_b} \tag{8-3}$$

and

$$\frac{\mathrm{d}N}{\mathrm{d}V_b} = \frac{-b\gamma'}{\sqrt{2\pi}\sigma_D a_{\mathrm{Cl}^-}^{\chi/2}} \exp\left[\frac{-\left(\mathrm{e}^{-\gamma' V_b} - \mathrm{e}^{-\gamma' \overline{V_b}}\right)^2 b^2}{2\sigma_D^2 a_{\mathrm{Cl}^-}^{\chi}}\right] \exp(-\gamma' V_b) \tag{8-4}$$

where $\gamma' = \chi\alpha F/2RT$, and b is the parameter defined in Eq. (7-13). Numerical analysis has been performed on experimentally obtained data for V_b, as described previously, using Wolfram Mathematica 10.1 software. The mean diffusivity of cation vacancies is found to be equal to 5×10^{-19}, 5×10^{-19} and 7×10^{-19} ($\mathrm{cm^2\ s^{-1}}$) at 25 °C, 55 °C and 85 °C, respectively. The remaining parameters, such as α, ξ, w and etc., were obtained from the analysis of the experimental results of the potentiodynamically determined passivity breakdown potentials as a function of chloride activity, a_{Cl^-}, and scan rate, v, as described in previously sections. We performed a one-step optimization, in order to obtain the values of the PDM parameters at the lowest chloride ion concentration, and we then used them to predict the distribution in the passivity breakdown potential at higher concentrations of chloride ion. Figure 8-8 and Figure 8-9 display the cumulative probability plots for the breakdown potential as a function of chloride concentration at 55 °C and 85 °C. The calculated distributions, based upon the PDM using $\sigma_D \sim 0.5\overline{D}$, are also plotted as solid lines in these figures and the extracted parameters are listed in Table 8-1. Satisfactory correlation between experimental and calculated distribution in the breakdown potential has been generally observed, which confirms the validity of the PDM for the describing the breakdown of the passive film on carbon steel.

Readers may notice that several parameters reported in Table 8-1, including ξ, J_m, w, and σ_D, can also be obtained by performing optimization of the PDM on metastable pit nucleation rate data,

as discussed at depth in the previous Chapter 7. Specifically, the optimization results of those parameters for Set III (Table 7-3), where the original experimental data [25] were also acquired on carbon steel (although with differences in the material composition and experimental conditions to the present work), are compared in

Table **8-2** with the parameter values obtained from the numerical analysis on the data of passivity breakdown potential as presented earlier in this chapter. The agreement between the two sets of results appears fairly good. The observable difference may be considered insignificant due to the different compositions of the carbon steel being studied (e.g. A516-70 has much higher carbon and sulfur content than CarElso 70 SOHIC does) and, probably more importantly, the substantial discrepancy in the nature of the experiments that were conducted to obtain the raw data: the metastable pit nucleation rate data were generated potentiostatically, whereas potentiodynamic experiments under various conditions (i.e. multiple a_{X^-} and v) were carried out to generate the passivity breakdown potential data.

Table 8-1: Parameter values used in calculating cumulative probabilities in the breakdown potential for carbon steel in deaerated sat. $Ca(OH)_2$ + X, M NaCl (pH 12.5 ± 0.1 at 25 °C) with different chloride concentrations at different temperatures.

Parameters	**Values**			**Units**	**Sources**
	T = 25 °C	T = 55 °C	T = 75 °C		
Ω, molar volume of Fe_2O_3 per cation	15.27	15.27	15.27	$cm^3\ mol^{-1}$	From density
$\overline{D}$, the mean cation vacancy diffusivity	5×10^{-19}	5×10^{-19}	7×10^{-19}	$cm^2\ s^{-1}$	From fitting
σ_D, the standard deviation of cation vacancy diffusivity	$0.5\overline{D}$	$0.5\overline{D}$	$0.5\overline{D}$		From fitting
α, polarizability of bl/s interface	0.15	0.15	0.16		From Figure 8-5
ε, the electric field strength	3×10^6	3×10^6	3×10^6	$V\ cm^{-1}$	Assumed
ξ, the critical vacancy concentration	5.5×10^{13}	9.6×10^{13}	5.2×10^{14}	cm^{-2}	From Figure 8-6
J_m, the critical vacancy flux	3.4×10^{12}	6.8×10^{12}	3.4×10^{13}	$cm^{-2}\ s^{-1}$	From Figure 8-6
β, pH dependence of $\phi^0_{f/s}$	-0.01	-0.01	-0.01	V	From Figure 8-10
$w = \frac{\chi}{2}\Delta G^o_A + \Delta G^o_S - \frac{\chi}{2}F\phi^0_{f/s}$	-14,707	-18,740	-31,420	$J\ mol^{-1}$	From Figure 8-5

Table 8-2: Comparison between parameters obtained from numerical analysis on passivity breakdown potentials and from optimization of the PDM on metastable pit nucleation rate of carbon steel. Note the discrepancy in the composition of carbon steels and experimental conditions.

Experimental	Data type	σ_D	ξ (cm^{-2})	J_m (cm^{-2} s^{-1})	w (J mol^{-1})
CarElso 70 SOHIC (C 0.15%, S 0.0005%, P 0.005%) pH ≈ 12.4 at 25°C	Potentiodynamically determined passivity breakdown potential	$0.5\overline{D}$	5.50×10^{13}	3.40×10^{12}	-14,707
A516-70 (C 0.31%, S 0.04%, P 0.035) pH = 8.3 at 25°C	Potentiostatically determined metastable pit nucleation rate	$0.75\overline{D}$	3.10×10^{14}	8.34×10^{12}	-24,324

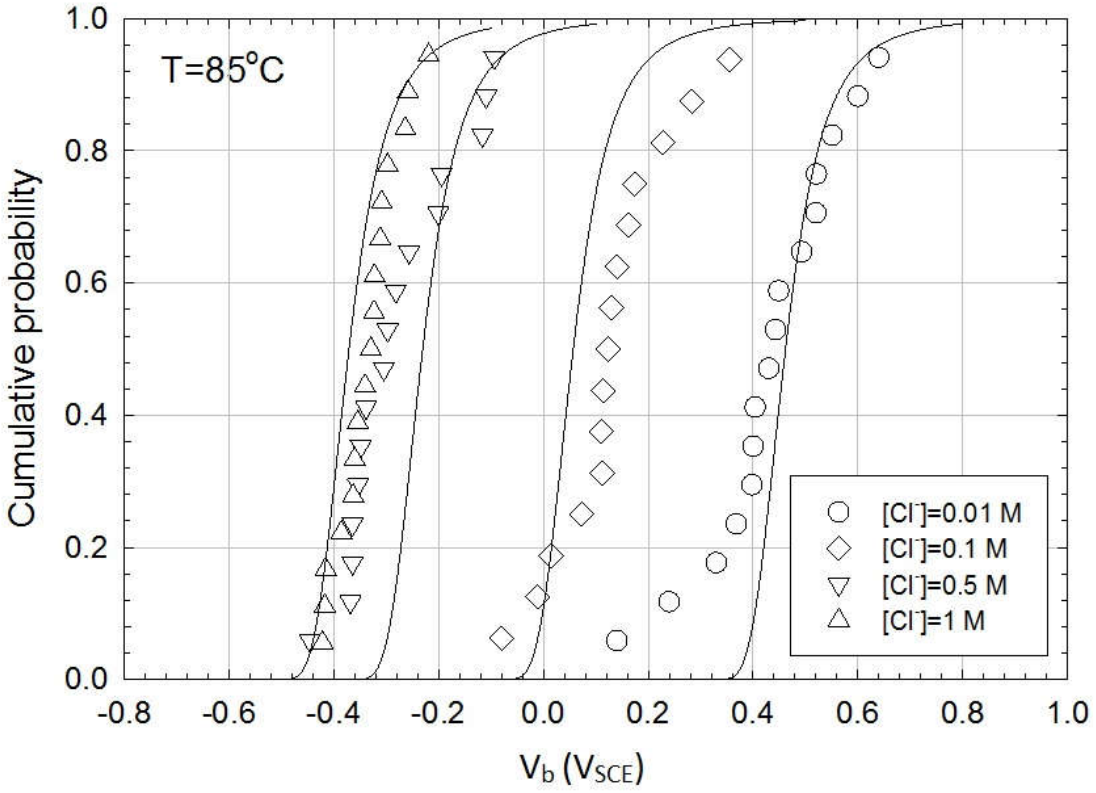

Figure 8-8: Calculated cumulative probabilities in the breakdown potential for carbon steel in deaerated sat. $Ca(OH)_2$ with different chloride concentrations at 85 °C, compared with the

experimentally determined distributions. The solid lines are the calculated distributions with $\sigma_D = 0.5\,\overline{D}$, while the marked points are the experimental data.

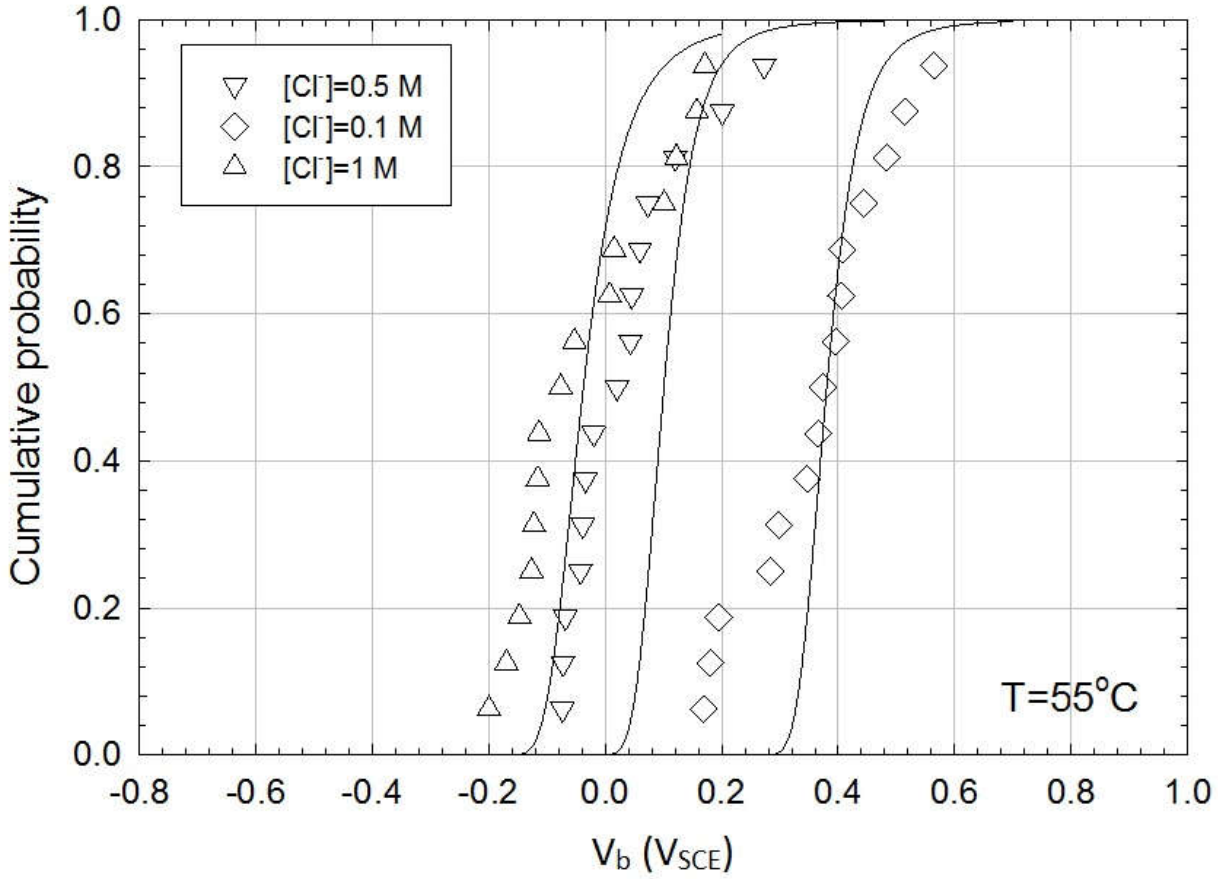

Figure 8-9: Calculated cumulative probabilities in the breakdown potential for carbon steel in deaerated sat. $Ca(OH)_2$ with different chloride concentrations at 55 °C, compared with the experimentally determined distributions. The solid lines are the calculated distributions with $\sigma_D = 0.5\,\overline{D}$, while the marked points are the experimental data.

8.3 Results in Lower-pH Solutions and the Effect of pH

Studies were also conducted by this group in solutions with lower pH values ranging from 8.2 to 11.5 at 25°C. At each pH, the same experiments as done in the sat. $Ca(OH)_2$ were performed (i.e. distribution in V_b determined potentiodynamically at different [Cl^-] and with different scan rates). Figure 8-10 exhibits the mean V_b of carbon steel determined using the scan rate of 0.1667 mV/s as a function of pH in solutions with the chloride concentration of 1 M at 25 °C. A general linear relationship can be identified between $\overline{V_b}$ and pH with a deviation observable at pH of 11.5. This anomaly is probably associated with the dependence of passivity breakdown upon the anion species in solution. Due to the wide pH range that needed to be covered in the study, different buffer solutions had to be prepared. Borate buffer solutions were used for the experiments at pH = 8.2, 9.0 and 10.0, while phosphate buffer solution (0.05 M Na_2HPO_4 + 0.1 M NaOH) was prepared for the experiments at pH = 11.5. It has been reported by several authors [43-45] that, for iron in phosphate solution, a relatively thick phosphorous compound layer tends to form in the outer part of the film (the outer-layer), due to the much lower solubility product for $Fe_3(PO_4)_2$ (10^{-36} or 10^{-25} [46]) than those for $Fe(OH)_2$ (10^{-17} or 10^{-14} [46]) and ferrous borate ($10^{-8} \sim 10^{-6}$ [46]). Such film formed in phosphate solution was found [47] to possess greater donor density than that formed in borate solution, which may create a larger number of structural and electronic defects, facilitating passivity breakdown (more negative V_b). It was also observed [47, 48] that phosphate ions were incorporated deeper into the film than borate ions at a constant film thickness, so the former might be able to alter the film properties more strongly. The $\overline{V_b}$ data at pH of 11.5 was then excluded in the linear fitting as shown in Figure 8-10. According to Eq. (7-2) from the PDM, the slope of the linear relationship of $\overline{V_b}$ vs. pH equals to a simple expression of $-\beta/\alpha$. By inserting the value of α obtained earlier (α = 0.15 at 25 °C), β can be readily calculated as being equal to about -0.014 V for the film on carbon steel, a result very close to what was reported previously for Type 403 stainless steel (β = -0.01 V) [4].

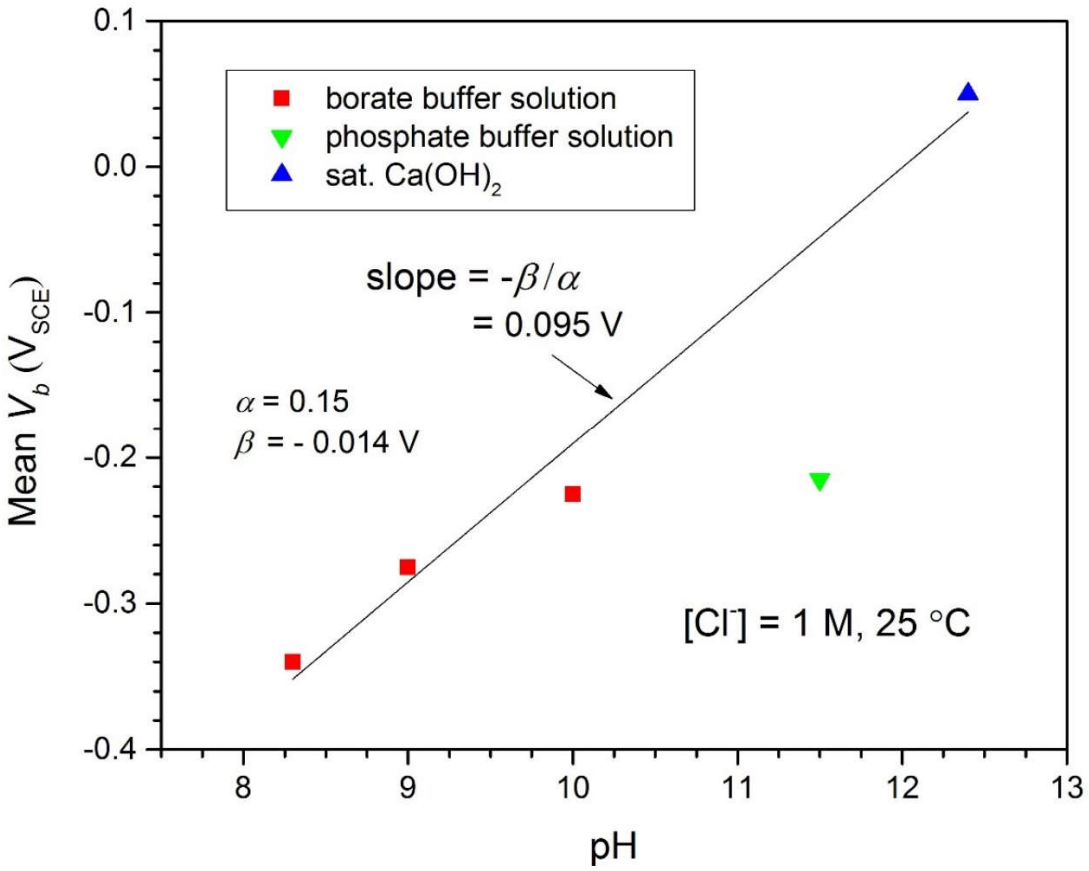

Figure 8-10: Effect of pH on the mean passivity breakdown potential of carbon steel obtained with a scan rate of 0.1667 mV/s in alkaline solutions with [Cl^-] = 1 M at 25 °C. The solid line shows the linear fitting of the mean V_b at pH values excluding 11.5.

8.4 Summary

In this chapter, we have analyzed the effect of temperature, chloride concentration, and potential scan rate on passivity breakdown of carbon steel in deaerated, saturated $Ca(OH)_2$ + NaCl solution. The principal results are concluded as follows:

1. The polarizability of the bl/s interface (α) is found to be around 0.15 ~ 0.16 and to be almost independent of temperature.
2. An increase in temperature from 25 °C to 85 °C resulted in a decrease in localized corrosion resistance as reflected in a negative shift in the critical breakdown potential (V_b).
3. The critical areal cation vacancy concentration (ξ) for passivity breakdown determined from the correlation between breakdown potential (V_b) and potential scan rate ($v^{1/2}$) based upon the PDM is found to be in close agreement with the value calculated from the geometric structure at the metal/barrier layer (α-Fe_2O_3) interface.
4. Statistical analysis of the experimentally determined breakdown potential data has shown that the distribution in breakdown potential (V_b) follows a near-normal distribution as predicted by the PDM.
5. Passivity breakdown potential results measured at multiple pH values ranging from 8.2 to 12.4 have been used to calculate the dependence of the potential drop across bl/s interface on pH (β), which equals to -0.014 V.
6. Correlation between experimentally collected data on the breakdown potential (V_b) as functions of chloride ion activity, temperature, and potential scan rate have demonstrated the validity of the PDM.

References

[1] K. Aligizaki, D.D. Macdonald, Proc. CORROSION 2001, 2001.
[2] A. Saleh, O. Azizi, O. Rosas-Camacho, A. Al-Marzooqi, D. Macdonald, Corrosion Engineering, Science and Technology, 46 (2011) 104-110.
[3] Z. Szklarska-Smialowska, ZS-Smialowska, Pitting and crevice corrosion, NACE International Houston, TX, 2005.
[4] Y. Zhang, D.D. Macdonald, M. Urquidi-Macdonald, G.R. Engelhardt, R.B. Dooley, Corros Sci, 48 (2006) 3812-3823.
[5] V. Gouda, British Corrosion Journal, 5 (1970) 198-203.
[6] J.A. Gonzalez, J. Algaba, C. Andrade, British Corrosion Journal, 15 (1980) 135-139.
[7] J.-Y. Zou, D.-T. Chin, Electrochim Acta, 33 (1988) 477-485.
[8] L. Bertolini, F. Bolzoni, T. Pastore, P. Pedeferri, British Corrosion Journal, 31 (1996) 218-222.
[9] G. Glass, N. Buenfeld, Corros Sci, 39 (1997) 1001-1013.
[10] G. Glass, N. Buenfeld, Progress in Structural Engineering and Materials, 2 (2000) 448-458.

[11] M. Moreno, W. Morris, M. Alvarez, G. Duffó, Corros Sci, 46 (2004) 2681-2699.
[12] K.Y. Ann, H.-W. Song, Corros Sci, 49 (2007) 4113-4133.
[13] M. Valcarce, M. Vázquez, Electrochim Acta, 53 (2008) 5007-5015.
[14] P. Ghods, O. Isgor, G. McRae, T. Miller, Cement and Concrete Composites, 31 (2009) 2-11.
[15] H. Xu, Y. Liu, W. Chen, R.-G. Du, C.-J. Lin, Electrochim Acta, 54 (2009) 4067-4072.
[16] L. Li, A. Sagues, Corrosion, 57 (2001) 19-28.
[17] L. Lin, C. Chao, D. Macdonald, J Electrochem Soc, 128 (1981) 1194-1198.
[18] D.J. Ellerbrock, D.D. Macdonald, J Electrochem Soc, 141 (1994) 2645-2649.
[19] S. Yang, D.D. Macdonald, Electrochim Acta, 52 (2007) 1871-1879.
[20] Y. Zhang, M. Urquidi-Macdonald, G.R. Engelhardt, D.D. Macdonald, Electrochim Acta, 69 (2012) 12-18.
[21] Y.C. Zhang, M. Urquidi-Macdonald, G.R. Engelhardt, D.D. Macdonald, Electrochim Acta, 69 (2012) 1-11.
[22] G. Burstein, P. Pistorius, S. Mattin, Corros Sci, 35 (1993) 57-62.
[23] P. Pistorius, G. Burstein, Corros Sci, 36 (1994) 525-538.
[24] P.C. Pistorius, G.T. Burstein, Philos T Roy Soc A, 341 (1992) 531-559.
[25] Y. Cheng, J. Luo, J Electrochem Soc, 146 (1999) 970-976.
[26] M. Alvarez, J. Galvele, Corros Sci, 24 (1984) 27-48.
[27] J.R. Galvele, J Electrochem Soc, 123 (1976) 464-474.
[28] Y.T. Tan, S.L. Wijesinghe, D.J. Blackwood, Corros Sci, 88 (2014) 152-160.
[29] K.S. Pitzer, J.C. Peiper, R. Busey, Journal of Physical and Chemical Reference Data, 13 (1984) 1-102.
[30] Z. Szklarska-Smialowska, Corrosion, 27 (1971) 223-233.
[31] J. Soltis, N. Laycock, D. Krouse, Corros Sci, 53 (2011) 7-10.
[32] G. Frankel, J Electrochem Soc, 145 (1998) 2186-2198.
[33] H. Leckie, H. Uhlig, J Electrochem Soc, 113 (1966) 1262-1267.
[34] W. Schwenk, Corrosion, 20 (1964) 129t-137t.
[35] J. Bastidas, J. Polo, C. Torres, E. Cano, Corrosion, 57 (2001) 666-669.
[36] T. Szauer, J. Jakobs, Corros Sci, 16 (1976) 945-949.
[37] T. Haruna, D.D. Macdonald, J Electrochem Soc, 144 (1997) 1574-1581.
[38] L. Pauling, S.B. Hendricks, J Am Chem Soc, 47 (1925) 781-790.
[39] D. Wilburn, W. Bassett, American Mineralogist, 63 (1978) 591-596.
[40] D.D. Macdonald, M. Urquidi-Macdonald, Electrochim Acta, 31 (1986) 1079-1086.
[41] D.D. Macdonald, Pure and Applied Chemistry, 71 (1999) 951-978.
[42] D. Macdonald, G. Engelhardt, 2.39 Predictive Modeling of Corrosion, in: Shreir's Corros, Elsevier BV, 2010.
[43] I. Sieber, H. Hildebrand, S. Virtanen, P. Schmuki, Corros Sci, 48 (2006) 3472-3488.
[44] Z. Szklarska‐Smialowska, R. Staehle, J Electrochem Soc, 121 (1974) 1393-1401.
[45] W. Kozlowski, J. Flis, Corros Sci, 32 (1991) 861-875.
[46] J. Thomas, British Corrosion Journal, 1 (1966) 156-160.
[47] K. Azumi, T. Ohtsuka, N. Sato, J Electrochem Soc, 134 (1987) 1352-1357.
[48] R. Nishimura, N. Sato, ISIJ international, 31 (1991) 177-183.

Chapter 9 Conclusions and Suggested Future Work

9.1 Conclusions

This dissertation work is carried out to explore the passivity and passivity breakdown of carbon steel, the material of the main metallic barrier in the HLNW Supercontainer in Belgium, in the simulated concrete pore solution under anoxic conditions characterized by relatively low corrosion potential. In light of the importance of devising deterministic models in the prediction of accumulated corrosion damage of carbon steel over an exceedingly long period, the kinetics of the passivity and metastable pit nucleation were also studied within the framework of the analytic Point Defect Model. The principal findings of this work are summarized as follows:

1. The commonly observed irreversibility of the passive state on carbon steel in alkaline solutions was examined and the fundamental source of this irreversibility was investigated. Potentiostatic polarization, EIS, and Mott-Schottky analysis were performed at each potential when the potential was stepped in the anodic direction then in the cathodic direction. The EIS results show that the passive system during the cathodic potential stepping has a notably larger imaginary component of impedance than during the anodic potential stepping, signifying that the film existing during the cathodic potential stepping possesses higher extent of capacitor character and hence imposes greater hindrance to charge transfer. The n-type character of the passive film on carbon steel has been verified by the positive slopes of the C^{-2} vs. V curves obtained from the M-S analysis, and by semi-quantitatively estimating the donor density inside the film from the magnitude of the slopes, a discrepancy in the defect structure of the passive film for the opposite potential stepping was discovered: the donor density decreases markedly as the potential is stepped in the anodic direction but remains almost constant after the potential shift is reversed.

2. A passive oxide/hydroxide film has been demonstrated to exist on carbon steel even when the applied potential is below the open circuit potential under highly reducing conditions. A mixed potential model (MPM) created by combining the PDM to describe the dissolution of metals and the Butler-Volmer Equation to account for the cathodic partial process has been successfully used to deconvolve the measured steady-state current into its partial anodic and partial cathodic components. Deconvolution was necessary, because under the redox conditions that exist in the supercontainer of the Belgian plan for the disposal of HLNW during the anoxic phase, the observed current is negative due to the preponderance of the cathodic process, which precludes the direct calculation of the corrosion rate using Faraday's law. Optimization of the MPM on EIS data yields kinetic parameters of the point defects reactions proposed by the PDM and hence allows calculation of the passive current density from which the corrosion rate is determined. A variety of results has been presented in this paper to demonstrate the validity of this model.

3. The steady-state anodic current density, the steady-state film thickness and the diffusivity of the donors were extracted from the optimization of the MPM on experimental EIS data. The steady-state anodic current density is found independent of voltage, and the mean current density for the cathodic potential stepping, 29.2 nA/cm^2, is more than halved than that for the anodic potential stepping, 68.8 nA/cm^2, a manifestation of the pronounced

effect that the potential excursion direction has on the passive state of carbon steel. The corrosion rate for the cathodic potential stepping, which resembles the decreasing corrosion potential of carbon steel inside the Supercontainer, was obtained to be 0.228 μm/year, resulting in a 22.8 mm thickness loss for the over pack after 100,000 years with only 7.2 mm wall-thickness left. It needs to be recognized that this estimation is based on the presumption that the Supercontainer corrosion system will not change within the 100,000-year service horizon, which might not be true and calls for the knowledge of the corrosion evolution path to produce a more accurate prediction. A slower rate of film thinning (1.2 nm/V) upon cathodic potential stepping than film growing (1.6 nm/V) upon anodic potential stepping is observed in the steady-state film thickness results. Both the film thickness (extrapolated to more anodic potentials) and the linear coefficients $\partial L/\partial V$ obtained in the present study match well with those reported in other work that employed various characterization techniques.

4. By comparing the rate constants, k_3 and k_7, which ultimately control the boundary motion of the passive film, for the opposite potential stepping directions, it is revealed that the fundamental origin of the passivity irreversibility exhibited by carbon steel is the kinetically slower film growth and slower film dissolution processes when the potential is shifted in the negative direction than when it is displaced in the positive direction. The dominant donor species within the passive film has been determined as iron interstitial based on the much greater rate constant of iron interstitials generation than that of oxygen vacancies generation.

5. The kinetic theory for nucleation of metastable pits in terms of the PDM has been applied the first time to the analysis of metastable pit nucleation data. Equations describing the evolution of the nucleation rate of metastable pits and the total number of metastable pitting incidents have been tested by conducting optimization of the kinetic model on experimental data reported in the literature that were acquired on a variety of metallic materials, including stainless steel, carbon steel, pure iron, pure aluminum, and Alloy-22. Satisfactory agreement was obtained between the optimized and experimental data for all of the selected materials. Useful fundamental parameters that characterize the nucleation process of metastable pits with reasonable values were extracted from the optimization for each of those materials. The successful accounting of the independent data from multiple sources for various metallic materials strongly demonstrates that the PDM can be applied as a powerful and versatile underlying theory for studying and understanding metastable pitting on metal surfaces.

6. The effect of temperature, chloride concentration, and potential scan rate on passivity breakdown of carbon steel in deaerated, saturated $Ca(OH)_2$ and other alkaline buffer systems were investigated. The polarizability of the bl/s interface (α) is found to be around $0.15 \sim 0.16$ and to be almost independent of temperature. An increase in temperature from 25 °C to 85 °C resulted in a decrease in localized corrosion resistance as reflected in a negative shift in the critical breakdown potential. The critical areal cation vacancy concentration for passivity breakdown determined from the correlation between breakdown potential and potential scan rate is found to be in close agreement with the value calculated from the geometric structure at the metal/barrier layer (α-Fe_2O_3) interface. Statistical analysis of the experimentally determined breakdown potential data has shown that the distribution in breakdown potential follows a near-normal distribution as predicted

by the PDM. Passivity breakdown potential results measured at multiple pH values ranging from 8.2 to 12.4 have been used to calculate the dependence of the potential drop across bl/s interface on pH, β, which equals to -0.014 V.

9.2 Suggested Future Work

A direct measurement of the corrosion rate is necessary to corroborate the optimization results of the partial anodic current density. Highly mass-sensitive techniques are required due to the very low corrosion rate of carbon steel in the alkaline SCPS. Two techniques have been proposed for this purpose: electrochemical quartz crystal microbalance (EQCM) which measures the mass change of the sample (a thin disposition film on quartz crystal) by monitoring the change in the resonance frequency of the quartz crystal; and resistometry which measures the mass loss of the sample (a thin wire) from the change in the resistance of the sample wire. The apparatus of these two techniques are currently being setup and will be finished in the near future. Provided more solid experimental corrosion rate data, the optimization of the MPM is also expected to yield more accurate prediction of the corrosion rate.